University of Southampton

Faculty of Engineering and Physical Sciences

Optoelectronics Research Centre

Atomic Scale Dynamics of Thermal and Driven Motion in Photonic Nanostructures

by

Tongjun Liu

ORCID ID 0000-0003-4931-1734

Thesis for the degree of Doctor of Philosophy

January 2023

University of Southampton

Abstract

Faculty of Engineering and Physical Sciences

Optoelectronics Research Centre

Doctor of Philosophy

Atomic Scale Dynamics of Thermal and Driven Motion

in Photonic Nanostructures

by

Tongjun Liu

This Thesis reports on the study of atomic scale dynamics of thermal and driven motion in nanomechanical and nano-optomechanical photonic metamaterials system including their atomic scale movement visualization and control.

- I have developed a sub-atomic motion visualization technique combining picometric displacement sensitivity with the nanometric spatial resolution of a conventional scanning electron microscope, and demonstrated its application in characterization of thermomechanical (Brownian) motion in nanomechanical structures, nanomechanical photonic metamaterials, NEMS/MEMS devices and biological structures.
- Using this technique, I have reported on the first observation of short-timescale ballistic motion in the flexural mode of a nano-membrane cantilever, driven by thermal fluctuations of flexural phonons. Within intervals <10 μs, the membrane moves ballistically at a constant velocity of ~300 μm/s, on average. Access to ballistic regime provides the first experimental verification of the equipartition theorem and Maxwell-Boltzmann statistics for flexural modes.
- For the first time I have optically resolved the average position of a nanowire with an absolute error of ~30 pm using light at a wavelength of λ= 488 nm, thus providing the first example of sub-Brownian metrology with λ/10,000 resolution. To localize the nanowire, I employed a deep learning analysis of the scattering of topologically structured light, which is highly sensitive to the nanowire's position.
- For the first-time, I have demonstrated: a) optical parametric control of the spectrum of thermomechanical motion on an array of nano-opto-mechanical resonators; b) phononic frequency comb generation by the array; c) thermal energy exchange between two coupled oscillators within an optically driven array.

Collectively, these works advance the visualization and control of photonic nanostructures at the picometre scale, thus opening up the exciting field of picophotonics.

Table of Contents

Table of Tables

Table of Figures

Table of Figures

List of Accompanying Materials

The research data presented in this Thesis can be found as:

T. Liu (2023), Dataset for Atomic Scale Dynamics of Thermal and Driven Motion in Photonic Nanostructures. DOI: 10.5258/SOTON/D2288

Research Thesis: Declaration of Authorship

Print name: TONGJUN LIU

Title of thesis: Atomic Scale Dynamics of Thermal and Driven Motion in Photonic Nanostructures

I declare that this thesis and the work presented in it are my own and has been generated by me as the result of my own original research.

I confirm that:

1. This work was done wholly or mainly while in candidature for a research degree at this University;
2. Where any part of this thesis has previously been submitted for a degree or any other qualification at this University or any other institution, this has been clearly stated;
3. Where I have consulted the published work of others, this is always clearly attributed;
4. Where I have quoted from the work of others, the source is always given. With the exception of such quotations, this thesis is entirely my own work;
5. I have acknowledged all main sources of help;
6. Where the thesis is based on work done by myself jointly with others, I have made clear exactly what was done by others and what I have contributed myself;
7. Parts of this work have been published as journal papers and conference contributions listed in Appendix B.

Signature: .....Date:.....

Acknowledgements

I'm grateful to have the chance to work in the Nanophotonics and Metamaterials group led by Prof. Nikolay Zheludev at the Optoelectronics Research Centre in the University of Southampton. I acknowledge all the continuous guidance and support from my supervisors Dr. Jun-Yu (Bruce) Ou, Prof. Kevin MacDonald and Prof. Nikolay Zheludev. Words can't describe how thankful I am to Dr. Jun-Yu (Bruce) Ou, my teacher and friend, who offered me the project of e-beam motion probing and taught me to do experiments at the beginning of my PhD course, that is really important for an experimentalist beginner. Bruce is always the first person I can turn to and who is willing and able to offer me help whenever I have experimental difficulties. I'm thankful to Prof. Kevin MacDonald for helping me with improving my conference's presentation and my manuscript, leaving me a lot of freedom on pursuing my PhD research, and guiding me to think independently and critically, which is really important for a researcher. I'm grateful to Prof. Nikolay Zheludev in particular for his sufficient mentoring, timely discussion, challenges, extraordinary wealth of knowledge about physics and unique vision, which I will undoubtedly benefit from throughout my academic career.

I express my gratitude to my collaborators and friends Drs. Jinxiang Li and Dimitrios Papas belonging to the nanomechanics community in the NanoMeta group for their fruitful discussion on experiments, results analysis and sharing skills/experiences. I would also like to thank my collaborators Drs. Eric Plum, Nikitas Papasimakis, Jie Xu, Eng Aik Chan and Prof. Vitalyi E. Gusev for their important contribution to my PhD projects. I need to thank Sergei Kurdiumov for his training on using computation server and discussion on machine learning. I'm grateful to Oleksandr Buchnev for focused ion beam milling machine training and to Neil Session for training on clean room facilities.

I would like to thank all the people of the Nanophotonics and Metamaterials group for their help during my studies and the great time we had during these four years. In particular Drs. Hao Li, Qiang (Eric) Zhang, Xinguang Liu, Tanchao Pu and Apostolos Zdagkas for the great time we had together during their stay in our group. I also thank Drs. Guanghui Yuan and Yijie Shen for sharing their MATLAB codes on structured light generation and their knowledge of structured light.

I would like to thank the China Scholarship Council (CSC) for providing me living stipends and offering me an opportunity to study abroad. I can't thank you enough my parents for your raising me up and support to purse my PhD dream. I'm grateful to my two elder sisters who help look after my parents when I'm away from home. Last but not least, I owed a lot to my wife Min Dai for her continuous support and encouragement whenever I feel depressed, her tolerance and daily online

accompanying and her encouragement on pursuing my own research interest, thinking and doing independently.

Abbreviations and Acronyms

AFM ..... Atomic Force Microscopy

AI..... Artificial Intelligence

ASD ..... Amplitude Spectral Density

BIC..... Bound states In the Continuum

BSE ..... Back-Scattered Electrons

CL ..... Cathodoluminescence

CNN..... Convolutional Neural Network

DMD..... Digital Micromirror Device

EDX ..... Energy-Dispersive X-ray spectroscopy

EIT ..... Electromagnetic Induced Transparency

EOM ..... Electro-Optical Modulator

ETD..... Everhart–Thornley Detector

FDT..... Fluctuation-Dissipation Theorem

FDTD ..... Finite Difference Time Domain method

FEM..... Finite Element Method

FFT ..... Fast Fourier Transform

FIB..... Focused Ion Beam

FoV..... Field of View

FWHM..... Full Width at Half Maximum

HMV..... Hyperspectral Motion Visualization

IoT..... Internet of Things

LDV..... Laser Doppler Vibrometer

MD ..... Molecular Dynamics

MEMS/NEMS ..... Micro/Nano-Electro-Mechanical-System

MLP..... Multi-Layer Perceptron

MSD ..... Mean Square Displacement

NA ..... Numerical Aperture

NED ..... Noise Equivalent Displacement

NVACF..... Normalized Velocity Autocorrelation Function

PALM..... Photo-activated Localization Microscopy

PECVD ..... Plasma-Enhanced Chemical Vapor Deposition

PML ..... Perfectly Matching Layer

PMT ..... Photomultiplier tube

PSD ..... Power Spectral Density

PSO ..... Particle Swarm Optimization

PSWF ..... Prolate Spheroidal Wavefunctions

RMS ..... Root Mean Square

SE ..... Secondary Electron

SEI ..... Secondary Electron Imaging

SEM ..... Scanning Electron Microscope

SLM ..... Spatial Light Modulator

SNR ..... Signal-to-Noise Ratio

SO ..... Super-Oscillatory

SOL ..... Super-Oscillatory Lens

SPM ..... Scanning Probe Microscopy

SQL ..... Standard Quantum Limit

STED ..... Stimulated Emission Depletion Microscopy

STM ..... Scanning Tunnelling Microscopy

STORM ..... Stochastic Optical Reconstruction Microscopy

TLD ..... Through-the-Lens Detector

UEM ..... Ultrafast Electron Microscopy

UHR ..... Ultra-High-Resolution

VACF ..... Velocity Autocorrelation Function

Chapter 1 Introduction

Angström scale movement and femto- to pico-second dynamics are readily found in atomic and molecular systems such as free charge carrier moving in crystals, chemical bond vibration or molecular vibration, rotation, chemical reaction process [1, 2], phonon transport in crystals [3] and 2D materials [4]; atomic length scale protein conformational changes, and motion that happens in protein folding process [5].

In nano-(opto)mechanics [6], electromagnetic, optical, thermal and quantum fluctuation forces become stronger as the physical dimensions of objects decrease (e.g. the Coulomb force vs. separation between two electrons) and at sub-micron scales they begin to compete with weakening forces of elasticity (e.g. Hooke's law force vs. extension/compression of a spring). Nanoscale movements also become faster as mass decreases with size, achieving gigahertz bandwidth at the nanoscale [6]. This means movement can be activated by different kinds of forces at relatively high frequency. Exciting new functionalities emerge through the exploitation of nanomechanical movements of nanoparticles, -powders, -wires, -ribbons, -tubes, -shells, -composites and -membranes (including 2D materials such as graphene).

Indeed, forces at the nanoscale can act as a bridge between the domains of nanomechanics and nanophotonics. The changing balance of elastic and electromagnetic forces or quantum fluctuation forces on the nanoscale opens up new possibilities for controlling photonic response through movement of a photonic nanostructure. This is true not only in nanophotonics but also generally in all kinds of systems, such as micro- and nano-electro-mechanical systems (MEMS & NEMS) [7], two-dimensional (2D) materials systems [8], quantum mechanical systems [9] and biomechanical systems [10].

All of these structures exhibit thermal (Brownian) movement with picometre amplitudes at frequencies in the few megahertz to few gigahertz range at room temperature. Nanomechanical effects related to thermal motion and the importance of configuration entropy (all possible configurations or particle positions of a system) at the nanoscale give rise to self-organization and cooperative dynamics in nanosystems [11]. Quantum vacuum fluctuation such as the Casimir effect and Van der Waals interactions play important and often decisive roles in nanomechanical structures [12].

Nano/picoscale movement can also be induced by external stimuli [13], for example in the form of piezoelectric drive, electromagnetic and optical excitation, temperature change, or indeed quantum-level interactions. Important examples include widely-adopted micro- and nano-electro-

mechanical systems (MEMS & NEMS) such as the accelerometers found in every smartphone, nanomechanical photonic metamaterials with variable optical properties controlled by nanoscale movements of photonic nanostructures, and nanofluidic devices for lab-on-chip application in medicine.

Over the last decade, protein nanomechanics and structural dynamics have seen tremendous progress and evolved into a burgeoning field of biochemical research [10].

These considerations present substantial technological opportunities and explain the growing interest in nanomechanics and the fundamentals of atomic scale dynamics.

1.1 Atomic scale dynamics: fundamental science and technological importance

1.1.1 Dynamics at (sub-) atomic scale: fundamental science

The Royal Swedish Academy of Sciences has awarded the 1999 Nobel Prize in Chemistry to Professor Ahmed H. Zewail for showing that it is possible with a rapid laser technique to see how atoms in a molecule move during a chemical reaction. Angström-scale movement and dynamics were assumed to happen during the chemical reaction process. Despite the rich history of chemistry over two millennia, the actual atomic motions involved in chemical reactions had only been observed in real time recently [1]. Chemical bonds break, form, or geometrically change with astonishing rapidity. Whether in isolation or in any other phase, this ultrafast transformation is a dynamic process involving the mechanical motion of electrons and atomic nuclei. The speed of abovementioned atomic motion is ∼1 km/s, and hence, to record atomic-scale dynamics over a distance of an angström, the average time required is ∼100 fs. The very act of such atomic motions as reactions unfold and pass through their transition states is the focus of the field of femtochemistry [1]. With femtosecond time resolution one can “freeze” structures far from equilibrium and prior to their vibrational and rotational motions, or reactivity [1]. Ultrafast pulsed laser techniques have made the direct exploration of this temporal realm a reality. Spectroscopy, mass spectrometry, and diffraction play the role of “ultrahigh-speed photography” in the investigation of molecular processes. A femtosecond laser probe pulse provides the shutter speed for freezing nuclear motion with the necessary spatial resolution. The pulse probes the motion by stroboscopy, i.e., by pulsed illumination of the molecule in motion and recording the particular snapshot. A full sequence of the motion is achieved by using an accurately timed series of these probe pulses, defining the number of frames per second. These achievements mark the beginning of sub-atomic dynamics research in physics, chemistry and biology.

Therefore, sub-atomic scale dynamics in terms of either characteristic length or time scale is of great fundamental interest as well as in the research community advancing fundamental understanding of electron transport, ultrafast dynamics and light-matter interactions in materials.

There are some examples in the following:

Ultrafast dynamics of electrons: Electrons have played a central role in the scientific and technological revolution of the 20th century. It is widely anticipated that their role as a key driver of scientific and technological progress will be increasingly replaced by photons in the 21st century. However, this assessment may be premature, or overly simplistic. About half a century after the invention of transistors and lasers, our insight into and impact on the atomic-scale motion of electrons in matter is still in its infancy. Therefore, the scientific and technological progress brought about by electrons is not over yet. Rather, this is just the beginning, considering that experimental tools and techniques to observe and control electron dynamics in real time at the atomic scale are now available [2, 14-17].

Phonon transport in 2D materials: Thermal transport in two-dimensional (2D) materials has attracted great attention since the discovery of high thermal conductivity in graphene, which is closely related to ballistic, hydrodynamic and flexural phonon transport [18]. It was recently reported that the lattice thermal conductivity of graphene is dominated by contributions from the out-of-plane or flexural phonon modes, previously thought to be negligible [19]. This unexpected result was connected to the anomalously large density of states of flexural phonons compared to their in-plane counterparts and to a symmetry-based selection rule that significantly restricts anharmonic phonon-phonon scattering of the flexural modes [19].

Structural dynamics of a single molecule: The internal vibrations of molecules drive the structural transformations that underpin chemistry and cellular function. While vibrational frequencies are measured by Raman spectroscopy, the normal modes of motion (a pattern of motion in which all parts of the system move sinusoidally with the same frequency and with a fixed phase relation) are inferred through theory because their visualization would require microscopy with angström-scale spatial resolution which can be achieved in a scanning tunnelling microscope [20]. Also, scanning probe techniques can leverage atomically precise forces to sculpt matter at surfaces, atom by atom. These forces have been applied quasi-statically to create surface structures and influence chemical processes, and exploiting local dynamics to realize coherent control on the atomic scale [21].

Picophotonics: Picophotonics is the emerging science of light matter interaction at picometre [(sub-) atomic] scale [22]. It includes cavity-electrodynamics at atomic level, atomic scale resolution of metrology and imaging, Langevin dynamics in photonic nanostructures at picometric scale. It also

includes the study of Casimir or Van der Waals forces and non-Hamiltonian forces in nanomechanics [23-25]; electron and plasmon quantum transport through atomic scale gaps [26]; configuration chemistry of individual molecules; protein folding [27]; other dynamic events in macromolecules and nanomachines; entropic forces in nanosystems; and thermal or Brownian nano-(opto-)mechanics at atomic length scale.

1.1.2 Atomic scale movement: technological importance

Richard Feynman first imagined many physically achievable devices or systems in his famous 1959 lecture "There's Plenty of Room at the Bottom"[28], where he invited scientists to enter a new field of physics later known as nanotechnology [7] and tried thinking about and answering the following questions: How to write information at the atomic scale? How to read this information at the atomic level? And inspired by biological systems such as tiny cells, he has also imagined that we can manufacture a nano-machine which can do what we want it to do. How to realize a miniaturized computer also has the marvelous capability of face identification? How to arrange atoms in the way we want? What would the properties of materials be if we could really arrange the atoms the way we want them to?

Molecular machines, micro- and nano-electromechanical system (MEMS/NEMS) and later micro-/nano-mechanical photonic metamaterials have since become practical implementations of this idea [6, 29]. MEMS are microscopic devices with moving parts typically between 1 and 100 micrometers in size. They have established applications in digital spatial light modulators (e.g., Texas Instruments' DMD chips for data projection), and high-performance pressure sensors, gyroscopes, and accelerometers (e.g., in mobile phones). NEMS, as the name suggests, are smaller – being broadly defined as having at least one characteristic dimension in the 1-100 nm range, with a plethora of potential applications in advanced (including quantum level) sensing and signal processing under development [7, 30]. Recent progress in micromechanical sensors and nanomechanical sensors in the internet of things (IoT) demands new techniques for the characterisation of fast nanoscale mechanical movements that underpin the functionalities of microelectromechanical systems (MEMS) and nanoelectromechanical systems (NEMS) devices and sensors (found in any smartphone and IoT devices), reconfigurable micromechanical switches for telecommunication networks and Lidar for autonomous vehicles.

As another implementation of Feynman's idea, mechanically reconfigurable photonic metamaterial devices, namely, metadevices [6, 29] take advantage of the changing balance of forces at the nanoscale as detailed in section 1.1.3. They engage electromagnetic (Coulomb, Lorentz, Ampère, and optical gradient) forces, as well as thermal effects (differential expansion, shape memory) and

acoustic excitation to dynamically change their optical properties [6]. Atomic- to nano-scale changes in the geometry and/or spatial arrangement of constituent 'metamolecule' building blocks fabricated on elastic nano-membranes can deliver a wealth of optical modulation and tuning functionalities with electro-/magneto-/thermo-/acousto-optical and nonlinear response coefficients orders of magnitude larger than those found in natural media [6].

1.1.3 Atomic scale dynamics of thermal motion in photonic nanostructures

Photonic metamaterials or metasurfaces consist of arrays of subwavelength unit cells also known as 'metamolecules' that are made of optical antennas realized recently by the progress in manufacturing technology and nanofabrication. They are artificially engineered materials that have boosted the development of miniaturized optical and photonic devices because of their unprecedented and controllable effective electromagnetic properties, including electric permittivity and magnetic permeability [31], and full wavefront shaping: amplitude, phase, polarization, wavevector and total angular momentum (spin plus orbital angular momentum) control [32]. Importantly, the effective properties of metamaterials are mainly dependent on the geometry and arrangement of the constituting subwavelength unit cells. This enables versatile designs of their electromagnetic properties.

An important research direction in nanophotonics and metamaterials is mechanically reconfigurable metamaterials or metasurfaces that goes towards the development of reconfigurable metamaterial devices [6, 29], via integrating nanomechanical actuation mechanism with metamolecules, see Figure 1.1. This is achieved by structurally rearranging the metamolecule array, i.e. repositioning the metamolecules of the arrays, or their components, with respect to each other by engaging electromagnetic Coulomb, Lorentz and Ampère forces [6, 29], as well as thermal stimulation and optical signals to dynamically change their optical properties at the megahertz to gigahertz frequency range.

By encoding the mechanical degree of freedom to the optical counterpart, nanomechanical photonic devices formed as periodic arrays of optical antennas supported by flexible nanomembrane structures have boosted the development of reconfigurable optical metamaterials or metasurfaces. This allows one to achieve giant thermal-optical [33], electro-optical [34, 35], electro-chiral [36], magnetoelectro-optical [37], acousto-optical [38], phase change [39, 40], thermoelastic [41], nonlinear optical responses [42] and realize an electrostatically addressable electro-optical modulator [43], dynamic wave plate [40] and plasmonic colours for sustainable optical displays [44].

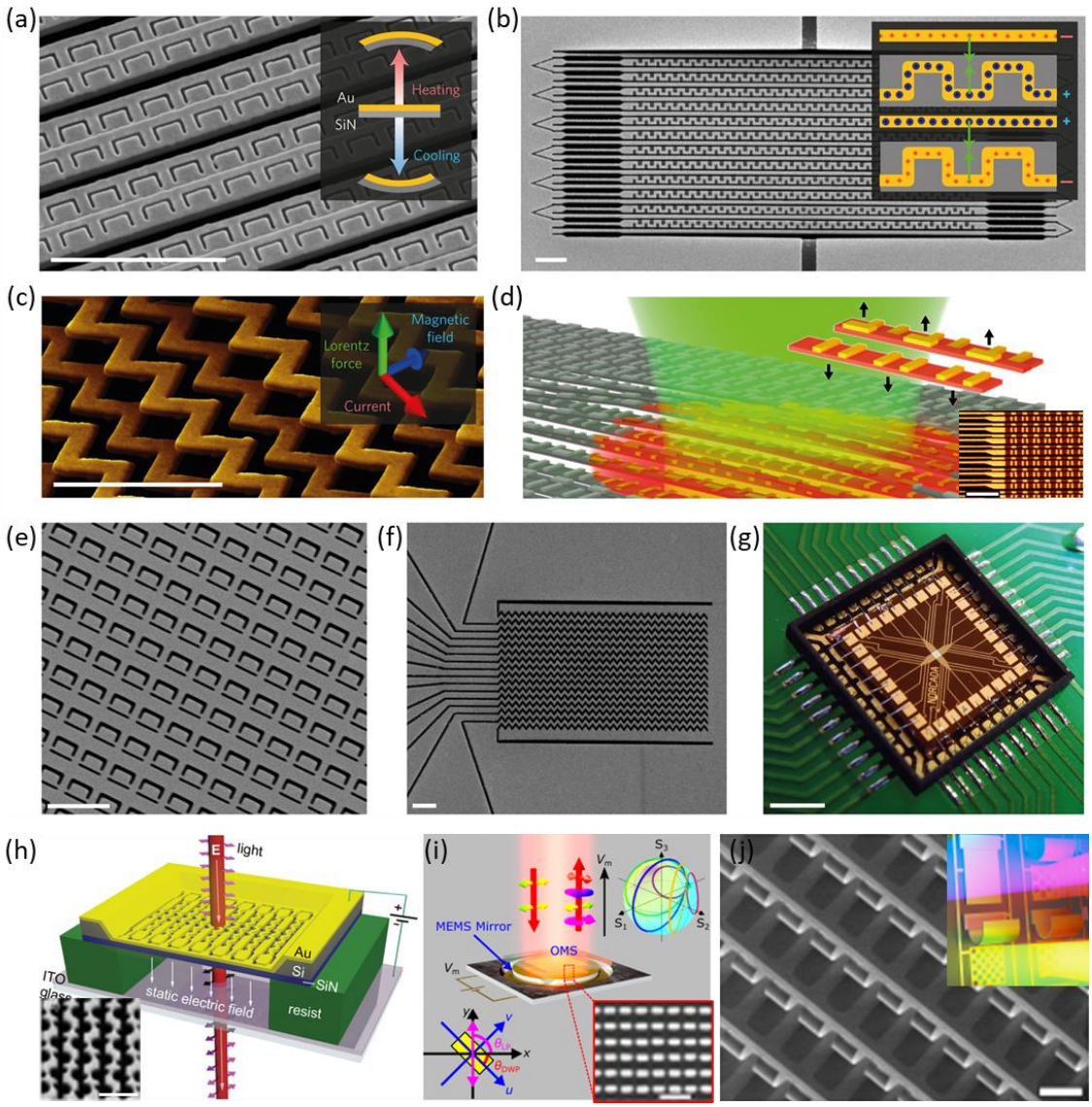

Figure 1.1 **Reconfigurable nanomechanical photonic metamaterials.** (a) Thermally reconfigurable metamaterial driven by differential thermal expansion between gold and silicon nitride layers [33]. (b) A meta electro-optical modulator driven by electrostatic forces [45]. (c) A magnetically actuated optical nanomembrane metamaterial [46]. (d) An all-optical reconfigurable nano-optomechanical metamaterial [35]. (e) A sub-GHz nonlinear device: all-dielectric metamaterial with a large optomechanical nonlinearity [34]. (f,g) A spatial light modulator: electrically addressable metadevice randomly reconfigurable in one dimension [43]. (h) Electrogyratory metamaterial suspended above an ITO-coated glass back-plane. Static electric field actuates the nanomechanical material, changing its chirality and optical activity [36]. (i) MEMS dynamic wave plate [40]. (j) MEMS cantilever–controlled plasmonic colours for sustainable optical displays [44]. Scale bars in a-f, h, are 2 μm; g, 2 mm; e, 500 nm; j, 50 μm.

In nano-(opto-)mechanical systems or more precisely their components, such as a cantilever or a bridge beam of microscopic length and nanoscopic cross section, experience thermal motion which induces fluctuation of optical properties. While optical resonances can be characterized in routine transmission and reflection experiments, mapping the high-frequency mechanical resonances of individual elements in complex metamaterial structures such as illustrated in Figure 1.1b-e is challenging. In particular, the thermal vibration frequencies of nanomechanical devices increase as objects decrease in size reaching MHz to GHz. Optical antennas or resonators are supported by the moving nanomechanical components such as bridge beams; typically, they have width and

thickness of a hundred nanometres smaller than the diffraction limit and length of 10s micrometres. These thermal movements have an averaged motion amplitude of 100 pm which is at atomic length scale (e.g. the van der Waals diameter of a silicon atom is ~220 pm).

Thermomechanical movement is of significance in technological applications and fundamental research. Firstly, thermal vibrations in nanomechanical photonic metamaterials result in small fluctuations of their optical properties but may perturb their switching characteristics. This is because as the dimensions of a mechanical oscillator shrink to the molecular scale, their vibrations become increasingly coupled and strongly interacting until even weak thermal fluctuations could make the mechanical oscillator nonlinear [47]. Secondly, these fluctuations provide an opportunity for the characterization of mechanical properties and/or properties of the environment, and can provide a reference for calibration of displacement sensitivity, which is important in metrology. Furthermore, if we are interested in the high-speed operation of these devices at timescales below its momentum relaxation time typically at nanosecond level, the Brownian motion of micro/nano-objects becomes 'ballistic' [48]. Finally, nano-(opto-)mechanical devices are underpinned by their mechanical degree of freedom. Therefore, it's also of great significance to control the mechanical degree of freedom at will.

1.2 Nanomechanical motion detection techniques

How to quantify/visualize thermomechanical movement of the individual elements in a complex nanomechanical system such as nanomechanical photonic metamaterials? Over the last several decades, many efforts have been put into micro/nanomechanical motion or molecular vibration detection and imaging. These methods include ultrafast (4D) electron microscopy [14], laser interferometry or spectroscopy and Laser Doppler vibrometry [49, 50], scanning probe methods [51-53] (such as using atomic force microscopes, scanning tunnelling microscopes and magnetic force microscopes, etc.).

Time-resolved electron microscopy: Ultrafast electron microscopy (UEM), also called 4D electron microscopy [14], is based on the pump-probe experiments to study complex transient events on the nanoscale temporal and spatial resolution with ultrafast electrons as probes, which has been an area of significant interest in materials science, biology, and chemistry. Figure 1.2a shows direct imaging nanomechanical motions of a nano-cantilever in real space and time with 4D electron microscopy [54]. The frames show referenced difference images with the reference frame (-10 ns) subtracted from subsequent frames. The difference images illustrate the characteristic dynamics of the non-anchored end of the nanoscale Cu crystal cantilever.

However, UEM is a highly-specialized instrument which generally contains very complex optics and timing control systems and also is not easily accessible and is generally used for the study of reversible dynamics. While the conventional scanning electron microscope (SEM) also has the nanometric resolution and is easily accessible, its capability to study the irreversible dynamics such as thermal movement in nanostructures can be further developed as will be shown in Chapter 3.

Laser interferometry: A review on laser light enabled nanomechanical motion measurement and imaging can be found in ref. [50]. Several techniques based on laser-driven interferometers and cavities are illustrated in Figure 1.2b with sensitivities reaching from thermal displacement amplitudes (typically at the picometre scale) all the way to the quantum regime. Figure 1.2b1 shows a simple two-path interferometer for characterizing a mechanical device (top). The thermal motion (blue trace) of a high-Q membrane is readily resolved above the measurement imprecision background (grey). Figure 1.2b2 illustrates a cavity-enhanced measurement in which an optical whispering-gallery-mode resonator is used. Thermal motion (red) trace is far above the imprecision background (grey), which is itself below the resonant standard quantum limit (SQL) for this mechanical mode. Figure 1.2b3 depicts a cavity-based measurement of highly coherent mechanical resonators put inside a Fabry–Pérot resonator. Quantum backaction starts to dominate over the thermal motion of the device, including correlations that lead to squeezing of the output light (violet trace) below the vacuum noise (grey), among others. Figure 1.2b4 compares the relative levels of the measurement imprecision, backaction, and thermomechanical noise in the measurement of the above three cases. Laser-based motion imaging can be realised by scanning laser interferometry over the sample. Scanning laser interferometry is particularly useful to characterize complex mechanical mode structures, such as Si_3N_4 membranes with phononic crystal structures [55].

Laser Doppler vibrometry: A laser Doppler vibrometer (LDV) is a scientific instrument that is used to make non-contact vibration measurements of a surface [49]. The laser beam from the LDV is directed at the surface of interest, and the vibration amplitude and frequency are extracted from the Doppler shift of the reflected laser beam frequency due to the motion of the surface. Using optical heterodyne detection scheme, the output of an LDV is generally a continuous analog voltage that is directly proportional to the target velocity component along the direction of the laser beam.

Laser interferometry and laser Doppler vibrometry are non-invasive techniques and can provide extremely high sensitivity to changes in optical path length (i.e. in the direction of light propagation) but, for imaging purposes in the transverse direction, they are diffraction-limited with a spatial resolution of a few hundred nanometres at best. Using this method, it's not possible to characterise the individual constituting nanomechanical components in a complex photonic metamaterial.

However, these challenges can be circumvented by using electron beams as demonstrated in Chapter 3. Also, as shown in Chapter 5, a nanostructure's movement in the plane perpendicular to the direction of light propagation can be accurately measured through scattering patterns when light passes through it although with modest picometric sensitivity. Furthermore, movement of nanostructures can be measured by detecting the reflectance or transmittance change when the nanostructures are patterned with optical resonators, such as metamolecules, that are coupled to each other (Chapter 6).

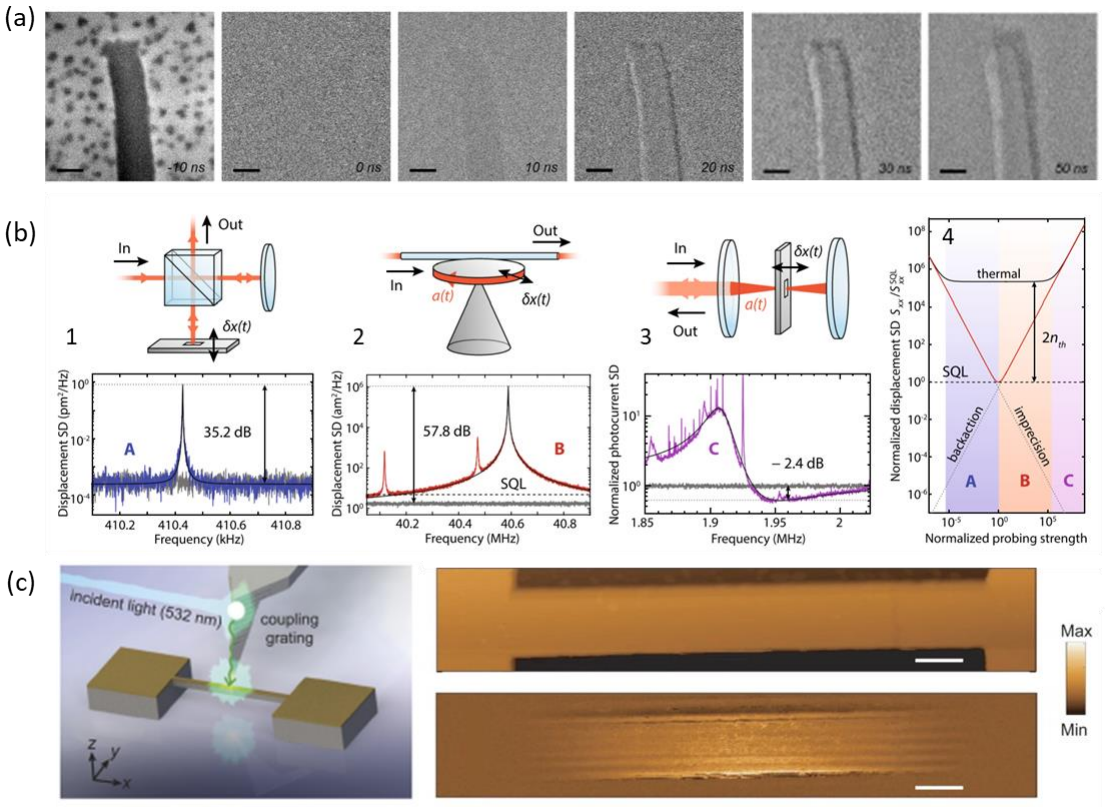

Figure 1.2 **Existing nano-motion imaging techniques.** (a) 4D electron micrographs of the nanoscale cantilever [54]. (b) Probing mechanical motion by laser interferometry [50]. (c) Scanning probe method combined with near-field plasmon sensing [56].

Scanning probe methods: Scanning probe microscopy (SPM) has by now been extended to a wide spectrum of basic and applied fields which plays an important role in the understanding and perception of matter at its nanoscopic and even atomic levels [57]. SPM uses a sharp tip to physically raster-scan samples and locally collect information from the surface. Various signals can be directly detected by SPM in real space with atomic or nanoscale resolution, which provides insights into the structural, electronic, vibrational, optical, magnetic, (bio)chemical and mechanical properties [57].

For example, in the scanning probe microscopy (SPM)-based near-field method as reported in [56], a sharp metallic tip on a microcantilever with a line-grating serves both as a local probe and a local source (Figure 1.2c). The localized surface plasmons are generated and confined at the tip, by tightly

focusing the light onto the tip. The interaction between the tip and the moving device surface scatters the localized plasmons, which are then measured at the far-field with a photodetector. Because the intensity of the optical interaction varies significantly with the distance between the tip and the surface as in apertureless scattering-type near-field optical microscopy, the scattered light collected at the far-field carries information on the oscillations of the mechanical resonator. The reported sensitivity of this technique is about 0.45 pm/$Hz^{1/2}$.

However, the potential concern is that external load from the probe will be introduced which may affect the mechanical properties of device under test. In particular, when measuring the complex nanomechanical photonic metamaterials as illustrated in Figure 1.1, the stiction between neighbouring nanowires as a result of introduced electrostatic and van der Waals interaction may happen after doing raster-scanning measurement. This concern can be overcome when using the electron or light as a probe.

1.3 Layout of this thesis

This thesis reports on the study of the atomic length scale dynamics of thermal and driven motion in photonic nanostructures, such as cantilever or bridge beams - the building blocks of nanomechanical photonic metamaterials and MEMS/NEMS, using secondary electrons, structured light and optomechanical interactions. It specifically focuses on visualization and control of a nanostructures' atomic length scale Langevin dynamics and externally stimulated movement.

In Chapter 2, I provide theoretical background on thermal (Brownian) motion and its Langevin dynamics for both free particles and nanomechanical resonators. It covers the basics of the pure diffusion model, the Langevin model without memory, and the generalized Langevin model with hydrodynamic memory. Thermomechanical displacement power spectral density (PSD) of a nanomechanical resonator is mathematically derived in terms of mechanical eigenfrequency, effective mass and mechanical damping from the Langevin model. Ballistic thermal motion characteristics of a nanomechanical structure at short timescale are also analysed from the Langevin equation. As one of the important parts in my research work, a Brownian parametric oscillator model is also introduced.

In Chapter 3, I develop a motion visualization technique, based upon spectrally resolved detection of secondary electron emission from moving objects, that combines picometric displacement sensitivity with the nanometric spatial (positional/imaging) resolution of electron microscopy. The sensitivity of the technique is quantitatively validated in measurements of the thermodynamically defined amplitude of a nano-cantilever's Brownian motion. It is further demonstrated in application to visualizing externally driven oscillatory modes of cantilever, individual element characterisation

of nanomechanical photonic metamaterial and MEMS device structures. With an electron-shot noise limited floor reaching ~1 pm/$Hz^{1/2}$, it can provide for the study of movements with sub-atomic amplitudes.

Chapter 4 reports on the observation of short-timescale ballistic motion in the flexural mode of a nano-membrane cantilever, driven by thermal fluctuation of flexural phonons, including measurements of ballistic velocities and displacements performed with sub-atomic resolution, using the free electron edge-scattering technique described in Chapter 3. The microsecond temporal resolution is a new dimension in this chapter, i.e. making it possible to access the short timescale ballistic regime.

Chapter 5 reports on an experiment in which the average position of a nanowire with a thermal oscillation amplitude of ~150 pm is resolved in single-shot measurements with absolute error of ~30 pm using superoscillatory light at a wavelength of λ= 488 nm, providing the first example of such sub-Brownian metrology with λ/10,000 resolution. To localize the nanowire, I employ a deep learning analysis of the scattering of topologically structured light, which is highly sensitive to the nanowire's position.

In Chapter 6, I demonstrate the optical detection and control of the picometre scale thermal fluctuation in nano-optomechanical metamaterials. Parametric control of thermal motion of a nano-optomechanical oscillator array via dynamic photothermal tunning and parametric coupling between two distinct optomechanical oscillators are demonstrated as well.

Lastly, a summary of this Thesis is presented in 0, together with possible future, emerging research directions.

Chapter 2 Theoretical background

This chapter starts from a theoretical interpretation of our familiar form of Brownian motion of a free particle, such as the inexhaustible and erratic motion of small pollen grains suspended in water. It firstly introduces Einstein's pure diffusion theory of Brownian motion dating back to 1905 which for the first time physically interpreted the long-time erratic movement, then a stochastic Langevin equation (considering the inertia of a Brownian particle) capable of revealing both the short time scale ballistic and long-time diffusive movement is introduced and a generalized Langevin model that considers the hydrodynamic interaction between fluid and particle is also briefly described.

In the second part, thermal fluctuation in a nanomechanical beam, as the main focus of this thesis, is described using the well-accepted Langevin model for a mechanical oscillator driven by noise in terms of the parameters of effective mass, mechanical eigenfrequency and mechanical damping. Thermomechanical displacement power spectral density, as is widely used in experimental measurements in this thesis (sections 3.4, 4.1, 6.3 and 6.4), is obtained from this model. Ballistic thermal motion characteristics of a nanomechanical structure at short timescale are also derived from the Langevin equation. In section 2.2.3, a numerical modeling of a Brownian nanomechanical oscillator is performed by solving the Langevin equation to better illustrate the thermomechanical movement in different damping regimes and the behavior of ballistic regime thermal movement before coming to the experimental demonstration in section 4.1.

In the third part, the mechanical eigenfrequency of a regular nanomechanical beam with uniform rectangular cross-section is derived from Euler-Bernoulli beam theory [58, 59] considering its geometry and properties of constituting materials, which is an important parameter in the Langevin model. Additionally, the effect of tensile stress on a beam resonator is examined; on one hand this helps explain the variation of mechanical resonance frequencies observed in an array of geometrically identical nanomechanical oscillators (sections 3.4.3 and 6.3); on other hand by tuning the tension within a nanomechanical structure, its thermomechanical vibration frequency can be tuned , which provides a solid theoretical foundation for the parametric control of the thermomechanical vibration of a nanomechanical oscillator array, as experimentally demonstrated in section 6.4. Mode dependent effective mass used in the Langevin model for a mechanical beam is also analytically described. This is an important parameter in the thermomechanical displacement power spectral density of a nanomechanical structure that can be experimentally measured and used to evaluate the displacement sensitivity of a technique such as demonstrated in sections 3.4, 5.4 and 6.3, since its amplitude is thermodynamically related to the physical parameters of the

object. Origins of the mechanical damping are briefly summarised, although it is beyond the scope of the experimental study reported in this thesis.

Lastly, in section 2.4, a Brownian parametric oscillator model is introduced which helps interpret and analyze the experimentally observed probe transmission spectrum evolution in the presence of parametric pumping as will be presented in section 6.4. An analytical solution of this model in the frequency domain is also given with its applicability analyzed from numerical calculations.

2.1 Thermal (Brownian) motion of a free particle and its statistics

Soon after the invention of the optical microscope in the 17th century, the inexhaustible and erratic motion of small pollen grains suspended in a fluid has been observed. Generally, these early observations were interpreted as the motion of living creatures. In 1827, the botanist Robert Brown systematically demonstrated that any small particles suspended in a fluid have such characteristics, even an inorganic grain. Therefore, the explanation for such motion should resort to the realm of physics rather than biology. Since then, this phenomenon has been named after the botanist as Brownian motion. It was not until 1905 that physicists such as Albert Einstein, William Sutherland, and Marian von Smoluchowski [60-62] started to gain a theoretical understanding of Brownian motion. While the existence of atoms and molecules was still open to objection, Einstein explained the phenomenon through a microscopic picture, i.e., the kinetic theory of molecules. If heat is a result of vibrational motion of molecules, a Brownian particle in a fluid should undergo an enormous number of random bombardments by the surrounding fluid molecules and its diffusive motion should be observable [60]. The experimental validation of Einstein's theory by Jean Baptiste Perrin unambiguously verified the atomic nature of matter, which was awarded the Nobel Prize in Physics in 1926 [63, 64]. Since the seminal works in the 1900s, this subject has fostered many fundamental developments on equilibrium and nonequilibrium statistical physics and enriched the applications of fluid mechanics such as the rheology of suspensions [63].

2.1.1 Pure diffusion model and Langevin equation

Einstein's seminal work in 1905 [60] has two innovative aspects: the first part is to connect two transport processes: the mass diffusion of the particle and the momentum diffusion of the fluid [63]. Hence, the diffusion coefficient D can be expressed in terms of the fluid properties [63]:

$$D = \frac{RT}{N_A}\frac{1}{6\pi\mu r_a} \tag{2.1.1}$$

where R is the ideal gas constant, T is the temperature, N_A is Avogadro's number, r_a is the radius of the Brownian particle and μ is the viscosity of the fluid. The second part formulates the diffusion

equation to relate the mass diffusion to the mean square displacement (MSD) [63], which is a measurable quantity. After a long and hard reasoning [60], Einstein calculates the mean square displacement (MSD) $\langle[\Delta x(\tau)]^2\rangle$ in a certain direction say x-direction (see Figure 2.1a) of a Brownian particle at a given observation time interval τ as

$$\langle[\Delta x(\tau)]^2\rangle = 2D\tau \tag{2.1.2}$$

which is proportional to the diffusion constant of the suspended substance D and the observation time τ [60]. Here the angle bracket $\langle\cdots\rangle$ indicates that a statistical ensemble average.

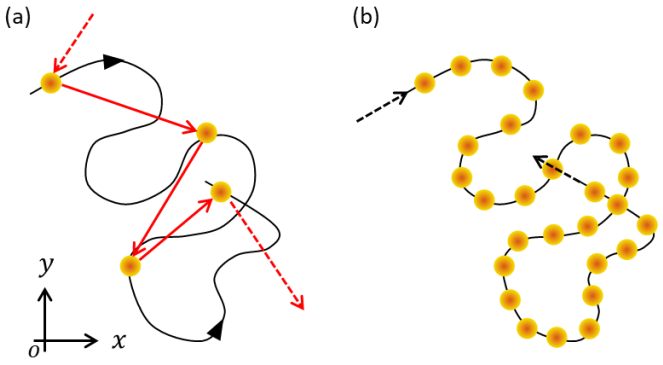

Figure 2.1 **Diffusive versus ballistic Brownian motion.** In the case considered by Einstein (a), the particle's speed and direction have changed many times between measurements (the yellow dots), and the observer sees a diffusive random walk with uncorrelated steps (the red arrows). Measurements made at shorter time intervals (b) resolve the smooth ballistic motion. Arrows indicate the apparent velocities of the particle. Black line shows the particle's trajectory observed with infinitesimal time interval. Images are adapted from [48].

The main criticism of the diffusion model, as Einstein himself realized later [65], is that the inertia of the particle is neglected. This implies that an infinite force is required to change the velocity of the particle to achieve a random walk at each step (Figure 2.1a) [48]. Therefore, its velocity cannot be defined and its trajectories are erratic. Since an apparent velocity is deduced by two consecutive positions, it really depends on the time-resolution of the observations (Figure 2.1). If the observations are separated by a diffusive time scale as in Einstein's model, the particle appears to walk randomly (Figure 2.1a). From the MSD of the diffusion, we may determine an effective mean velocity over a time interval as $v \equiv \sqrt{\langle[\Delta x(\tau)]^2\rangle}/\tau = \sqrt{2D}/\tau$. As τ approaches 0, this effective velocity diverges and cannot represent the real velocity of the particle. Physically, however, we should be able to find a time scale smaller than its momentum relaxation time for the ballistic regime where the velocity does not change significantly (Figure 2.1b), that is the root mean square displacement $\sqrt{\langle[\Delta x(\tau)]^2\rangle}$ is proportional to the observation time interval τ with well-defined velocity $v(0)$, i.e. $\sqrt{\langle[\Delta x(\tau)]^2\rangle} \approx v(0)\tau$.

A remedy for the unphysical feature of Einstein's model at the ballistic time scale was proposed by Paul Langevin [66], which takes into account the inertia of the particle. In Langevin's formulation,

the equation of motion for the Brownian particle is formally based on Newton's second law of motion as

$$m\ddot{x}(t) + \gamma_s \dot{x}(t) = F_{thermal}(t) \tag{2.1.3}$$

where m is the mass of the particle of radius r_a, $\gamma_s = 6\pi\mu r_a$ is the Stokes friction coefficient with μ being the fluid viscosity, and $F_{thermal}(t)$ is a random force on the particle. In this case, the velocity of the particle $v(t) = \dot{x}(t)$ is well-defined and it is subject to two different types of forces exerted by the surrounding fluid: a friction force and random force. It is further assumed that the random force is an independent Gaussian white noise process. Hence, it satisfies following constraints

$$\langle F_{thermal}(t)\rangle = 0, \langle F_{thermal}(t)F_{thermal}(t')\rangle = \Gamma\delta(t-t') \tag{2.1.4}$$

$$\langle F_{thermal}(t)x(t')\rangle = 0, \langle F_{thermal}(t)v(t')\rangle = 0 \tag{2.1.5}$$

Here, $\Gamma = 2\gamma_s k_B T$ represents a fundamental relation named as the fluctuation-dissipation theorem (FDT) [67] with k_B the Boltzmann constant. Roughly speaking, the magnitude of the fluctuation Γ must be balanced by the strength of the dissipation γ_s so that temperature is well defined in Langevin's model. Therefore, the pair of friction and random forces acts as a thermostat for a Langevin system. It should not come as a surprise that the frictional force and the random force have such a relation, since they both come from the same origin of interactions between the particle and the surrounding fluid molecules.

Then, following [63], we obtain an expression for the MSD over the entire time interval range as:

$$\langle[\Delta x(\tau)]^2\rangle = \frac{2k_B T}{\gamma_s}\left(\tau - \frac{m}{\gamma_s} + \frac{m}{\gamma_s}e^{-\tau/(m/\gamma_s)}\right) \tag{2.1.6}$$

On the one hand, for observation time interval much larger than the particle's momentum relaxation time $\tau_b = m/\gamma_s$, i.e., $\tau \gg \tau_b$ (or the massless case $\tau_b = 0$), the exponential term becomes negligible, and we retrieve Einstein's result

$$\frac{d}{d\tau}\langle[\Delta x(\tau)]^2\rangle = \frac{2k_B T}{\gamma_s} = 2D \tag{2.1.7}$$

On the other hand, for $\tau \ll \tau_b$ or $\tau \to 0$, by using the Taylor series $e^{-\tau} = 1 - \tau + \tau^2/2! + O(\tau^3)$ we obtain

$$\langle[\Delta x(\tau)]^2\rangle = \frac{k_B T}{m}\tau^2 \tag{2.1.8}$$

which is identical to the ballistic regime derived from the equipartition theorem, i.e., $\langle v^2(0)\rangle = k_B T/m$. Hence, one can clearly see that Langevin's model can explain the ballistic regime as well as Einstein's long-time diffusion result of the MSD.

2.1.2 Hydrodynamic model: generalized Langevin equation

For completeness, the hydrodynamic model for a Brownian particle is also briefly summarised here although it is not studied experimentally in this thesis. Although the velocity autocorrelation function (VACF) of a Brownian particle was never explicitly measured in the first half of the twentieth century due to experimental challenges, it was widely believed to decay exponentially [63]. When a new era of computational science began in the 1950s, using molecular dynamics (MD) simulations, some pioneers started to realize that the VACF of molecules does not follow strictly an exponential decay, but has a slowly decreasing characteristic [63]. A milestone took place in 1970 when Alder and Wainwright [68] delivered a definite answer for the long persistence of the VACF as an algebraic decay, that is, velocity correlation function $C(t) \sim t^{-d/2}$ for $t \to \infty$. Here d is the dimension of the problem. These observations from computer simulations led to many intriguing questions as to what is missing in the Langevin model. The most suspicious assumption of the Langevin model (and also of the Einstein model) is probably that the friction coefficient γ_s is taken as the solution of the steady Stokes flow, whereas a Brownian particle undergoes erratic movements constantly. Therefore, the steady friction may be valid only if the surrounding fluid becomes quasi-steady immediately after each movement, or less strictly, before the relaxation time of Brownian particle. This deficiency was already pointed out in the early lectures of Hendrik Lorentz that Stokes drag coefficient $\gamma_s = 6\pi\mu r_a$ is a good approximation only when the mass density ratio ρ_f/ρ_B of the fluid and the Brownian particle is so small that the fluid inertia is negligible [63].

Since the seminal work of Alder and Wainwright, it was very soon widely acknowledged that unsteady hydrodynamics plays a significant role in the dynamics of the Brownian particle. Quasi-steady state in the Langevin model can be examined only if we consider the unsteady solution of the hydrodynamics, which has been available for more than a century from the independent works of Basset and Boussinesq [63, 69]. For a free moving rigid particle suspended in a continuum fluid described by the fluctuating hydrodynamics [70], the non-Markovian generalized Langevin equation can be formulated as [71-74]:

$$m\ddot{x}(t) + F_{fr}(t) + F_{ext}(t) = F_{thermal}(t) \tag{2.1.9}$$

For a free spherical particle (i.e. where external force $F_{ext}(t) = 0$) undergoing motion influenced by the inertia of the surrounding fluid, its resistant force was known to Boussinesq and Basset [63, 69]:

$$F_{fr}(t) = -6\pi\mu r_a v(t) - \frac{m_f}{2}\dot{v}(t) - 6\pi\mu r_a\sqrt{\frac{\tau_f}{\pi}}\int_{-\infty}^{t}\frac{\dot{v}(t')}{\sqrt{t-t'}}dt' \tag{2.1.10}$$

where $\tau_f = r_a^2\rho_f/\mu$ denotes the so-called vortex diffusion time and $m_f/2 = 6\pi\mu r_a\tau_f/9 = 2\pi r_a^3\rho_f/3$ is the 'added mass', i.e., the mass of fluid displaced by the Brownian particle. The Basset force arises from vorticity that originates at the surface of an accelerating particle and diffuses outward, expanding to the size of the particle in time τ_f. The strength of the Basset force is proportional to $\sqrt{\mu\rho_f}$. As the density of the surrounding medium approaches zero, so does τ_f and the vorticity diffuses away immediately. As the viscosity approaches zero, the interaction between the particle and the vorticity approaches zero. In the time domain, the sphere-fluid interaction force can be written as

$$F_{fr}(t) = \int_{-\infty}^{t} \gamma(t-t')v(t')\,dt' \tag{2.1.11}$$

where $\gamma(t)$ is the memory kernel. In the angular frequency (ω) domain, the Fourier-Laplace transform of the memory kernel, $\gamma[\omega]$, better illustrates the nature of the Basset force. Compared to the original Langevin equation (2.1.3), Eqn. (2.1.11) is non-Markovian as the friction force is history-dependent. The memory kernel $\gamma(t)$ is the inverse Laplace transform of Eqn. (2.1.10). The explicit form of $\gamma[\omega]$ is

$$\begin{aligned}\gamma[\omega] &= \gamma_s\left(1+\sqrt{-i\omega\tau_f}\right) - \frac{i\omega m_f}{2} \\ &= \gamma_s\left(1+\sqrt{\frac{\omega\tau_f}{2}}\right) - \frac{i\omega m_f}{2}\left(1+9\sqrt{\frac{1}{\omega\tau_f}}\right)\end{aligned} \tag{2.1.12}$$

In the second line here, it has been separated into its real and imaginary parts. The real part contributes to motion in-phase with the external force, corresponding to non-conservative (dissipative) interactions, while the imaginary part contributes to motion out of phase with the force and corresponds to conservative (inertial) interactions.

In addition, the random force $F_{thermal}(t)$ is non-white or coloured, as described by fluctuation-dissipation theorem

$$\langle F_{thermal}(t)F_{thermal}(t+\tau)\rangle = 2\gamma_s k_B T\left(\delta(\tau) - \frac{1}{4}\sqrt{\frac{\tau_f}{\pi}}\tau^{-3/2}\right) \tag{2.1.13}$$

Widom was able to solve this problem analytically and showed the existence of the long-time tail in the velocity autocorrelation function of the Brownian particle [75, 76]:

$$C(t) = \frac{k_B T}{m_{eff}(\varsigma-\varrho)}\left[\varsigma e^{\varsigma^2 t}erfc\left(\varsigma\sqrt{t}\right) - \varrho e^{\varrho^2 t}erfc\left(\varrho\sqrt{t}\right)\right] \tag{2.1.14}$$

where $erfc()$ is the complementary error function, and

$$\varrho = \left[\zeta + \sqrt{\zeta^2 - 4\gamma_s m_{eff}}\right]/2m_{eff}\,, \qquad \varsigma = \left[\zeta - \sqrt{\zeta^2 - 4\gamma_s m_{eff}}\right]/2m_{eff} \tag{2.1.15}$$

In this equation, the shorthand notation $\zeta = 6\pi r_a^2\sqrt{\rho_f \mu}$ has been introduced, with r_a being the radius of the Brownian particle, ρ_f the fluid density, and μ the shear viscosity of the fluid. Furthermore, the effective mass is $m_{eff} = m + \frac{1}{2}m_f$, with m being the mass of the Brownian particle and $m_f = 4\pi r_a^3\rho_f/3$ the mass of the fluid displaced by the Brownian particle. In the limit $t \to 0$, one obtains

$$\lim_{t\to 0} C(t) = \frac{k_B T}{m_{eff}} \tag{2.1.16}$$

This result is in contradiction with the equipartition theorem because the effective mass m_{eff} instead of particle mass m is used. This paradox was solved by Zwanzig and Bixon [77]. They showed that there is a rapid initial decrease from $k_B T/m$ to $k_B T/m_{eff}$ at very short time scales by including compressibility effects in the study of the velocity autocorrelation function. It is easy to determine the long-time behaviour of the velocity autocorrelation function, using the asymptotic expansion of the product of the exponential function and complementary error function. One then obtains for $C(t)$

$$C(t) = k_B T\frac{\zeta}{2\gamma_s^2\sqrt{\pi}}t^{-3/2} + O\left(t^{-3/2}\right) \tag{2.1.17}$$

which shows the famous long-time tail.

In an analogous way one can obtain an expression for the mean-square displacement [76]:

$$\begin{aligned}\langle[\Delta x(\tau)]^2\rangle = 2D\Bigg(\tau - \frac{2\zeta}{\gamma_s\sqrt{\pi}}\sqrt{\tau} + \frac{\left(\zeta^2 - \gamma_s m_{eff}\right)}{\gamma_s^2} \\ + \frac{\gamma_s}{m_{eff}(\varsigma - \varrho)}\left[\varsigma^{-3}e^{\varsigma^2\tau}erfc\left(b\sqrt{\tau}\right) - \varrho^{-3}e^{\varrho^2\tau}erfc\left(\varrho\sqrt{\tau}\right)\right]\Bigg)\end{aligned} \tag{2.1.18}$$

This expression had already been presented by Paul and Pusey [78], and Weitz *et al.* presented measurements which support this expression [79]. In the limit of large τ we obtain the familiar result

$$\langle[\Delta x(\tau)]^2\rangle = 2D\tau \tag{2.1.19}$$

2.2 Thermal fluctuation in a nanomechanical structure

Classical Brownian motion experiments reveal how a microscopic particle is driven in chaotic motion externally by collisions with molecules of ambient gas or liquid. According to the fluctuation-dissipation theorem [80], in a nanomechanical structure, Brownian motion can be driven in several ways [30, 81] including the collisions of phonons with the walls of the nanostructure [82] and collisions with the ambient molecules. It also may come from the emission and absorption of thermal photons. Vibrations transfer from the clamped end may contribute to it as well [30]. These both introduce random impulses that induce Brownian motion and dampen the oscillations to reach equilibrium [80].

The majority of nanomechanical photonic metamaterials are constructed from cantilevers or doubly clamped beam-like components of microscopic length and nanoscopic cross section. The thermal motion of such structures under vacuum as the case studied in this thesis is driven internally by momentum transfer resulting from the interference, annihilation and creation of incoherent flexural phonons in the main mechanical modes. (The emission and absorption of thermal photons are not important due to the low momentum of such photons and the bad optical cavity.)

Thermomechanical vibration of a nanomechanical structure, such as a cantilever or bridge beam, can be modelled as a trapped particle's Brownian motion where external restoring force is considered, i.e. the Langevin equation with restoring force for this system [83]. Here, for a nanomechanical beam, assuming that the mechanical mode spectrum is sufficiently sparse such that there is no spectral overlap with other mechanical modes and ignoring the hydrodynamic interaction where mass density ratio ρ_s/ρ of the surrounding medium and the mechanical beam is so small that the surrounding media's inertia is negligible [63, 71-74], the motion of a nanomechanical beam $x(t)$ at a particular mechanical mode in a certain direction say x (Figure 2.2) can be modelled as a 1-dimensional damped harmonic oscillator driven by the random thermal force as described by the Langevin equation [30, 58, 83-85]:

$$\ddot{x}(t) + \gamma_m \dot{x}(t) + \omega_m^2 x(t) = F_{thermal}(t)/m_{eff} \tag{2.2.1}$$

$$F_{thermal}(t) = \sqrt{2k_B T \gamma_m m_{eff}}\,\eta(t) \tag{2.2.2}$$

Here, ω_m, m_{eff} and γ_m and are its undamped angular frequency (as will be discussed in section 2.3.1), effective mass (see section 2.3.2) and dissipation factor ($\gamma_m = \gamma_s/m_{eff}$ compared with Eqn. (2.1.3); its origins are summarised in section 2.3.3) for a nanomechanical structure. k_B is the Boltzmann constant and T is the environment temperature. The random thermal force $F_{thermal}(t)$

is a white noise which is related to friction and temperature through fluctuation dissipation theorem [80]. Equation (2.2.2) gives the amplitude of this thermal noise explicitly in terms of γ_m, the Boltzmann energy $k_B T$, and $\eta(t)$, which is a normalized white-noise, hence $\langle \eta(t) \rangle = 0$; $\langle \eta(t)\eta(t') \rangle = \delta(t - t')$ for all *t*, *t'*. Here the angle bracket $\langle \dots \rangle$ indicates ensemble average.

If one measures the motion of a single harmonic oscillator in thermal equilibrium, one will observe a displacement $x(t)$ (Figure 2.2) oscillating at the damped angular frequency $\omega_1 = \sqrt{\omega_m^2 - (\gamma_m/2)^2}$. Due to the influence of both mechanical damping and the fluctuating thermal Langevin force, these oscillations will have a randomly time-varying amplitude and phase [30]. Both amplitude and phase change on the time scale given by the momentum relaxation time or damping time $\tau_b = \gamma_m^{-1}$. A figure of merit to quantify this damping is the dimensionless quality factor Q which is defined as

$$Q = 2\pi \left(\frac{Total\ energy}{Energy\ lost\ per\ cycle} \right) \tag{2.2.3}$$

In the limit of small damping rate, $\gamma_m \ll \omega_m$, the quality factor can be approximated by $Q = \omega_m/\gamma_m$. Essentially, the quality factor gives the number of cycles that are needed for the system to lose its energy to the environment.

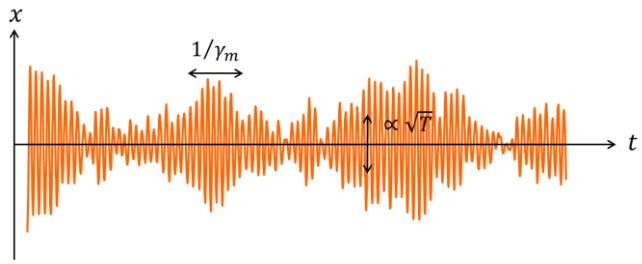

Figure 2.2 **Thermomechanical movement of a damped nanomechanical oscillator.** Brownian motion (thermal fluctuations) of a nanomechanical resonator in the time domain, with amplitude fluctuating on a time scale set by the damping time $1/\gamma_m$. The variance of position is proportional to the environment temperature.

2.2.1 Thermomechanical displacement power spectral density

Thermomechanical displacement power spectral density (PSD), a spectral representation of thermal motion in the frequency domain, is equal to the Fourier transform of the displacement autocorrelation function [85] and is widely used in experimental measurements as shown in sections 3.4, 4.1, 6.3 and 6.4. It can be directly derived from the Langevin equation.

Usually, it is convenient to study a thermomechanical oscillator in the frequency domain. By transforming the Langevin equation Eqn. (2.2.1) to the frequency domain, one can obtain:

$$-\omega^2 x(\omega) - i\omega\gamma_m x(\omega) + \omega_m^2 x(\omega) = F_{thermal}(\omega)/m_{eff} \tag{2.2.4}$$

Therefore,

$$x(\omega) = \chi(\omega)F_{thermal}(\omega) = \frac{F_{thermal}(\omega)}{m_{eff}}\frac{1}{\omega_m^2 - \omega^2 - i\gamma_m\omega} \tag{2.2.5}$$

where $F_{thermal}(\omega) = \sqrt{2k_BT\gamma_m m_{eff}}$. This expression describes the linear response of the mechanical oscillator in the frequency space, where a force $F_{thermal}(\omega)$ leads to a mechanical response $x(\omega)$, which is defined by the mechanical susceptibility $\chi(\omega)$ [85] that is given by

$$\chi(\omega) = \frac{1}{m_{eff}[\omega_m^2 - \omega^2 - i\gamma_m\omega]} \tag{2.2.6}$$

The double-sided displacement power spectral density (PSD) is defined as [86]: $S_{xx}(\omega) = |x(\omega)|^2$, so

$$S_{xx}(\omega) = \frac{2k_BT\gamma_m}{m_{eff}}\frac{1}{(\omega_m^2-\omega^2)^2 + \gamma_m^2\omega^2} \tag{2.2.7}$$

which describes how the power of the quantity $x(t)$ is distributed in the frequency space. And the double-sided velocity spectral density is $S_{vv}(\omega) = \omega^2 S_{xx}(\omega)$

$$S_{vv}(\omega) = \frac{2k_BT\gamma_m}{m_{eff}}\frac{\omega^2}{(\omega_m^2-\omega^2)^2 + \gamma_m^2\omega^2} \tag{2.2.8}$$

Therefore, the single-sided (containing only positive frequency components) thermomechanical displacement power spectral density (PSD) of a nanomechanical resonator (i.e., $S_x = 2S_{xx}$), in terms of its effective mass m_{eff}, quality factor $Q = \omega_m/\gamma_m$ and resonant frequency $f_m = \omega_m/2\pi$, is

$$S_x(\omega) = \frac{4k_BT\gamma_m}{m_{eff}}\frac{1}{(\omega_m^2-\omega^2)^2 + \gamma_m^2\omega^2} \tag{2.2.9}$$

with a typical resonance curve shown in Figure 2.3a. Or in the frequency domain

$$S(f) = \frac{k_BTf_m}{2\pi^3 m_{eff}Q[(f_m^2 - f^2)^2 + (ff_m/Q)^2]} \tag{2.2.10}$$

with units of m^2/Hz, which is widely used and can be measured experimentally as shown in sections 3.4, 4.1, 6.3 and 6.4.

Moreover, it can be shown in later section 2.2.2 that the mean square of the quantity $x(t)$ is the area under the power spectral density [85]

$$\langle x^2 \rangle = \frac{1}{2\pi}\int_{-\infty}^{+\infty} S_{xx}(\omega)\, d\omega = \int_{-\infty}^{+\infty} S_{xx}(f)\, df \tag{2.2.11}$$

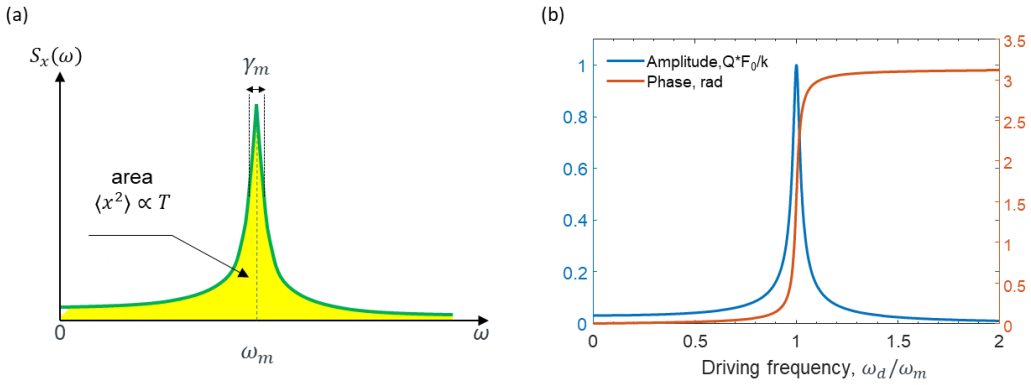

Figure 2.3 **Mechanical movement of a damped oscillator.** (a) Single-sided thermomechanical displacement power spectral density in thermal equilibrium. (b) Mechanical motion amplitude and phase response under external stimuli.

In thermal equilibrium, the mean mode energy of the harmonic mechanical oscillator, $\langle E \rangle$, is given by the sum of kinetic and potential energies

$$\langle E \rangle = \frac{1}{2} m_{eff} \langle v^2 \rangle + \frac{1}{2} k \langle x^2 \rangle \tag{2.2.12}$$

where $\langle x^2 \rangle$ is the mean square thermal displacement and $\langle v^2 \rangle$ is the mean square velocity in thermal equilibrium. From the equipartition theorem we get individual equipartition of the kinetic and the potential energies:

$$\frac{1}{2} m_{eff} \langle v^2 \rangle = \frac{1}{2} k \langle x^2 \rangle = \frac{1}{2} k_B T \tag{2.2.13}$$

Using the last equation and spring constant $k = m_{eff}\omega_m^2$ we get the mean square thermal displacement

$$\langle x^2 \rangle = \frac{k_B T}{m_{eff}\omega_m^2} \tag{2.2.14}$$

This provides an evaluation of the variance of thermal motion for a nanomechanical structure as used in sections 3.4.1, 4.1, 5.4.2 and 6.3. And the root-mean-square thermal motion amplitude and velocity are respectively

$$\sqrt{\langle x^2 \rangle} = \sqrt{\frac{k_B T}{m_{eff}\omega_m^2}}, \quad \sqrt{\langle v^2 \rangle} = \sqrt{\frac{k_B T}{m_{eff}}} \tag{2.2.15}$$

Furthermore, from equation (2.2.11) we obtain that the area under the single-sided mechanical thermal noise spectrum of a mechanical harmonic oscillator equals the variance of its displacement

$$\langle x^2 \rangle = \frac{1}{2\pi}\int_0^{+\infty} S_x(\omega)\, d\omega = \int_0^{+\infty} S_x(f)\, df = \frac{k_B T}{m_{eff}\omega_m^2} \tag{2.2.16}$$

as illustrated in Figure 2.3a.

For a mechanical damped harmonic oscillator driven by a coherent force $F(t) = F_0 \cos(\omega_d t)$, in the angular frequency domain, the amplitude response $x(\omega_d)$ is given by

$$x(\omega_d) = \frac{F_0/m_{eff}}{\sqrt{(\omega_m^2 - \omega_d^2)^2 + \gamma_m^2 \omega_d^2}} \tag{2.2.17}$$

and the phase $\phi(\omega_d)$ by

$$\phi(\omega_d) = \tan^{-1}\left(\frac{\gamma_m \omega_d}{\omega_m^2 - \omega_d^2}\right) \tag{2.2.18}$$

By applying an inverse Fourier transform, we can also obtain the displacement in the time domain

$$x(t) = \frac{\omega_m}{\gamma_m}\frac{F_0}{m_{eff}\omega_m^2}\sin\omega_d t = Q\frac{F_0}{m_{eff}\omega_m^2}\sin\omega_d t = Q\frac{F_0}{k}\sin\omega_d t \tag{2.2.19}$$

$k = m_{eff}\omega_m^2$ being the spring constant. On resonance ($\omega_d = \omega_m$), the motion is $\pi/2$ out of phase with the driving force (see Figure 2.3b), and the motional amplitude reaches a maximum, which is proportional to the quality factor Q.

2.2.2 Ballistic thermal motion statistics

In Chapter 4, I present experimental observations of short-timescale ballistic motion of a nano-membrane cantilever. This regime can be understood starting from the Langevin equation for the thermal motion of a damped harmonic oscillator in one dimension, which is given by Eqn. (2.2.1). In the following, the ballistic motion characteristics in terms of mean square displacement (MSD) at short-timescale are mathematically revealed for underdamped, critically damped and overdamped Brownian oscillators.

The Wiener-Khinchin theorem [30, 85] states that the power spectral density of a wide-sense stationary random process $S_{xx}(\omega)$, i.e., a stochastic process with a constant mean (here $x(t)$), is equal to the Fourier transform of its autocorrelation function $C_x(\tau) = \langle x(t)x^*(t+\tau)\rangle$, and vice versa:

$$S_{xx}(\omega) = \int_{-\infty}^{+\infty} d\tau e^{-i\omega\tau}\langle x(t)x^*(t+\tau)\rangle \tag{2.2.20}$$

where $*$ means the complex conjugate and can be ignored because quantity $x(t)$ here is real-valued function. Therefore, position autocorrelation $\langle x(t)x(t+\tau)\rangle$ here is the inverse Fourier transform of displacement power spectral density

$$\begin{aligned}\langle x(t)x(t+\tau)\rangle &= \frac{1}{2\pi}\int_{-\infty}^{+\infty} S_{xx}(\omega)e^{i\omega\tau}d\omega \\ &= \frac{1}{2\pi}\int_{-\infty}^{+\infty}\frac{2k_BT\gamma_m}{m_{eff}}\frac{1}{(\omega_m^2-\omega^2)^2+\gamma_m^2\omega^2}d\omega\end{aligned} \tag{2.2.21}$$

The above integration kernel has four singularities, when $(\omega_m^2-\omega^2)^2+\gamma_m^2\omega^2=0$, with

$$\omega = \pm\frac{i\gamma_m}{2}\pm\sqrt{\omega_m^2-(\gamma_m/2)^2} \tag{2.2.22}$$

The damped angular frequency defined as

$$\omega_1 = \sqrt{\omega_m^2-(\gamma_m/2)^2} \tag{2.2.23}$$

Depending upon the value of ω_1, one can identify three different regimes: $\omega_1 > 0$ corresponds to an underdamped oscillator; $\omega_1 = 0$: critically damped oscillator; $\omega_1$complex value: overdamped oscillator. The integral in equation (2.2.21) can be calculated as a contour integral in the complex plane of ω by taking the residues at the poles located at values of equation (2.2.22) while only considering the upper half semi-circle because of the observation time interval $\tau > 0$.

For under/over damped cases, we can get the position autocorrelation function:

$$\langle x(t)x(t+\tau)\rangle = \frac{k_BT}{m_{eff}\omega_m^2}e^{-\frac{\tau}{2\tau_b}}\left(cos\omega_1\tau+\frac{sin\omega_1\tau}{2\omega_1\tau_b}\right) \tag{2.2.24}$$

with momentum relaxation time $\tau_b = 1/\gamma_m$. Note that at $\tau = 0$, $\langle x^2(t)\rangle = k_BT/\left(m_{eff}\omega_m^2\right)$ – corresponding simply to equipartition theorem $1/2\, m_{eff}\omega_m^2\langle x^2(t)\rangle = 1/2k_BT$.

The mean squared displacement (MSD) $\langle[\Delta x(\tau)]^2\rangle$ of a Brownian underdamped harmonic oscillator – a measure of average distance travelled at a given time interval τ (the orange line in Figure 4.3a), can thus be obtained through $\langle[\Delta x(\tau)]^2\rangle = \langle|x(t)-x(t+\tau)|^2\rangle = 2\langle x^2(t)\rangle - 2\langle x(t)x(t+\tau)\rangle$ as:

$$MSD(\tau) = \langle|x(t)-x(t+\tau)|^2\rangle = \frac{2k_BT}{m_{eff}\omega_m^2}\left[1-e^{-\frac{\tau}{2\tau_b}}\left(cos\omega_1\tau+\frac{sin\omega_1\tau}{2\omega_1\tau_b}\right)\right] \tag{2.2.25}$$

For the critically damped case, the position correlation function reads

$$\langle x(t)x(t+\tau)\rangle = \frac{k_B T}{m_{eff}\omega_m^2} e^{-\frac{\tau}{2\tau_b}}(1+\tau/\tau_b) \tag{2.2.26}$$

And mean square displacement is

$$MSD(\tau) = \langle |x(t)-x(t+\tau)|^2\rangle = \frac{2k_B T}{m_{eff}\omega_m^2}\left[1-\left(1+\frac{\tau}{2\tau_b}\right)e^{-\frac{\tau}{2\tau_b}}\right] \tag{2.2.27}$$

For short time scales $\tau \ll \tau_b$ or $\tau \to 0$, by using the Taylor series $e^{-t} = 1 - t + t^2/2! + O(t^3)$, $\sin(t) = t + O(t^3)$ and $\cos(t) = 1 - t^2/2! + O(t^4)$, one obtains respectively from equations (2.2.25) and (2.2.27),

$$MSD(\tau) = \frac{2k_B T}{m_{eff}\omega_m^2}\left[1-\left(1-\frac{\tau}{2\tau_b}+\frac{\tau^2}{8\tau_b^2}+O(\tau^3)\right)\left(1+\frac{\tau}{2\tau_b}-\frac{\omega_1^2\tau^2}{2}+O(\tau^3)\right)\right] \tag{2.2.28}$$

$$MSD(\tau) = \frac{2k_B T}{m_{eff}\omega_m^2}\left[1-\left(1+\frac{\tau}{2\tau_b}\right)\left(1-\frac{\tau}{2\tau_b}+\frac{\tau^2}{8\tau_b^2}+O(\tau^3)\right)\right] \tag{2.2.29}$$

Using equation (2.2.23) and $\tau_b = 1/\gamma_m$ (i.e., $\omega_1 = \sqrt{\omega_m^2 - 1/(2\tau_b)^2}$) to simplify these expressions, one obtains the ballistic behavior, respectively, of an under/over damped oscillator with $\omega_1 = \sqrt{\omega_m^2 - 1/(2\tau_b)^2}$ (the purple line in in Figure 4.3a):

$$MSD^{Ballistic}(\tau) = \frac{2k_B T}{m_{eff}\omega_m^2}\left(\frac{1}{8\tau_b^2}+\omega_1^2\right)\tau^2 = \frac{k_B T}{m_{eff}}\tau^2 \tag{2.2.30}$$

and for a critically damped oscillator $\omega_1 = 0$, i.e., $\omega_m^2 = 1/(2\tau_b)^2$

$$MSD^{Ballistic}(\tau) = \frac{2k_B T}{m_{eff}\omega_m^2}\frac{\tau^2}{8\tau_b^2} = \frac{k_B T}{m_{eff}}\tau^2 \tag{2.2.31}$$

which is proportional to the square of observation time interval with velocity identical to the one derived from the equipartition theorem, i.e., $\langle v^2(0)\rangle = k_B T/m$. The velocity autocorrelation function (VACF) can be obtained by similar means considering Eqn. (2.2.9):

$$\langle v(t)v(t+\tau)\rangle = \frac{1}{2\pi}\int_{-\infty}^{+\infty} S_{vv}(\omega)e^{i\omega\tau}d\omega \tag{2.2.32}$$

Using contour integration, the VACF for an underdamped Brownian oscillator is then given by:

$$\langle v(t)v(t+\tau)\rangle = \frac{k_B T}{m_{eff}} e^{-\frac{\tau}{2\tau_b}}\left(cos\omega_1\tau - \frac{sin\omega_1\tau}{2\omega_1\tau_b}\right) \tag{2.2.33}$$

The normalized velocity autocorrelation function (NVACF), quantifying similarity between the velocity v after time τ and the initial velocity (the orange line in Figure 4.3b), is

$$NVACF = \psi(\tau) = e^{-\frac{\tau}{2\tau_b}}\left(\cos\omega_1\tau - \frac{\sin\omega_1\tau}{2\omega_1\tau_b}\right) \tag{2.2.34}$$

showing an exponential decay in the envelope with increasing time.

2.2.3 Numerical calculation of Langevin equation

To better illustrate the thermomechanical movement and its ballistic thermal motion characteristics, numerical calculation was performed to study Brownian dynamics of a damped harmonic oscillator by solving Eqn. (2.2.1) using the method described in [83, 84], where equation (2.2.1) can be rewritten as two coupled first-order differential equations in terms of position $x(t)$ and velocity $\dot{x}(t)$ with given initial values of 0. Random noise $\eta(t) \sim N(0,1)$ in equation (2.2.2) is implemented as a series of random numbers generated from the standard normal distribution (with mean 0 and standard deviation 1). Parameters for a Brownian oscillator of effective mass (m_{eff} = 47 pg) and oscillating angular frequency ($\omega_m = 2\pi f_0$ = 2π×5.7 kHz) used in the simulation are obtained from our experimental sample as will be presented in Chapter 4. The displacements of the oscillator at room temperature (T = 300 K) for three different regimes according to equation (2.2.23): underdamped ($\gamma_m = 0.2\omega_m$), critically damped ($\gamma_m = 2\omega_m$) and overdamped ($\gamma_m = 4\omega_m$) regimes are simulated as shown in Figure 2.4.

Figure 2.4a shows the simulated real time positions in the underdamped (red), critically damped (green), and overdamped (blue) regimes. Note that all three regimes have the same mean (zero) and variance ($k_B T/\left(m_{eff}\omega_m^2\right)$). Only at short times as shown in the inset, does the difference between the three regimens reveal itself: the position coordinate of the underdamped system oscillates, while the position coordinate of the overdamped system does not show discernible persistence of motion. The position coordinate of the critically damped system looks at times like it oscillates, but actually only displays positively correlated random motion.

As can be seen from Figure 2.4b, the numerically calculated displacement power spectral density agrees very well with the analytical description given by Eqn. (2.2.10). The resonance peak in the frequency spectrum is disappearing with the increasing mechanical damping. The high frequency tails contain the ballistic movement information which all display a f^{-4} decrease as indicated by the purple dashed lines, while the overdamped case also displays a f^{-2} decrease as indicated by the blue dashed line, which is attributed to the diffusive motion.

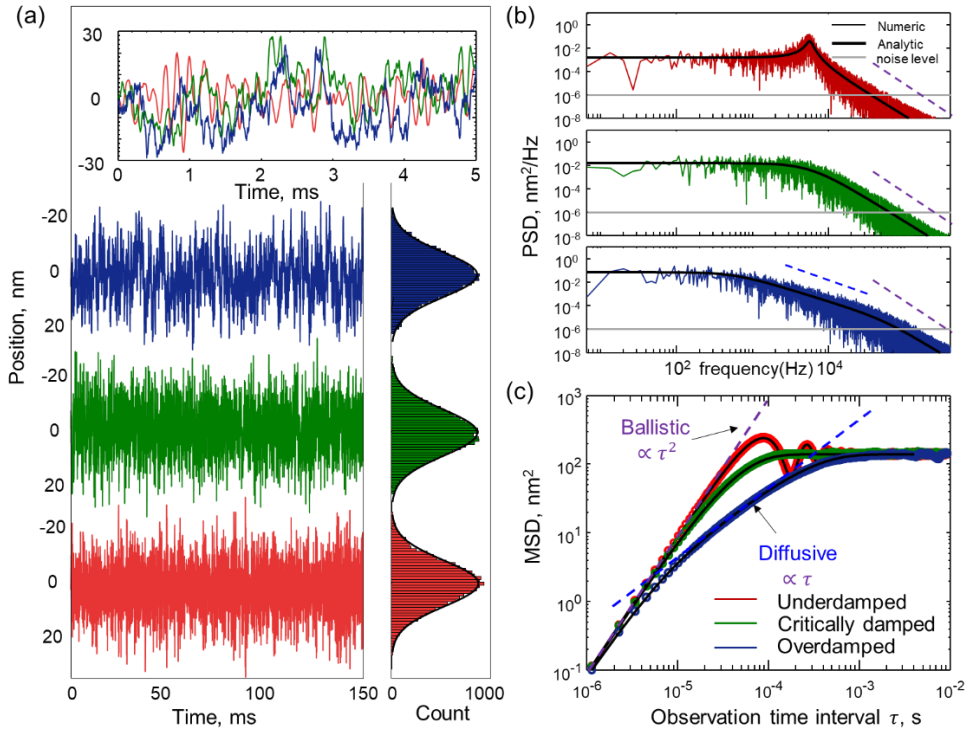

Figure 2.4 **Numerical calculation of Langevin model for a thermomechanical oscillator.** (a) Positions of a damped nanomechanical oscillator (a cantilever in its fundamental mode) in a thermal bath. Three different regimes are studied by varying the dissipation factor γ_m above and below the critical value $2\omega_m$: Underdamped [red, $\gamma_m = 0.2\omega_m$, critically damped [green, $\gamma_m = 2\omega_m$], and overdamped [blue, $\gamma_m = 4\omega_m$]. The inset shows a magnified portion of the trace, revealing the oscillating, critical, and random nature of the motion, respectively. On the right, histograms show the distribution of the position data with $k_BT/(m_{eff}\omega_m^2)$ - variance Gaussians overlaid. (b) Displacement power spectral density (PSD) for three regimes. The black line is derived from the Langevin model for thermal motion of a harmonic oscillator given by equation (2.2.10) in frequency domain. Dashed blue and purple lines illustrate f^{-2} and f^{-4} behaviors, respectively, here f represents frequency. (c) Mean square displacement (MSD) of the position for three different regimes with fitting line according to equations (2.2.25) for under/overdamped oscillators and equation (2.2.27) for a critically damped oscillator.

However, when a time series of positions is examined, the first measure applied is frequently the mean square displacement (MSD) at a given time interval as shown in Figure 2.4c. We can see in all three regimes the mean square displacement has the time square dependence at short time interval indicating the ballistic motion with characteristic $MSD(\tau) = (k_BT/m_{eff})\tau^2$ as eye-guided by the purple dashed line. And only in the overdamped regime we can see the transition from ballistic regime to diffusive regime ($MSD(\tau) \propto \tau$). Finally, MSDs in three regimes all plateau at the same level $2\,k_BT/(m_{eff}\omega_m^2)$ for time lags larger than 1 ms.

2.3 Mechanical properties of a nanomechanical structure

The parameters of mechanical eigenfrequency and effective mass used in the Langevin model for a nanomechanical structure are detailed in the following sections considering its geometry and constituting materials. Mechanical resonances of a nanomechanical beam under stress is also examined, this explains the variation of mechanical resonant frequencies observed in an array of

geometrically identical nanomechanical oscillators (sections 3.4.3 and 6.3). The origin of mechanical damping of a nanomechanical structure is also briefly reviewed in section 2.3.3.

2.3.1 Mechanical eigenfrequency in a nanomechanical structure

Mechanical motion in nanostructures results from their intrinsic elasticity and extrinsic clamping conditions, which lead to a restoring force towards a given equilibrium position. The motion is characterized by a set of orthogonal eigenmodes each having a distinct resonance frequency and displacement shape, which are obtained by solving the characteristic elastic equations [59, 85]. A large number of nano/micro-mechanical resonators possess beam-like geometries and can be effectively modelled as macroscopic beam-like structures. The Euler-Bernoulli beam model is used to model the bending behaviour of slender beams (ratio of length to thickness of more than ten, L/h > 10) under the assumption that the beam has no shear deformation and rotational inertia [59, 85]. For simple geometries, such as a stress-free singly clamped (cantilever) or doubly clamped beam (bridge), analytical solutions can be found in [59, 85] and the nth mode frequency of the beam is given by

$$f_n = \frac{\lambda_n^2}{2\pi L^2}\sqrt{\frac{YM}{\rho A_c}} \tag{2.2.35}$$

where λ_n is a mode dependent dimensionless parameter; L, Y, M, ρ, and A_c are the length, Young's modulus, second moment of inertia, mass density, and cross-sectional area of the mechanical beam. Values λ_n for flexural modes of a singly clamped cantilever and doubly clamped bridge beam are shown in Table 2.1.

Table 2.1 Value of mode dependent parameter λ_n for cantilever and bridge

Mode number (n)	λ_n	
	Singly clamped beam (Cantilever)	**Doubly clamped beam (Bridge)**
1	1.8751	4.7300
2	4.6941	7.8532
3	7.8548	10.9955
n>3	$(n-1)\pi + \pi/2$	$n\pi + \pi/2$

For a one-material beam with rectangular cross-section (width w and thickness h), in which the second moment of inertia is $M = \iint z^2 dA_c = wh^3/12$, the nth out-of-plane flexural mode along the thickness direction has natural frequency

$$f_n = \frac{\lambda_n^2 h}{2\pi\sqrt{12}L^2}\sqrt{\frac{Y}{\rho}} \tag{2.2.36}$$

where h, L is the structure's thickness and length, while the natural frequency of in-plane mode is

$$f_n = \frac{\lambda_n^2 w}{2\pi\sqrt{12}L^2}\sqrt{\frac{Y}{\rho}} \tag{2.2.37}$$

with beam's width w.

A comparison between the analytical formulas and simulations can be performed for the simple case of a uniform beam such as a singly clamped cantilever and doubly clamped bridge beam. Considering a stress-free silicon nitride (Si_3N_4) beam with length L = 20 µm, thickness h = 100 nm, width w = 200 nm, Young's modulus Y = 260 GPa, density ρ = 3100 kg/m^3 and using Equation (2.2.36) we can calculate its mechanical eigenfrequencies analytically for the first three flexural modes along the thickness direction. For the first three flexural modes of cantilever (bridge) beam, we find the mechanical eigenfrequencies are 0.370 MHz (2.353 MHz) and 2.318 MHz (6.487 MHz), 6.490 MHz (12.718 MHz) respectively. These values are in good agreement with those obtained from finite element method (FEM) modelling using COMSOL Multiphysics as shown in Figure 2.5 for a cantilever (bridge) beam 0.370 MHz (2.360 MHz) and 2.321 MHz (6.508 MHz), 6.500 MHz (12.765 MHz) respectively.

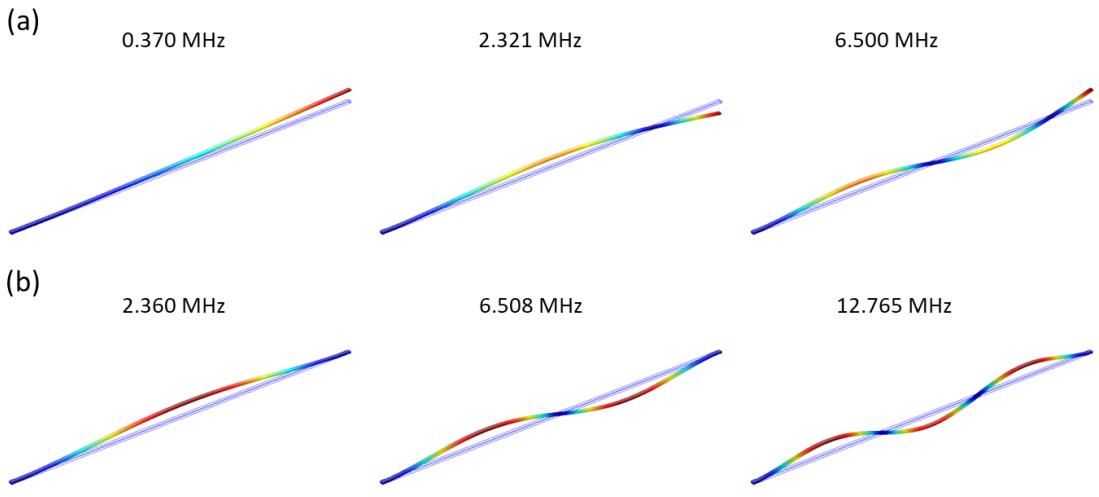

Figure 2.5 **Mode shape and frequencies of the first three modes of a stress-free silicon nitride beam.** (a) Cantilever's first 3 out-of-plane flexural modes. (b) Bridge's first three out-of-plane flexural modes.

The simple case described in the above assumes that there is no stress in the beam. However, thin films and membranes used in beam fabrication are usually pre-stressed either as a consequence of their fabrication procedure or by design. In free-standing membranes for instance, high stress is

favoured as it enhances the quality factor of their mechanical resonances. In beam structures, increase of tensile stress leads to higher resonance frequencies. Following [59] the presence of tensile stress σ in a beam results in resonance frequencies

$$f_n = \frac{\lambda_n^2}{2\pi L^2}\sqrt{\frac{YM}{\rho A_c}}\sqrt{1+\frac{\sigma A_c L^2}{YM\lambda_n^2}} \tag{2.2.38}$$

which is Eqn. (2.2.35) multiplied by a term that increases with stress. Therefore, the eigenfrequency of a stressed beam is the eigenfrequency of the beam under zero stress multiplied by the stress dependent term. This shows that an increase of tensile stress in a beam will increase its resonance frequency. Therefore, tuning of the internal stress in a nanomechanical structure can provide tunable frequency response (the same is true with tuning the strings of a musical instrument via tension). By tuning the tensile stress within a nanomechanical structure, its thermomechanical vibration frequency can be tuned, which provides a method for controlling of the thermomechanical vibration of nanomechanical oscillator arrays, as demonstrated in section 6.4. For a geometrically complex nanostructures, such as bridge beams patterned with optical antennas, finite element numerical simulation (e.g. COMSOL) can be used to identify the structure's mechanical eigenfrequencies and mode shapes.

2.3.2 Effective mass of a nanomechanical structure

Effective mass of a nanomechanical structure is an important parameter in its thermomechanical displacement power spectral density and provides a non-invasive calibration method or reference to evaluate the displacement sensitivity of a technique as illustrated in sections 3.4.1, 5.4.2 and 6.3. This section derives the effective mass for a nanomechanical beam that is used in the Langevin equation. The effective mass $m_{eff,n}$ of a nanomechanical structure, usually mechanical mode-shape dependent, relates its potential energy E_p to its nth eigenfrequency f_n and maximum displacement d_n^* through the expression

$$E_p = \frac{1}{2}m_{eff,n}\omega_n^2|d_n^*|^2 \tag{2.2.39}$$

Potential energy can be determined through a volume integral

$$E_p = \frac{1}{2}\omega_n^2\int \rho(r)|d_n(r)|^2 dV \tag{2.2.40}$$

where $d_n(r)$ is the spatial displacement distribution ('shape') of the nth mode and $\rho(r)$ is the spatial density distribution of the structure. Combining these two equations gives

$$m_{eff,n} = \int \rho(r) \left| \frac{d_n(r)}{d_n^*} \right|^2 dV = \int \rho(r) |R_n(r)|^2 dV \quad (2.2.41)$$

where $R_n(r)$ is the normalized displacement at position r for the nth mode.

In some cases [85, 87] (e.g. ideal cantilevers, strings, and rectangular membranes of uniform density distribution) the ratio of effective to physical mass m_{eff}/m assumes a single mode-independent value for the geometry. In others (doubly-clamped beams, circular membranes), there are well-established sets of mode-dependent values. In the general case, such as the nanomechanical photonic metamaterial (section 6.3), the above volume integral can be evaluated numerically, for example via finite element modelling.

For a single-material cantilever beam of uniform rectangular cross-section, its effective mass is a quarter of its real mass $m_{eff} = 0.25m$, while $m_{eff} = 0.4m$ for a single-material bridge beam. And the spring constant for a bridge beam $k = m_{eff}\omega_1^2$ at fundamental mode is 65 times that of the cantilever beam having the same geometry meaning that the bridge's displacement is 1/65 of that of a cantilever under the same exerted force.

Considering a 20 µm long, 100 nm thick and 200 nm wide silicon nitride (material parameters shown in Table 2.2) doubly-clamped nanomechanical beam having picogram-scale effective mass, they are expected to oscillate at their fundamental mode around 2 MHz by a root-mean-square thermal motion amplitude of 100 picometres which is atomic scale (e.g. the van der Waals diameter of a silicon atom is ~220 pm) at room temperature. The instaneous velocity of ballistic thermal motion is expected to be 3 mm/s meaning that it will move an average of 3 pm within 1 ns.

Table 2.2 Material properties used throughout this thesis

Materials	**Young's modulus Y (GPa)**	**Mass density ρ (kg/m^3)**	**Thermal conductivity κ (W·m^{-1}·K^{-1})**	**Heat capacity C_p (J·kg^{-1}·K^{-1})**
Si_3N_4	260	3100	2.5 [88]	700
Au	70	19300	300	129
amorphous Si	170	2330	1.5 [89]	700

2.3.3 Mechanical dissipation in a nanomechanical structure

The mechanical damping of a nanomechanical structure is ambient pressure dependent and there are three pressure regimes that can be distinguished: the intrinsic, the molecular and the viscous regime [58, 90-92]. A different dominant dissipation mechanism occurs in each of these regimes. In

the experimental study of this thesis where sample are placed in vacuum chamber, intrinsic damping dominates.

Intrinsic regime: In vacuum the dissipation mechanisms in nanomechanical structure are intrinsic-internal and intrinsic-external. Intrinsic-internal mechanisms include effects such as phonon-phonon scattering (acoustic phonons), phonon-electron scattering and thermoelastic damping (acoustic-thermal phonon scattering) [58, 90-92]. Support dissipation and surface losses are regarded as intrinsic-external mechanisms. The overall quality factor Q_{total} can be written as a summation of contributions according to

$$Q_{total}^{-1} = \sum Q_i^{-1} \tag{2.2.42}$$

where Q_i refers to the contribution of a given mechanism. Thermoelastic damping stems from a heat flow over the thickness of the cantilever between opposite areas, which are alternatively under compressed and tensile stress during resonance [93]. Loss due to clamping occurs because of the strain induced at the connection to the support structure and motional energy leakage to the base region.

Molecular regime: In the molecular regime collisions between the nano-beam and the surrounding gas molecules have to be taken into account. If the gas pressure is small, the Knudsen number K_n is high. This number is the ratio between the mean free path of the gas molecules and the beam size. At pressures so low that $K_n \gg 10$ the mechanical Q factor is dominated by the intrinsic losses discussed above. With increasing pressure, the molecular regime starts at about $K_n \sim 10$ [94]. Momentum exchange between individual gas molecules and the mechanical structure at a rate proportional to the difference in velocity between the molecules and the resonator is here considered to be the damping source.

Viscous regime: When $K_n < 0.01$, gas molecules can no longer be considered as free molecules and collisions between the molecules have to be taken into account. In this regime the gas behaves like a viscous incompressible fluid [95].

2.4 Parametric oscillation

A parametric oscillator is a harmonic oscillator in which oscillations are driven by periodically varying a parameter (such as the mass or spring constant) of the system at a frequency typically different from the natural frequency of the oscillator. In Chapter 6, I present experimental observations of parametric control over picometric thermomechanical vibration in a nano-

optomechanical system. The underlying dynamics of those observations can be described by the Brownian parametric oscillator equation [96]:

$$\ddot{x}(t) + \gamma_m \dot{x}(t) + \left[\omega_m^2 + 2\varepsilon\omega_m \cos(\omega_p t)\right] x(t) = F_{thermal}(t)/m_{eff} \tag{2.2.43}$$

where $x(t)$ is the real time thermal vibration of a nanomechanical resonator at angular frequency ω_m with effective mass of m_{eff} driven by thermal Langevin force $F_{thermal}(t)$, γ_m is the mechanical dissipation factor and ω_p is the parametric pumping angular frequency. This oscillator has a time varying spring constant $k(t) = m_{eff}\left[\omega_m^2 + 2\varepsilon\omega_m \cos(\omega_p t)\right]$, where ε is the parametric pumping strength proportional to the frequency shift ($\delta\omega = \sqrt{\omega_m^2 + 2\varepsilon\omega_m} - \omega_m \sim \varepsilon$). The parametric pump with angular frequency of ω_p converts the initial thermomechanical vibration without parametric driving at frequency ω_m into multiple thermal vibration Stokes' or anti-Stokes' sidebands centered at angular frequencies $\omega = \omega_m \pm N\omega_p$ via frequency mixing with N being an integer.

At low parametric pumping strength and in a stable regime, the sidebands' weight depends on the ratio between parametric pumping strength ε and its frequency ω_p, and the parametrically driven thermomechanical displacement power spectral density spectrum can be represented as:

$$\Gamma(\omega) = \sum_{-\infty}^{\infty} J_N^2(\varepsilon/\omega_p)\Gamma_0(\omega_m + N\omega_p) \tag{2.2.44}$$

with

$$\Gamma_0(\omega_m) = \frac{4\gamma_m k_B T}{m_{eff}[(\omega_m^2 - \omega^2)^2 + \gamma_m^2\omega^2]} \tag{2.2.45}$$

being the initial thermomechanical displacement power spectral density (PSD) without parametric pumping. J_N represents the Nth order Bessel function of the first kind.

Figure 2.6 shows the numerically calculated thermomechanical displacement PSD results obtained by numerically solving the Eqn. (2.4.43) for one of the experimentally measured nano-optomechanical oscillators as presented in Chapter 6. It has the effective mass m_{eff} = 2.2 pg, mechanical angular frequency ω_{m1} = 2π×2328.3 kHz ($\gamma_{m1} = 2\pi\delta f_1$= 2π×1.21 kHz, Q_1 = 1926.8). The blue line in Figure 2.6a shows the numerically calculated thermomechanical displacement PSD assuming the parametric pumping strength ε= 9.87 kHz, ω_p = 2π×20 kHz, one can see the initial thermomechanical displacement PSD (orange curve) is converted into multiple thermal vibration Stokes' or anti-Stokes' sidebands centered at angular frequencies $\omega = \omega_m \pm N\omega_p$ (blue curve). A good match between the numerical and analytical model is found in Figure 2.6a-c when the parametric pumping strength is relatively small. However, as can be seen in Figure 2.6d, deviation

is found particularly on the low-frequency Stokes' sidebands when the parametric pumping strength is strong enough. The experimentally measured maximum parametric pumping strength is $\varepsilon/2\pi$ ~ 10 kHz range as will be shown in section 6.4. Therefore, the analytical result in Eqn. (2.4.43) can be used to analyze the experimental data.

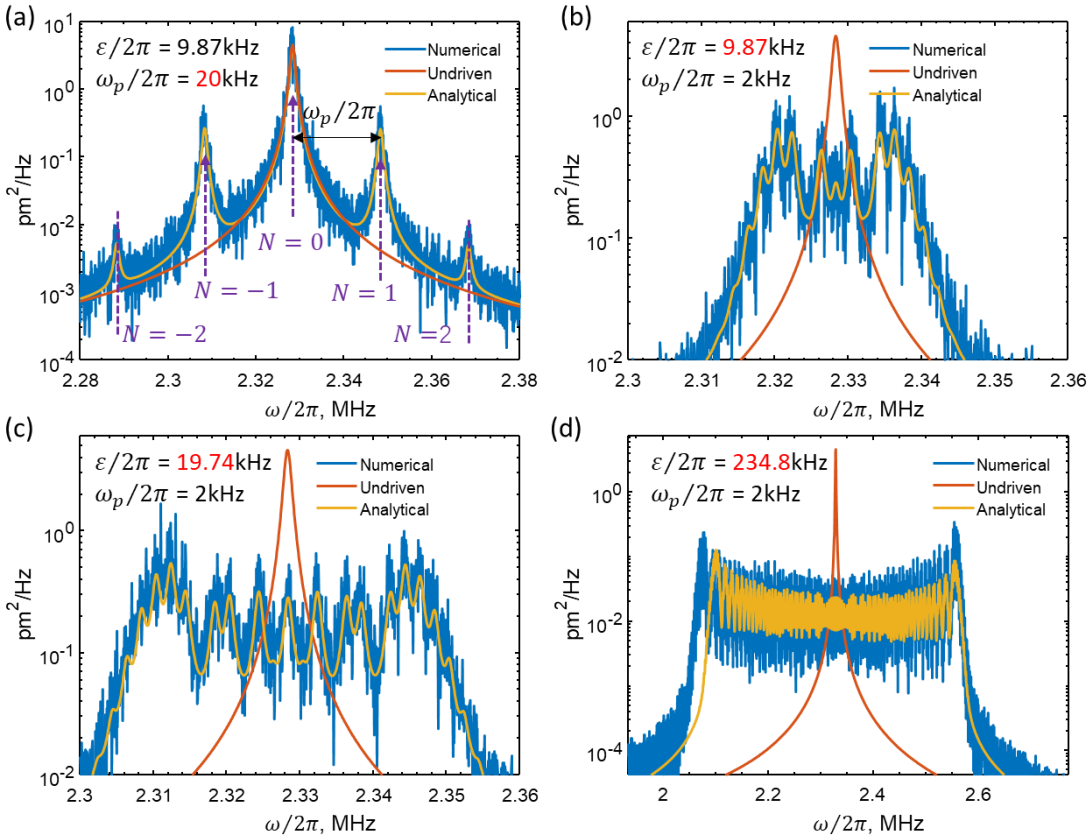

Figure 2.6 **Numerically calculated displacement power spectral density for a Brownian parametric oscillator.**Orange line shows the thermomechanical displacement power spectral density for a Brownian oscillator without parametric pumping term. Blue line and yellow lines respectively show the numerically calculated and the analytically approximated Eqn. (2.4.44) thermomechanical displacement power spectral density. (a)(b) Calculated spectra evolution for two oscillators with different parametric pumping frequency ω_p =2π×20 kHz and 2π×2 kHz while having same pumping strength ε=2π×9.87 kHz. (b)-(d) Calculated spectra evolution for the oscillators with different parametric pumping strength ε while having same pumping frequency ω_p=2π×2 kHz.

2.5 Summary

In this chapter, the development of a physical description of Brownian or thermal motion has been introduced starting from Einstein's pure diffusion model, Markovian Langevin model to non-Markovian Langevin model when considering hydrodynamic interaction. These theories can be in principle applied to a nanomechanical structure that is situated in different environments.

Thermal motion of a nanomechanical structure in a particular mechanical mode has been described using Langevin model by including a restoring force term. Thermomechanical displacement power spectral density that is widely used in experimental measurements in sections 3.4, 4.1, 6.3 and 6.4

has been derived from this model. Ballistic thermal motion characteristics of a nanomechanical structure at short timescale are also mathematically derived and numerical modelling is performed, which supports understanding and interpretation of the experimental results in section 4.1.

In the Langevin model, the parameters of mechanical eigenfrequency and effective mass for a nanomechanical beam with regular shape can be derived from Euler-Bernoulli beam theory. Additionally, the effect of tensile stress on the eigenfrequency of a nanomechanical beam is examined, this supports the explanation of the variation of mechanical resonant frequencies observed in an array of geometrically identical nanomechanical oscillators (sections 3.4.3 and 6.3). This also provides the theoretical foundation for the parametric control of the thermomechanical vibration of nanomechanical oscillator arrays via dynamic photothermal tuning mechanism as demonstrated in section 6.4. The mode-dependent effective mass has been derived which can assist in determining displacement sensitivity of a technique as will be experimentally demonstrated in sections 3.4.3 and 6.3. Considering a 20 μm long, 100 nm thick and 200 nm wide Si_3N_4 doubly-clamped nanomechanical beam having picogram-scale effective mass, they are expected to oscillate in the thickness direction at their fundamental mode around 2 MHz by a root-mean-square thermal motion amplitude of 100 picometres which is atomic length scale at room temperature.

A Brownian parametric oscillator model and its numerical calculation are also introduced which helps analyze and interpret the experimental observations of parametric control over a Brownian oscillator as presented in section 6.4.

Overall, these models underpin the theoretical part of this thesis and are used to analyse the experimental data throughout the following chapters.

Chapter 3 Sub-atomic movement visualization in nanostructures via free electron edge-scattering

The existing nano-imaging techniques such as transmission and scanning electron microscopes, scanning probe techniques (STM, AFM, etc.) and optical super-resolution microscopies (PALM, STED, STORM, etc.) [97-100], and recently introduced methodologies employing superoscillatory and topologically structured light fields [101-103] provide nanometric spatial resolution in 'static' imaging. However, the acquisition frame rate of the instruments limits the application in imaging of MHz to GHz frequency motion. Time-resolved or ultrafast electron microscopes [14] are highly-specialized instruments employing short-pulse (typically fs laser-driven) electron sources and streak camera or time-correlated photon counting detectors to interrogate stimulated, short-timescale (e.g. carrier, lattice and bonding) dynamics in materials in pump-probe and stroboscopic regimes, which is capable of studying complex transient events on the nanoscale temporal and spatial resolution while generally containing very complex optics and timing control systems. Laser-based interferometric and cavity spectroscopic techniques [49, 50] can provide MHz frequency picometric sensitivity to changes in optical path length (i.e. in the direction of light propagation) but, for imaging purposes in the transverse direction, they are diffraction-limited with a spatial resolution of a few hundred nanometres at best.

In this chapter, I introduce a technique for hyperspectral motion visualization (HMV), which combines sensitivity to the movement of sub-atomic amplitude with the nanometric spatial resolution of secondary electron signal in conventional scanning electron microscopy (SEM). Quantitative, directionally-resolved measurements and mapping of displacement amplitude and relative phase, provides for highly localized interrogation of mechanical resonance characteristics (eigenfrequencies, quality factors) of target structures and visualization of their mechanical modes.

Section 3.1 describes the basics of electron-beam specimen interaction producing the various signals and their energy distributions and the interaction volume. Section 3.2 illustrates the concept and working principle of the developed hyperspectral motion visualization (HMV) SEM techniques followed by the instrumentation details in 3.3. The applications of this technique for thermal movement characterisation and driven motion mapping are demonstrated in section 3.4. Lastly, the secondary electron shot-noise limited displacement sensitivity and sample perturbation by the electron beam is analysed in section 3.5.

3.1 Electron-beam specimen interaction

Electrons interact elastically or inelastically with atoms at various depths within the specimen, producing various types of signals that contain information about the surface topography and composition of the sample, including secondary electrons (SE), back-scattered electrons (BSE), characteristic X-rays and visible/near-infrared light (cathodoluminescence, CL), absorbed current (specimen current), elastically or inelastically scattered and transmitted electrons [104] (Figure 3.1).

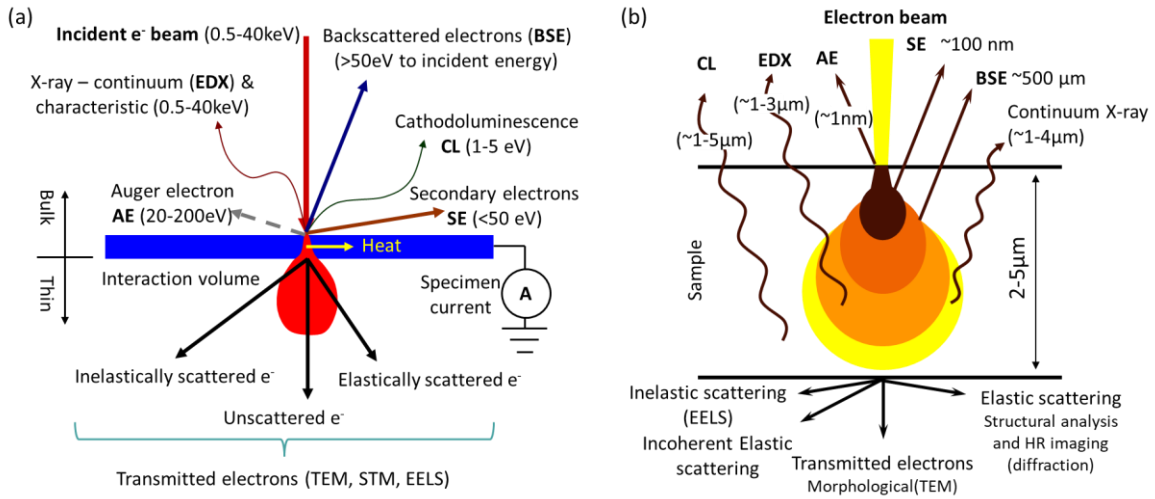

Figure 3.1 **Electron-beam specimen interaction.** (a) Various signals and their energy distributions. (b) Signals emitted from different parts of the interaction volume. Images are adapted from ref. [104].

In the secondary electron imaging (SEI) used in this work, the secondary electrons are emitted from the specimen surface. Consequently, SEI can produce very high-resolution images of a sample surface, revealing details less than 1 nm in size. Another commonly available mode of imaging is based upon back-scattered electrons (BSE), which are electrons reflected from the sample by elastic scattering. They emerge from deeper locations within the specimen and, consequently, the resolution of BSE images is less than SE images. However, BSE is often used in analytical SEM, along with the X-ray spectra, where the intensity of the BSE signal is strongly related to the atomic number (Z) of the specimen. BSE images can provide relative atomic number contrast linked to the elemental distribution in the sample. In samples predominantly composed of light elements, such as biological specimens, BSE imaging can image colloidal gold immuno-labels of 5 or 10 nm diameter, which would otherwise be difficult or impossible to detect in secondary electron images. X-rays are emitted when the electron beam removes an inner shell electron from the sample, causing a higher-energy electron to fill the shell and release energy. The energy or wavelength of these X-rays can be measured by energy-dispersive X-ray spectroscopy or wavelength-dispersive X-ray spectroscopy and used to identify and measure the abundance of elements in the sample and map their distribution. Cathodoluminescence (CL) is the emission of low energy photons in the range from

approximately 1 eV to 5 eV (infrared, visible, and ultraviolet light) as a result of inelastic scattering of the high energy beam electrons, which can be used to characterise electronic state information.

3.2 Concept of hyperspectral motion visualization SEM

The functional principle behind the motion visualization technique is illustrated in Figure 3.2. Conventional secondary electron images are formed by raster scanning a focused electron beam over an object and detecting, at each point, the integrated secondary electron current. Any fast-moving components of the object (the wings and antennae of the bee in Figure 3.2a) will suffer 'motion-blur' because their displacement cannot be tracked on timescales shorter than the frame rate. However, by instead recording the time dependence of the secondary electron (SE) current at each point one can detect and spatially map fast movements of the object. One may then record either full raster-scanned images with SE detection locked at a chosen frequency, or construct a complete hyperspectral image by computing the Fourier spectrum of motion at each point. These 'images' will show spatially resolved, quantitative detail of displacement amplitude and phase at a chosen frequency or across a range of frequencies.

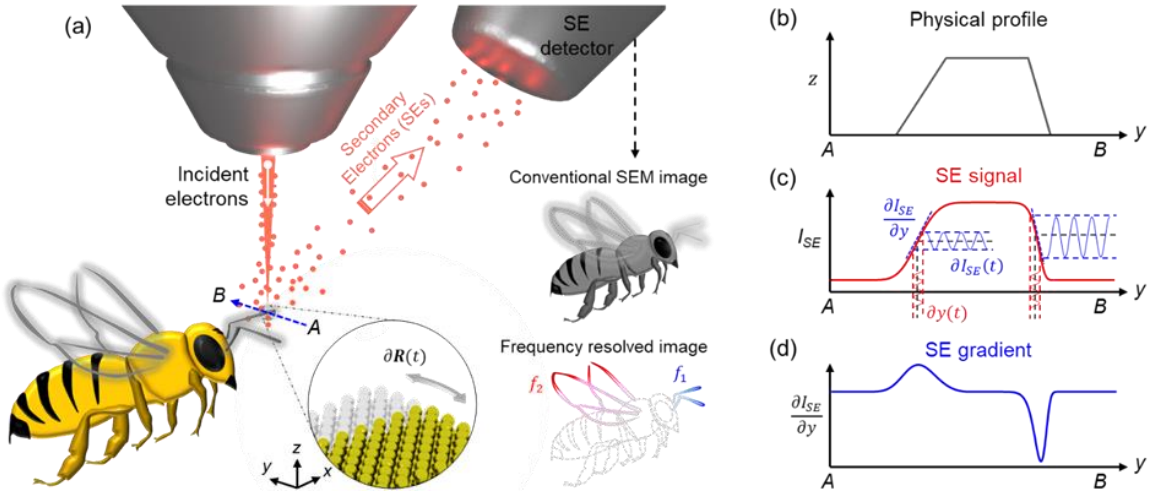

Figure 3.2 **Hyperspectral Motion Visualization (HMV-SEM) concept.** (a) Conventional (static) secondary electron (SE) images obtained in a scanning electron microscope are based upon the time-averaged SE signal at each point, whereby moving parts suffer 'motion blur'. HMV-SEM maps based upon the detection of selected frequency components in the SE signal will show only those parts which oscillate at that frequency, revealing the amplitude and direction of movement at each point. (b-d) An incident electron beam scanned over an object [notionally here, one of the bee's antennae, along the line AB in (a)] generates a scattered secondary electron signal with an amplitude profile (c) related to the physical profile of the object (b) and the spot size and intensity profile of the incident electron beam. Where the gradient (d) of this profile is non-zero, displacements of the object ∂y translate to changes in SE signal ∂I_{SE}, as illustrated inset to (c).

For simple objects, much useful information can be obtained from images recorded at just a few selected frequencies, as will be demonstrated in what follows. Figure 3.2 (b-d) details the mechanism by which the SE signal generated by an incident electron beam transduces displacement [105, 106], including at length scales far smaller than the beam diameter where movement induced

local variation of SE flux is still significant at structure's edges. While the target object (notionally one of the bee's antennae in Figure 3.2a) is stationary, the SE current $I_{SE}(\boldsymbol{r})$ generated as an incident electron beam is scanned along the line *AB* (where $\boldsymbol{r}$ is coordinate in the image plane) will change in magnitude from and return to zero on either side (where the incident beam entirely misses the object) at a rate dependent upon the sharpness of the physical edges and the intensity profile of the electron beam. At these edges, small time-dependent displacements $\partial\boldsymbol{R}(t)$ of the object will translate to changes in the SE signal:

$$\frac{\partial I_{SE}(\boldsymbol{r},\boldsymbol{R}(t))}{\partial t} = \frac{\partial I_{SE}(\boldsymbol{r},\boldsymbol{R}(t))}{\partial \boldsymbol{R}} \cdot \frac{\partial \boldsymbol{R}}{\partial t} = -\nabla I_{SE}(\boldsymbol{r}) \cdot \boldsymbol{v}(t) \tag{3.2.1}$$

where $\boldsymbol{v}$ is the object's movement velocity vector at the measurement point. Integrated over time:

$$I_{SE}(\boldsymbol{r},t) = -\nabla I_{SE}(\boldsymbol{r}) \cdot \boldsymbol{R}(t) + C \tag{3.2.2}$$

Thus, at each point on the oscillating target, the magnitude of the time-dependent SE signal will be equal to the scalar product of two vectors: the gradient of the static SEM image parallel to the motion direction at that point $\nabla I_{SE}(\boldsymbol{r})$ and the displacement $\boldsymbol{R}(t)$. As such, motion in any direction with a non-zero projection to the image plane can be detected at any point where the corresponding SE gradient is non-zero. In the Figure 3.2 schematic, for example, if the image plane is inclined at an angle θ_i to the *y* axis, both horizontal $\partial y(t)$ and vertical $\partial z(t)$ displacements of the object (in and out of the xy sample plane) can be detected on the basis of a SE signal gradient parallel to y. The noise equivalent displacement (NED) level in such measurements – the magnitude of displacement detectable with unitary signal-to-noise ratio with an integration time of one second – is determined largely by the Poisson statistics of electrons incident on the SE detector (see section 3.5.1). It is inversely proportional to the SE current gradient ∇I_{SE}. As estimated in section 3.5.1, for a typical SEM, this minimum detectable displacement can be as small as ~1 pm even while the incident beam diameter (i.e., static imaging resolution) is ≥ 1 nm. The ability to detect motion at this scale presents remarkable opportunities for imaging the movement of nanostructures, bearing in mind that by comparison the lattice constants of solids are typically in the 300-700 pm range and the radii of isolated neutral atoms lie between 30 and 300 pm.

3.3 Instrumentation for hyperspectral motion visualization SEM

A hyperspectral motion visualization SEM consists of two main parts: a conventional scanning electron microscope (SEM) with external scanning control, and lock-in detection and data acquisition modules, see Figure 3.3.

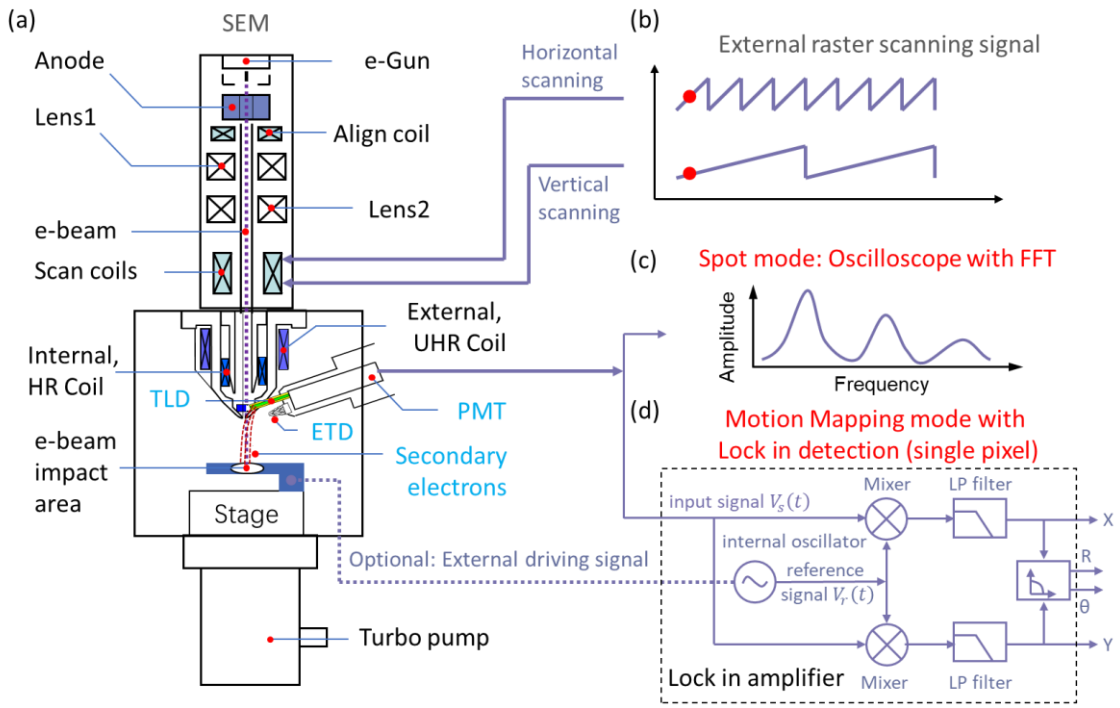

Figure 3.3 **Hyperspectral Motion Visualization (HMV-SEM) instrumentation.** (a) A SEM consisting of electron optics, sample positioning, signal detection and a vacuum system. (b) The electron beam is externally controlled through deflect lens or scan coil by a dual-channel arbitrary function generator generating sawtooth-like waves for raster scanning. (c) For Brownian motion detection, the instrument is configured as a spectrum analyser (oscilloscope with FFT function) and SEM is operating in the spot mode. (d) For motion imaging mode, the lock-in is then referenced to the clock frequency to demodulate the output signal of the secondary electron detector pixel by pixel and build amplitude and phase maps of the object's movements at the frequency of interest.

The hyperspectral motion visualization system was built around the scanning electron microscope arm of an FEI Helios NanoLab™ 600 DualBeam FIB/SEM system. The secondary electron detector used in this work is a built-in through-the-lens detector (TLD) allowing ultra-high-resolution imaging (UHR) mode. Acquisition and processing of the signal from the secondary electron detector are performed using a Zurich Instruments UHFLI digital lock-in amplifier, which has the oscilloscope with FFT function and multi-Frequency option. For Brownian motion detection, the instrument is configured as a spectrum analyser (oscilloscope with FFT function) and the SEM is operated in spot mode. In the hyperspectral motion imaging regime, scanning of the electron beam is controlled by a dual-channel arbitrary function generator (Tti TGF4242) generating sawtooth-like waves for horizontal and vertical scanning while the lock-in amplifier's internal clock generator is optionally used to drive a piezoelectric sample stage actuator (Thorlabs PA4FEH3W). The lock-in is then referenced to that clock frequency to demodulate the output signal of the secondary electron detector and build amplitude and phase maps of the object's movements at said frequency. The DC component of the signal is simultaneously employed to build the conventional SEM image of the sample using the multi-Frequency option. The raster scanning speed can be adjusted depending on the sampling rate and integration time of lock-in detection.

3.4 Applications of hyperspectral motion visualization SEM

To elucidate and quantitatively validate the performance of the HMV-SEM technique we employ rectangular cantilevers, i.e., the common actors and structural components of many nanomechanical devices and systems – objects with well-understood, analytically described modes of oscillation.

3.4.1 Thermal motion characterization

As introduced previously, the random thermal motion of small objects at non-zero temperatures is perhaps most familiar in the microscopic random walk of free particles in liquids, known as Brownian motion. But the thermal motion of picometric amplitude is also present in anchored micro-/nano nano-objects, such as cantilevers and doubly-clamped beams, and is most profound at their natural mechanical resonant frequencies. Such motion provides an ideal calibration reference for the sensitivity of the HMV-SEM technique as its amplitude is thermodynamically related to the physical parameters of the object: which is to say that a direct quantitative comparison can be made between experiment and energy equipartition theorem [30, 85].

To demonstrate, we detect the thermal motion of a 22 µm long cantilever (Figure 3.4a) manufactured by focused ion beam milling from a 50 nm thick silicon nitride membrane (a flexible substrate) coated by thermal evaporation with 50 nm of gold (for strong secondary electron signal contrast). With the incident electron beam fixed at a point on one of the cantilever's long edges near the tip, as indicated in Figure 3.4a, we record the time dependence of the secondary electron signal in the frequency domain and calculate the corresponding amplitude spectral density (ASD, Figure 3.4c). In all measurements reported here an incident electron energy of 5 keV and a beam current of 86 pA is employed, whereby the effects of electron beam-induced heating and momentum transfer to the cantilever are negligible (see section 3.5.2). The measured secondary electron signal ASD at a given point is directly related to cantilever displacement ASD (right-hand axis in Figure 3.4c) via the SE signal gradient (Figure 3.4b) at that point, with account taken for the oblique incidence of the electron beam. One can observe peaks in the frequency spectrum at three of the cantilever's natural oscillation frequencies: specifically, the fundamental out-of-plane mode at 117.6 kHz, fundamental in-plane mode at 528.0 kHz and second-order out-of-plane mode at 739.0 kHz (attribution of modes being confirmed by computational modelling). Cantilever mechanical properties are simulated using the solid mechanics module in COMSOL Multiphysics (finite element method). A rectangular 100 nm thick (50 nm each of silicon nitride and gold) × 500 nm wide cross-section is assumed. From this model, the three lowest Eigenfrequencies of a 22 µm long cantilever are those of the fundamental out-of-plane flexural mode at 111 kHz; fundamental

in-plane flexural mode at 518 kHz; and the 2nd-order out-of-plane flexural mode at 695 kHz. These correlate well with measured resonance frequencies (Figure 3.4c) – small discrepancies being accounted for by manufacturing imperfections and internal stresses within/between the silicon nitride and gold layers (which also account for the slightly out-of-plane equilibrium position of the cantilever).

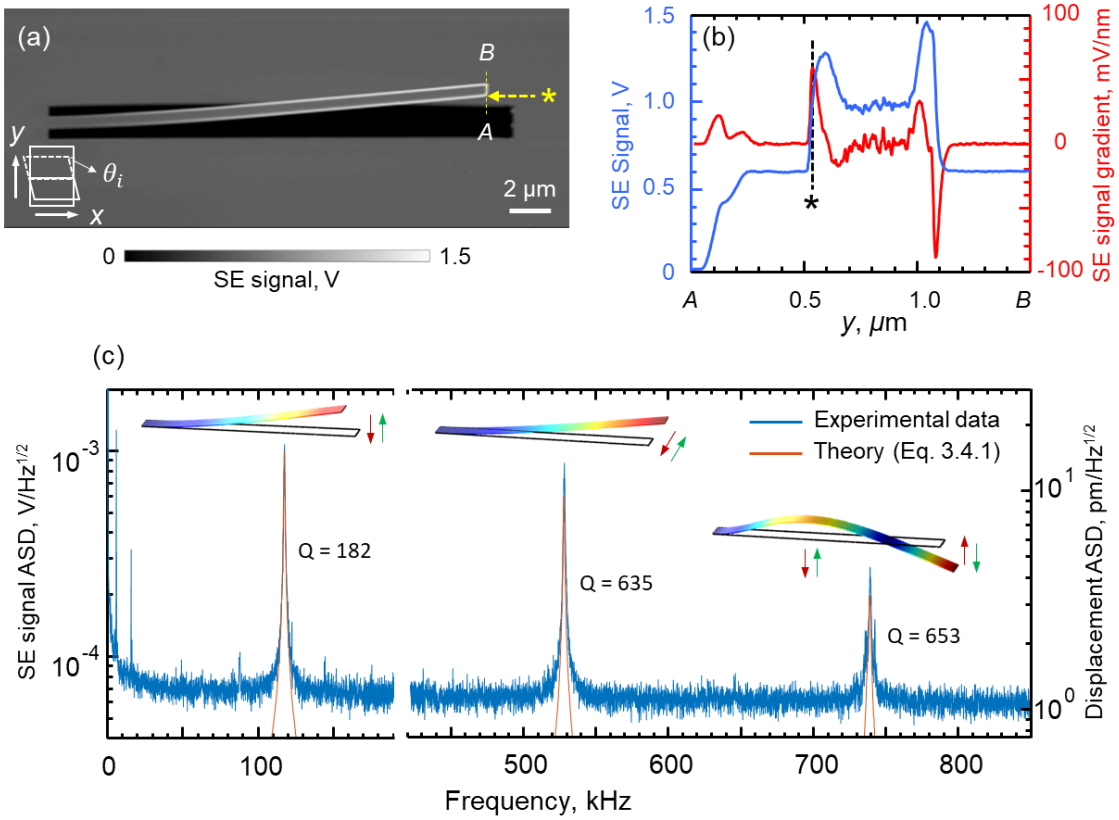

Figure 3.4 **Sensing thermal motion of a cantilever.** (a) Static secondary electron image of a gold-coated silicon nitride cantilever [100 nm thick, 500 nm wide, 22 μm long], viewed at an oblique angle θ_i = 15° to the membrane plane. (b) Profile along the line AB of secondary electron DC signal and the gradient thereof. (c) Amplitude spectral density (ASD) of secondary electron signal measured at the point *, showing peaks associated with out-of- and in-plane oscillatory modes [as denoted by the inset schematics]. The right-hand axis shows a calibrated scale of displacement ASD. Overlaid red lines are analytical displacement ASD curves given by Eq. (3.3), using experimentally measured values of f_m and Q for each mode, and assuming $m_{eff} = 0.25m$.

According to the Wiener–Khinchin theorem [30, 85], the thermomechanical displacement power spectral density (PSD = ASD^2) of an oscillator is

$$S(f) = \frac{k_B T f_m}{2\pi^3 m_{eff} Q[(f_m^2 - f^2)^2 + (f f_m/Q)^2]} \tag{3.4.1}$$

where k_B is the Boltzmann constant, T is temperature and, for each mode, m_{eff}, f_m and Q are respectively the effective mass, natural frequency and quality factor. From experiment – the mapping of Eq. (3.4.1) onto the peaks in Figure 3.4c using measured values of f_m and Q at room

temperature (T = 300 K), with m_{eff} determined by best fit – root mean square (RMS) thermal motion amplitudes $\sqrt{\langle x^2 \rangle}$ can be evaluated as the square root of an integral of PSD over frequency:

$$\sqrt{\langle x^2 \rangle} = \sqrt{\int_0^\infty S(f)df} \tag{3.4.2}$$

These calculations yield amplitudes of 1.60 nm for the out-of-plane mode at 117.6 kHz; 0.53 nm for the in-plane mode at 528.0 kHz; and 0.27 nm for the second-order out-of-plane mode at 739.0 kHz. These compare very well with analytical values of 1.57, 0.35 and 0.25 nm respectively, from thermal equipartition for an ideal rectangular cantilever, whereby $\sqrt{\langle x^2 \rangle} = \sqrt{k_B T / m_{eff}(2\pi f_m)^2}$ and m_{eff} has a fixed value of $0.25m$ for all modes (m being the real mass). The accuracy of the correlation between theory and experiment is illustrated in Figure 3.4c by the overlaid analytical curves, which are calculated according to Eq. (3.4.1) with $m_{eff} = 0.25m$. Likewise, the ~1 pm/Hz$^{1/2}$ background signal level seen in Figure 3.4c corresponds very well with the expected noise equivalent displacement floor (see section 3.5).

Full-width half-maximum peak widths Δf are a measure of oscillator damping: $\Delta f = \gamma_s / (2\pi m_{eff})$, where γ_s is the (material, ambient pressure, and mode-dependent) Stokes friction coefficient[107, 108]. With the effective mass of a cantilever being, again, not mode-dependent, the peak width Δf is straightforwardly proportional to, and resonance quality $Q = f_m / \Delta f$ inversely proportional to γ_s.

3.4.2 Hyperspectral driven motion mapping

The HMV-SEM technique can also be applied to map externally-driven movements of nanostructures. By raster scanning the injection point over a target and synchronously detecting the SE signal at the driving frequency (using a lock-in amplifier), a spatially resolved map of driven oscillation amplitude and phase can be constructed, giving a comprehensive picture of the sample's mechanical response at the selected frequency. By then changing the driving frequency and repeating the raster scan, a hyperspectral image of sample movements can be assembled. We demonstrate this modality by visualizing the oscillatory motion of cantilevers driven by a piezoelectric transducer (with an oscillatory amplitude of $\leq$1 nm). Figure 3.5a-c show images of the above (Figure 3.4) cantilever in terms of, respectively, the DC component (c.f. static SE image) and the amplitude and phase of the time-dependent component of the SE signal at 739.0 kHz – the frequency of its second-order out-of-plane bending mode. These illustrate how the technique reveals movement at the high SE contrast edges of a structure: no signal is detected where the SE gradient is zero (along the central area of the cantilever surface). In this case, each bright edge of the cantilever in Figure 3.5a appears as a pair of lines in Figure 3.5b with opposing phase relative to

the piezo actuator (Figure 3.5c), corresponding to closely-spaced points of positive and negative SE gradient encountered as the incident electron beam is scanned across the edge. Phase mapping records the relative phase of modulated secondary electron signal referring to the driving signal. It depends on both the local gradient and the motion mode shape of the studied structure according to Eqn. (3.2.2).

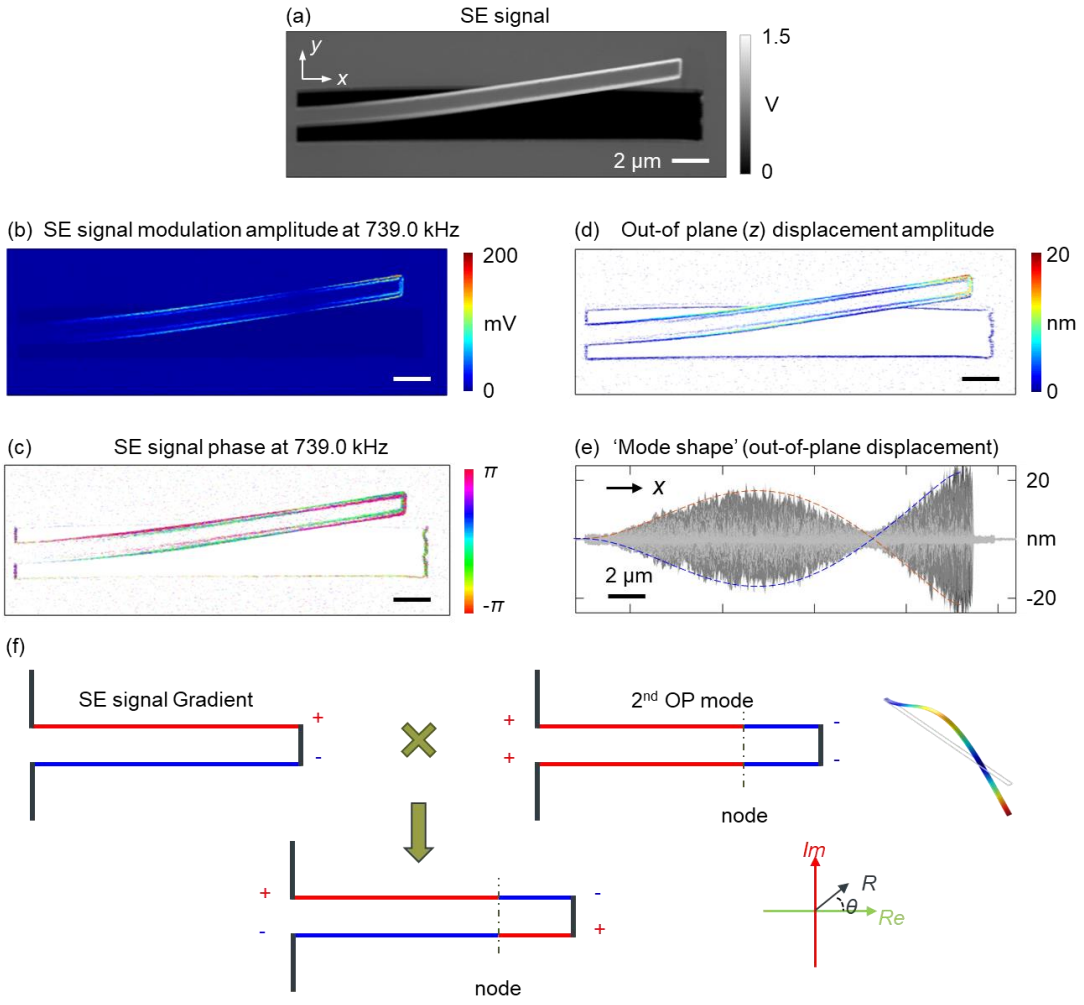

Figure 3.5 **Visualization of driven cantilever motion.** (a-c) DC component (a) and synchronously recorded amplitude and phase (b and c respectively) of the time-dependent component of the secondary electron signal recorded while the structure is mechanically driven at the cantilever's 739.0 kHz 2nd-order out-of-plane resonant frequency by a piezo-actuator. (d) Calibrated out-of-plane [z-direction] displacement amplitude maps of the cantilever. (e) x-z plane projection of absolute displacement with the corresponding numerically simulated mode profile overlaid as a pair of dashed lines. Note that the vertical image-plane scale [panels a-d] has been enlarged for clarity: the 2 μm scale bar applies only to the x direction. Also, for clarity in (d), no data is presented at points where the SE gradient falls below a noise threshold, i.e., such that displacement cannot be quantified. The same [white] pixels are then also excluded from (c). (f) 2nd order out-of-plane mode phase mapping of a cantilever. The final measured phase is a product of secondary electron gradient with the mode shape. Here, '-' and '+' are π out-of-phase.

As shown in Figure 3.5f, a second order out-of-plane mode cantilever is used to illustrate phase mapping. The secondary electron gradient depends on the scanning direction, which is positive on one edge and negative on the other edge. The cantilever's left clamped end part and its tip part (separated by the node line) moves out-of-phase in the case of second order out-of-plane

oscillation mode. Therefore, the measured electronic signal phase is the multiplication of SE signal gradient and mode shape. The '-' and '+' signs mean they are out-of-phase with a relative phase shift of π. An out-of-plane displacement amplitude map (Figure 3.5d) is obtained by dividing the time-dependent SE signal amplitude at each point of Figure 3.5b by the corresponding signal gradient derived from Figure 3.5a, taking account of the oblique viewing angle. Combining this with the signal phase and plotting all pixels as a histogram of absolute displacement against *x* coordinate, reveals the displacement mode shape, as shown in Figure 3.5e. In this example, the cantilever tip oscillates with an amplitude of ~25 nm. Currently, the minimum detectable displacement in motion mapping is about 0.1 nm (1 Angström) with an integration time of 0.1ms corresponding to the calibrated motion noise level.

To illustrate hyperspectral motion visualization, we employ a set of three cantilevers with different lengths (17, 22 and 27 µm) cut from a single membrane (Figure 3.6). Having first identified their individual natural frequencies from thermal motion spectra (as per Figure 3.5 above), we drive the structure and spatially map the movement of the whole sample at each frequency in turn (Figure 3.6a). The selective, resonant excitation of one cantilever at a time in either its fundamental or second-order out-of-plane bending modes is clearly observed, with the expected mode shapes being well defined in corresponding *x-z* projections of displacement (Figure 3.6b).

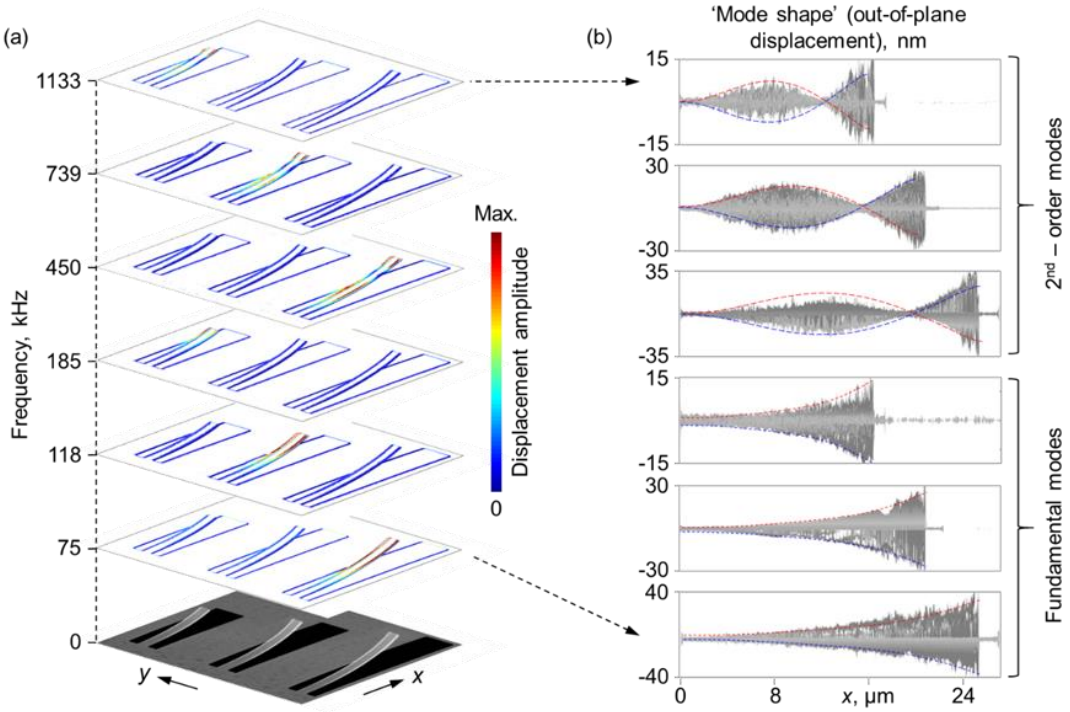

Figure 3.6 **Hyperspectral visualization of driven cantilever motion.** (a) Out-of-plane [z-direction] displacement amplitude maps of a set of three cantilevers of different length, shown in the zero-frequency [static secondary electron] image, recorded while the structure is mechanically driven at a selection of frequencies [as labelled] by a piezo-actuator. (b) Corresponding x-z plane projections of absolute displacement overlaid with numerically simulated mode profiles (dashed lines).

3.4.3 Visualization of movement in devices with multiple degrees of freedom

The examples presented above introduce the HMV-SEM technique by way of its use to study thermal and driven motion of isolated cantilevers. However, its full potential lies in application to more complex structures and devices with multiple degrees of freedom – 'nano-machines'. Here, we illustrate how the HMV-SEM technique can be used to interrogate thermal and driven motion, and thereby to better understand the functionality, of a nano-mechanical photonic metamaterial (Figure 3.7a-b) and a comb structure within a MEMS accelerometer (Figure 3.7c-f).

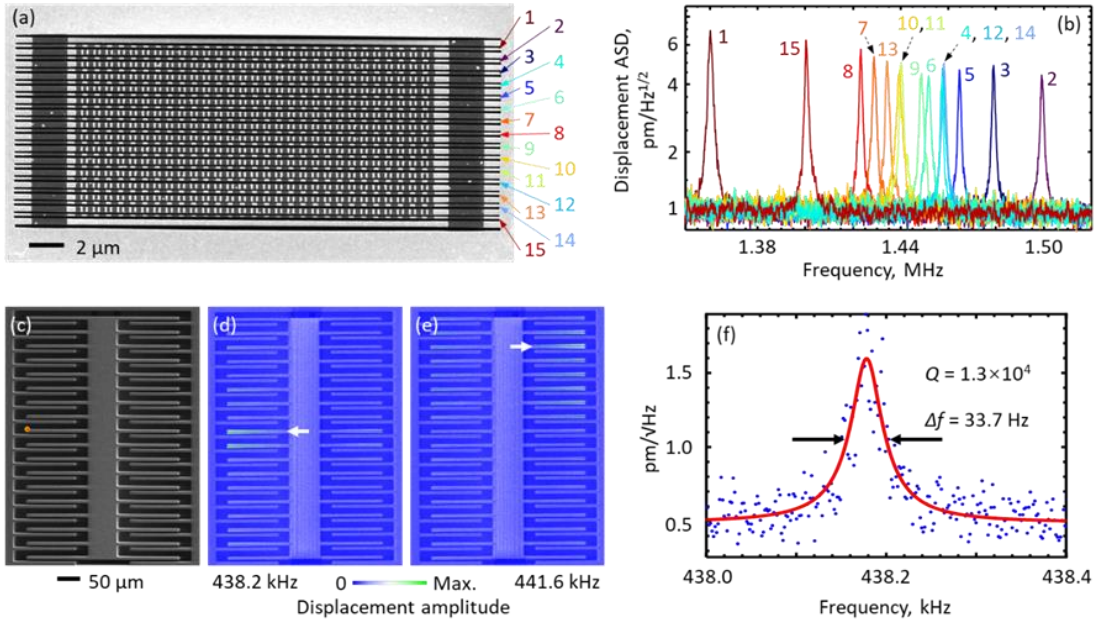

Figure 3.7 **Mapping thermal and driven motion in photonic metamaterials and MEMS devices.** (a) SEM image of an optomechanical metamaterial fabricated on a silicon-nitride nanomembrane (b) In-plane thermal motion displacement spectra measured at the centres of the fifteen narrow beams [as numbered in (a)]. (c) SEM image of a capacitive Si comb within a MEMS accelerometer. (d, e) Corresponding displacement amplitude maps for piezo actuator-driven in-plane motion at 438.2 and 441.6 kHz – the fundamental resonant frequencies of selected comb cantilever 'fingers' [marked by white arrows]. (f) Representative thermal motion spectrum measured at the tip of the comb cantilever finger marked with a red dot in (c).

Figure 3.7a shows an SEM image of a plasmonic nano-opto-mechanical metamaterial comprising an array of gold nano-brick trimers supported on alternately wide (325 nm) and narrow (165 nm) 28 µm long, 50 nm thick silicon nitride beams. This metamaterial has exceptionally large optical nonlinearity underpinned by the mutual displacement of neighboring beams, driven by interactions between dipole moments induced in the plasmonic nano-bricks by a control (pump) light beam [35]. The relative positions of the gold nano-bricks within the trimers determine the optical properties of the metamaterial as seen by a transmitted or reflected signal (probe) light beam at a different wavelength [35]. Ideally, a modulated pump beam will induce synchronous resonant (i.e., large amplitude) oscillation of one or other wide/narrow structural beams, thereby maximizing the effect of light-by-light control – the induced change in optical properties at the probe wavelength. As such, the nonlinear optical response of the metamaterial is dependent on the mechanical properties of

the structure, such as the natural frequencies and quality factors of the beams. All beams of the same type should preferably be mechanically identical to exclude inhomogeneous broadening of the nonlinearity. The diffraction limit precludes selective optical interrogation of the properties of individual structural beams, but the resolution of the electron beam-based motion visualization technique is perfectly suited to the task. The thermal motion spectra in Figure 3.7b reveal variations in the mechanical properties of a set of nominally identical beams: the fifteen narrow beams of the metamaterial shown have fundamental in-plane resonant frequencies of 1.44 MHz ±2%, mean square displacement amplitudes of 209 pm ±6% and quality factors of 1400 ±33%. While with the peripheral beams numbered 1, 2 and 15 excluded, these distributions narrow to ±1% in resonant frequency, ±4% in displacement amplitude and ±5% in Q. From static SEM imaging (Figure 3.7a), those three beams are subject to noticeable equilibrium out-of-plane deformation, but variations in mechanical properties among the majority cannot be anticipated – they are seen to have a high level of geometric uniformity, constrained only by the nanometric fabrication tolerances of the FIB milling technique. However, variations in their mechanical parameters are related not only to dimensional discrepancies or fabrication imperfections, but also to variations in tension (in the same way that tension determines the pitch of a violin string) derived from non-uniform stress intrinsic to the silicon nitride membrane substrate. The ability to quantify the mechanical response of the individual structural elements of a metamaterial provides valuable insight into device performance and provides for the possibility of in-situ correction during fabrication (i.e., within a dual-beam FIB/SEM system), thus enabling the fabrication of high-performance devices.

Figure 3.7c shows an SEM image of a silicon capacitive comb sensing element within a commercial MEMS accelerometer developed for automotive air-bag deployment systems. Acceleration in the sensing direction induces an inertial force on the mass attached to the movable part of the comb, resulting in a change in distance between the 'fingers' of the fixed and movable parts of the comb. From the associated change in capacitance, acceleration can be quantified. Device behaviours including sensitivity and false alarm response depend strongly upon the mechanical characteristics of the comb fingers, which are in effect micromechanical cantilevers, and controlled artificial displacements of the inertial mass may be applied to the detection of defective combs. Using the HMV-SEM technique (Figure 3.7d-f), we find that the nominally identical fingers of the present comb indeed have closely spaced fundamental resonant frequencies - varying by only ±0.4% about a mean value of 440 Hz, and resonance Q-factors of order 1.3×10^4 that vary by as much as ±8%. The fingers manifest in-plane thermal motion tip displacements of ~ 25 pm (as compared to a separation between adjacent fingers of ~ 5 μm).

The application of the motion detection technique to the spatial mapping of externally driven movements of flea setae is also illustrated in Figure 3.8. For this purpose, samples are mounted on

a piezoelectric actuator and the incident electron beam is raster-scanned over the sample, with the amplitude and phase of the secondary electron current oscillation detected at the piezo driving frequency by a lock-in amplifier. The point-by-point raster scanning, with an integration time of 20 µs at each pixel (and as above a 5 kV, 86 pA electron beam), is externally triggered for consistent registration of phase over the entire image area. Figure 3.8, referencing Robert Hooke's iconic 1665 optical microscopic image [109], shows stimulated nano-motion electron microscopic images of a (deceased) flea at a selection of different driving frequencies. The imaged maxillary palpus and coxa region include setae that are a few tens of micrometres long and a few hundred nanometres in diameter, which are here found to have natural oscillation frequencies in the sub-MHz range. The images (Figure 3.8b-d) reveal resonant oscillatory displacement amplitudes reaching a few hundred nanometres (in response to a piezo actuator in-plane drive amplitude of ~10 nm and against a background of the whole sample moving with said amplitude – dark blue features in the upper panels of Figure 3.8b-d). The lower panels in Figure 3.8b-d show the phase of the modulated secondary electron signal relative to the (piezo) driving force. This depends on both the local gradient and the motion mode shape of the structure: the absence of phase discontinuities along the long edges of resonantly oscillating setae show that they are moving in a fundamental flexural mode, i.e. that all points along the length are moving in the same direction at the same time.

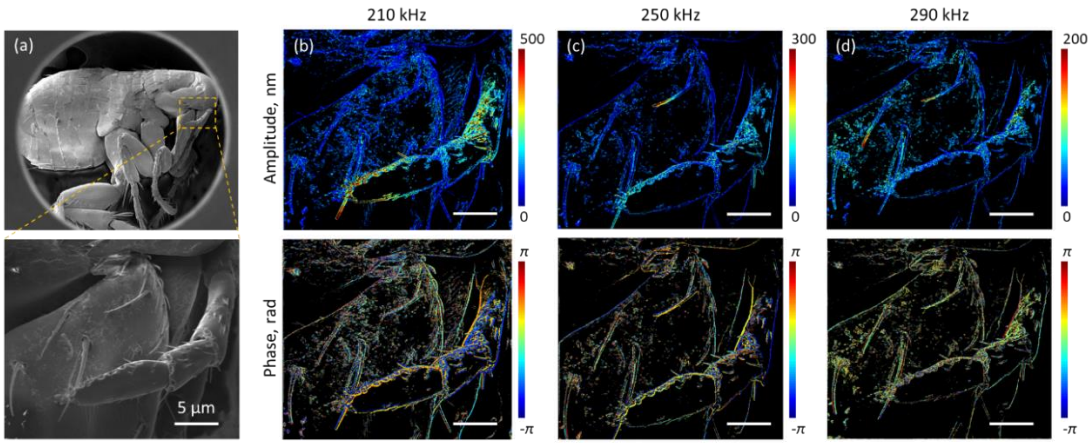

Figure 3.8 **Hyperspectral imaging of driven oscillations of flea setae.** (a) Static secondary electron image of the entire flea and enlarged detail of the motion-imaged area. (b, c, d) Amplitude (upper row) and corresponding phase (lower) of secondary electron signal modulation at selected driving frequencies [as labelled].

3.5 Fundamental measurement limit and sample perturbation by the electron beam

3.5.1 Noise Equivalent Displacement (NED)

The noise equivalent displacement (NED) level in HMV-SEM is determined largely by the Poisson statistics of electrons incident on the SE detector, whereby the standard deviation of shot noise is

$$\sqrt{N_e} = \sqrt{I_{SE}\tau/e} \tag{3.5.1}$$

N_e being the number of electrons detected in time interval τ.The SE current gradient can be estimated as

$$\nabla I_{SE}(\boldsymbol{r}) \sim \Delta I_{SE}/r_e \tag{3.5.2}$$

where ΔI_{SE} is the change in SE current over a distance equal to the incident electron beam spot size r_e~ 1nm. In measuring the amplitude of displacement d_{meas} by detecting secondary electron current variation, the number of electrons detected in time τ is then

$$S_e = d_{meas}(\Delta I_{SE}/r_e)\tau/e \tag{3.5.3}$$

A unitary signal-to-noise ratio (SNR) will be achieved when $S_e/\sqrt{N_e} = 1$, which is to say when

$$d_{meas} \sim r_e\sqrt{eI_{SE}/\left(\Delta {I_{SE}}^2 \tau\right)} \tag{3.5.4}$$

In practice (Figure 3.4b), we record SE detector output voltage $V_{SE} = \Omega I_{SE}$ and evaluate the corresponding gradient

$$\nabla V_{SE}(\boldsymbol{r}) \sim \Omega\Delta I_{SE}/r_e \tag{3.5.5}$$

in which terms the measurable displacement with unitary SNR is

$$d_{meas} \sim (r_e/\Delta V_{SE})\sqrt{e/\tau}\,\sqrt{V_{SE}}\sqrt{\Omega} \tag{3.5.6}$$

The constant of proportionality Ω is estimated at ~3×10^{10} Ohms, under an assumption that the full-scale 1.5V value of V_{SE} (Figure 3.4b) is associated with a maximum current I_{SE} of order 50 pA (from an incident beam current of 86 pA; a SE yield of 0.6, typical for gold at 5 keV [ref. [104]]; and SE collection efficiency approaching 100% for an SEM in a short working distance immersion lens configuration [110]). Thus, at the point marked by an asterisk in Figure 3.4b, where V_{SE} ~1V and $\Delta V_{SE}/r_e$ ~60 mV/nm, we may expect to measure a displacement as small as d_{meas} ~1.2 pm with a one second integration time. This also means that, in a second, S =1.47×10^4 (ΔI_{SE} = 2 pA) of electrons out of the totally generated N = 2.15×10^8 (I_{SE} = 34.4 pA) electrons contain the information of d_{meas} = 1.2 pm movement, which takes only 0.0068%. In the driven motion mapping examples of Figure 3.5 and Figure 3.6, where integration time is reduced to 0.1 ms, the expected NED level rises accordingly to ~120 pm/$Hz^{1/2}$.

3.5.2 Electron-to-cantilever momentum transfer

A non-relativistic electron of energy E_e has a velocity $v = \sqrt{\frac{2E_e}{m_e}}$ and momentum $p = m_e v$, where m_e is the electron mass. (v/c ~ 0.1 in the present case, so relativistic corrections can be ignored.) An electron beam of current I_e contains I_e/e electrons per second, where e is the electronic charge, and may thus impart a maximum force $F_{rad} = \frac{I_e}{e} p = \frac{I_e}{e}\sqrt{2E_e m_e}$. This amounts to ~2×10^{-14} N in the present case.

3.5.3 Electron-beam induced heating

For the purpose of estimating electron beam-induced temperature change, we consider:

- a free-standing bilayer beam of 50 nm gold on 50 nm silicon nitride, with length L = 22 µm and width w = 500 nm, in vacuum;
- an electron beam with acceleration voltage V = 5 kV and a beam current I_e = 86 pA incident on the gold side of the beam.

Monte Carlo modelling [111] shows that >99% of electrons are stopped within the 100 nm (gold plus silicon nitride) thickness of the beam at this low electron energy. In keeping with prior works [105] we assume that around 2.5% of incident electron beam power is absorbed as heat H_{abs} = 0.025$I_e V$ ~10 nW, predominantly in the gold layer.

The temperature change δT over the entire beam is related to the heat loss rate by Fourier's law $H_{abs} = -\kappa A_c \delta T/L$, where κ is thermal conductivity and $A_c = wh$ is cross-sectional area, h being thickness. The thermal conductivity of gold (300 W·m^{-1}·K^{-1}) is much larger than that of silicon nitride (2.5 W·m^{-1}·K^{-1}) so the presence of the nitride layer is ignored for the purposes of this estimate (whereby h = 50 nm), giving δT ~29 mK.

Finite element modelling (the heat transfer module in COMSOL Multiphysics) gives a very similar result. Herein we assume:

- the presence of both layers, with specific heat capacities at a constant pressure of 129 and 700 J·kg^{-1}·K^{-1} respectively for gold and silicon nitride;
- that the beam has an initial temperature T = 300 K and that one end (i.e., the anchored end of the cantilever) is attached to a thermostat at 300 K;

- a 10 nW point source of heat at one corner of the gold layer at the free end of the beam (i.e., the cantilever tip, as in the point measurement of Brownian motion presented in Figure 3.4).

Under these conditions, the temperature at the opposite gold corner of the cantilever tip increases by δT ~27 mK.

Root mean square thermal displacement is proportional to the square root of temperature, so the relative change resulting from a temperature change δT is given by $\sqrt{1 + \delta T/T} - 1$. At ~5×10^{-5} in the present case (i.e., not more than a few tens of femtometres against the measured ~1 nm thermal motion RMS cantilever tip displacements), this contribution is negligible.

3.6 Summary

In summary, in this chapter based upon the detection of the spectrally resolved secondary electrons current as a consequence of natural and/or stimulated oscillation of target nanostructures, I have developed a methodology and the instrumentation for quantitative, directionally-resolved measurements of high-frequency movements in the megahertz range with picometric (sub-atomic) amplitudes and the hyperspectral visualization of the movement with nanometric spatial resolution.

The hyperspectral movement visualization technique is deployed on a conventional scanning electron microscope to interrogate thermal (Brownian) and externally-driven motion at the pico- to the nanoscale in nanomechanical structure and nanomechanical photonic metamaterials. It is shown to provide for: highly localized measurement of an oscillator's resonant frequencies and quality factors; measurement of thermal motion amplitudes down to the electron shot noise-equivalent displacement level of 1 pm/Hz$^{1/2}$; and frequency- and directionally-resolved mapping of oscillatory motion 'mode shapes' with spatial (SEM imaging) resolution far beyond the diffraction limit applicable to optical vibrometry techniques.

This technique enables identification of variation in the mechanical resonance frequency of nanomechanical beams of the same geometry, due to the non-uniform stress inherent in the silicon nitride film substrate. The ability to quantify the mechanical response of the individual structural elements of a metamaterial provides valuable insight into device performance.

Chapter 4 Ballistic dynamics of flexural thermal movements in a nano-membrane

Flexural deformations and modes of oscillation are now understood to be of fundamental importance to the thermal, optical, electrical and mechanical properties of graphene and other 2D materials [112-116], and to the optical properties of photonic metamaterials through near-field coupling among resonators [6] and mechanochromic effects (i.e. mechanical deformation induced color change) [41]. In particular, atomic- to nano-scale flexural deformation in the geometry of elastic nano-membranes can deliver a wealth of optical modulation and tuning functionalities with electro-/magneto-/thermo-/acousto-optical and nonlinear response coefficients orders of magnitude larger than those found in natural media [6]. As objects decrease in size the thermal vibration of flexural components becomes increasingly important. For example, although thermal vibration of flexural components adds noise to induced controlled movements that underpin the functionality, these fluctuations provide an opportunity for the characterization of mechanical properties and sensing its surroundings [117].

In contrast with a classical Brownian particle in a fluid that is thermally perturbed by external collisions with ambient molecules, under vacuum thermal movements of the flexural components within nanomechanical photonic metamaterials are driven internally by momentum transfer from the annihilation and creation of the flexural phonons.

As long ago as 1906, Einstein realized that the commonly held picture of diffusive thermal motion, characterized by erratic, discontinuous changes in speed and direction, must break down at short time and length scales, where inertia becomes substantial [65] – objects must move ballistically between ‘collision’ events. He concluded that this regime of motion would be impossible to observe as to do so would require, at the time, unimaginably high spatial and temporal measurement resolution. Indeed, even today, it is a challenging proposition: while such measurements have been reported in recent years for optically-trapped microparticles undergoing Brownian motion in gas [118] and liquid [72], the phonon-dominated dynamics of free-standing films, nano-membranes, nano-wires and cantilevers remained underexplored because there were no routinely available technologies for quantifying their short-timescale nano/picoscale motion.

This chapter shows detection of variations in secondary electron emission from the edge of a moving (oscillating) nano-membrane interrogated with a focused electron beam provides for measurements of the membrane’s position with microsecond temporal resolution and sub-atomic displacement sensitivity as developed in Chapter 3. The microsecond temporal resolution is a new

dimension in this chapter, i.e. making it possible to access the short timescale ballistic regime. The detection method reveals the Einstein-predicted ballistic regime of thermal flexural motion of the membrane in short time scales. The reported experiments allow the measurement of velocities of consecutive steps of membrane movement and their statistics and provide direct experimental verification of the applicability of the equipartition theorem and Maxwell-Boltzmann statistics to flexural dynamics.

Theoretical work of this chapter is given in section 2.2 by solving the Langevin equation to better illustrate the behavior of ballistic regime thermal movement which supports understanding and interpretation of the experimental results in section 4.1. Experimental method of detecting ballistic thermal motion regime is described in section 4.2 followed by the analysis of sample disturbance using this method in section 4.3.

4.1 Experimental results and discussion on ballistic motion detection

The dynamics of thermal motion in the out-of-plane flexural mode of a cantilever cut from a free-standing gold nano-membrane was investigated here. The material and geometry were selected to facilitate observation of the ballistic regime by consideration of the cantilever's effective mass, the natural frequency and quality factor of its fundamental flexural mode, and the secondary electron yield. It was 30 nm thick and 62 µm long with a width tapered from 0.6 µm at the fixed end to 3 µm at the other, and an effective mass m_{eff} = 47 pg (Figure 4.1).

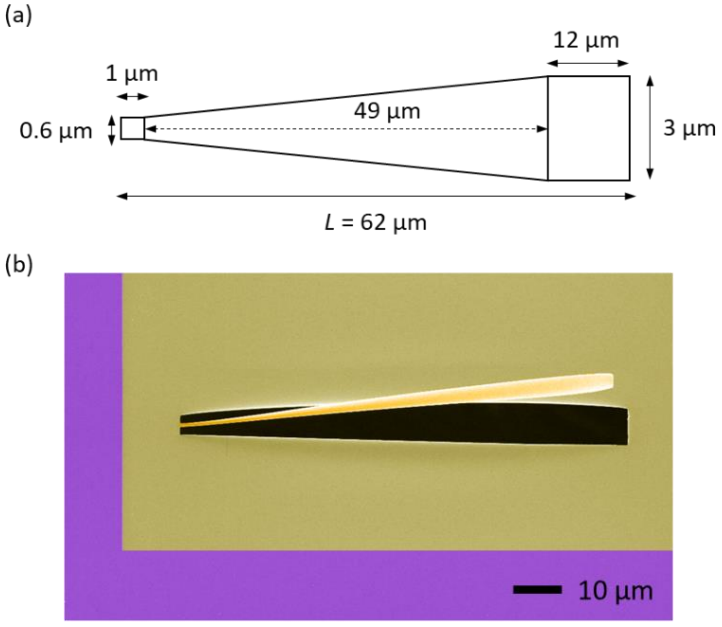

Figure 4.1 **Nanomechanical micro-cantilever.** (a) In-plane dimensional schematic of the cantilever. (b) False colour scanning electron microscope image of the cantilever, taken at a 30° viewing to the free-standing gold membrane surface normal along vertical direction. (Purple: Si frame, Yellow: gold membrane)

The secondary electron flux generated by scattering of an electron beam tightly focused on the edge of the membrane is highly sensitive to its position (see section 4.2 experimental method part). Position measurements as a function of time reveal Gaussian distributions of the membrane's position and velocity with root-mean-square values of $\sqrt{\langle x^2 \rangle}$= 8.3 nm and $\sqrt{\langle v^2 \rangle}$= 0.30 mm/s, respectively (Figure 4.2). The natural oscillation frequency of the cantilever $\omega_m/2\pi$ = 5.7 kHz and the damping time $\tau_b = 1/\gamma_m$ = 14 ms were evaluated from the Fourier spectrum of the displacement autocorrelation function.

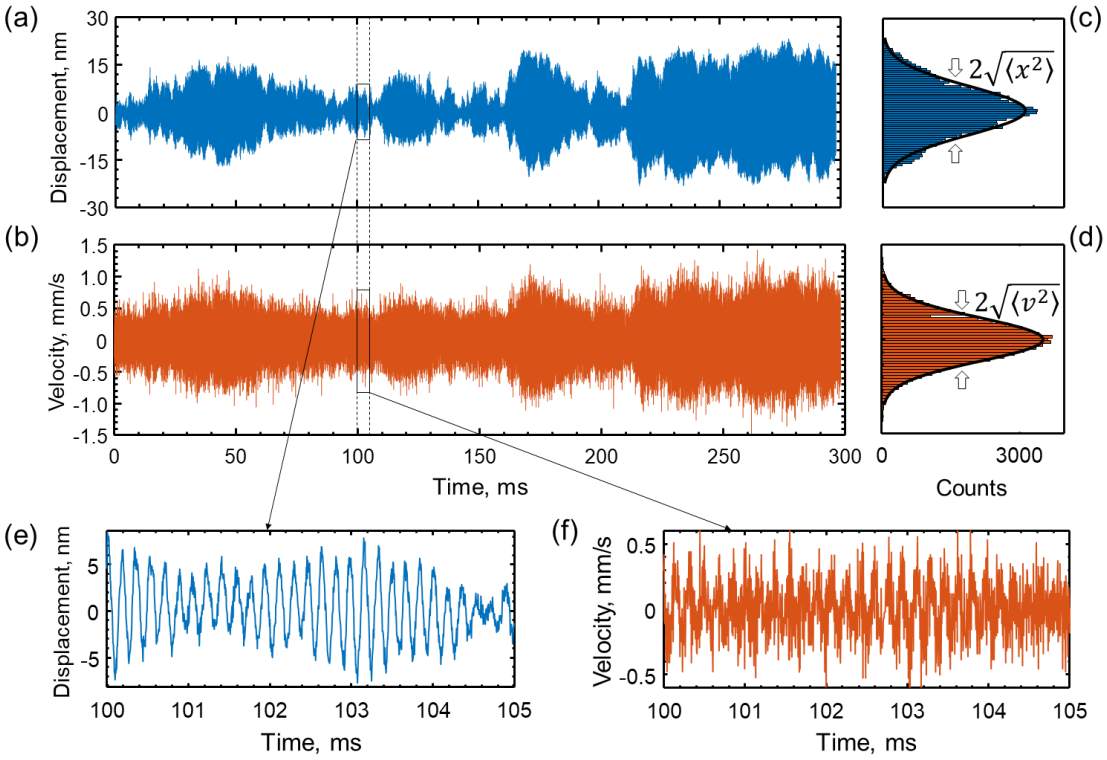

Figure 4.2 **Thermomechanical motion of a gold nano-membrane cantilever measured by free electron edge scattering.** Time series recording of displacement (a) and corresponding [derived] velocity (b) of the tip of a cantilever moving in its fundamental flexural mode under vacuum. (c) and (d) show corresponding displacement and velocity distributions. Overlaid black lines are Gaussian fittings. (e) and (f) show zoomed in sections of (a) and (b) respectively, in which the oscillatory period of the mode θ = 1.75×10^{-4} s is resolved.

To reveal the detailed nature of nano-membrane cantilever thermal motion, from the experimental data we evaluate mean squared displacement $\langle [\Delta x(\tau)]^2 \rangle$ as a function of observation time τ (Figure 4.3a). For small observation intervals $\tau \ll \theta$ (where θ = 1.75×10^{-4} s is the oscillation period of the cantilever) the mean squared displacement $\langle [\Delta x(\tau)]^2 \rangle$ grows quadratically with τ. This is direct evidence of the ballistic motion regime, as it means that velocity is constant over the observation interval. This is confirmed by the normalized velocity autocorrelation function $\langle v(t)v(t+\tau) \rangle / (k_B T/m_{eff})$ plotted in Figure 4.3b, which evaluates how close the velocity at the end of the observation period is to the velocity at the beginning. At short time intervals, the near-unity value of the autocorrelation function is again explicit evidence of the ballistic regime. From

Figure 4.3a one can conclude that over intervals up to ~10^{-5} s the cantilever essentially moves ballistically over average distances up to 3 nm.

In essence, the ballistic regime implies that within a short observation interval $\tau \ll \theta$, the natural oscillation of the cantilever is not significantly disturbed by momentum transfer related to the annihilation and creation of individual flexural phonons. Here, the emission and absorption of thermal photons makes a negligible contribution because of their low momentum. At room temperature (T = 300 K) the average number of thermal phonons [30, 119] with energy $\hbar\omega_m$ in the flexural mode is $\bar{n}_{thermal} \approx k_B T/(\hbar\omega_m)$ = 1.1×10^9, while the average lifetime of the flexural phonons can be evaluated as $(\bar{n}_{thermal}\gamma_m)^{-1}$ = 13 ps, during which time the cantilever moves an average distance of $\sqrt{\langle v^2\rangle}/(\bar{n}_{thermal}\gamma_m)$ = 3.9 fm. One can observe that phonon momentum transfer events begin to affect the ballistic regime of natural oscillation only when the observation intervals τ > 10^{-5} s, i.e., about 6% of the oscillation period θ. During this period of observation $(\bar{n}_{thermal}\gamma_m)\tau$ ~10^6 phonons out of the ~1.1×10^9 in the mode are created and dissipated.

For longer observation periods, $\langle[\Delta x(\tau)]^2\rangle$ becomes a complex oscillating function of τ. A truly diffusive regime, wherein $\langle[\Delta x(\tau)]^2\rangle \propto \tau$ and which is characteristic of free Brownian particle movement, is not observable in underdamped cantilevers, where the dynamics are affected by a restoring force. The statistical properties of cantilever thermal motion are described by the Langevin model [83, 84] for a harmonic oscillator (as discussed in section 2.2): $\ddot{x} + \gamma_m\dot{x} + \omega_m^2 x = F_{thermal}(t)/m_{eff}$, where $F_{thermal}(t) = \sqrt{2k_B T\gamma_m m_{eff}}\eta(t)$ is the thermal force related to the dissipation factor γ_m through the fluctuation-dissipation theorem [67], k_B is the Boltzmann constant, and $\eta(t)$ is a delta-correlated normalized white noise term: $\langle\eta(t)\rangle = 0$; $\langle\eta(t)\eta(t')\rangle = \delta(t-t')$. There is a good correlation between experimental data (blue data points in Figure 4.3ab) and the Langevin model predictions (orange lines)

$$\langle[\Delta x(\tau)]^2\rangle = \langle|x(t) - x(t+\tau)|^2\rangle = \frac{2k_B T}{m_{eff}\omega_m^2}\left[1 - e^{-\frac{\tau}{2\tau_b}}\left(cos\omega_1\tau + \frac{sin\omega_1\tau}{2\omega_1\tau_b}\right)\right] \qquad (4.1.1)$$

over the entire range of observation times, particularly at $\tau << \theta$ where the value of $\langle[\Delta x(\tau)]^2\rangle$ accurately follows the $\tau^2\left(k_B T/m_{eff}\right)$ dependence derived from the model. $\omega_1 = \sqrt{\omega_m^2 - (\gamma_m/2)^2}$ being the damped angular frequency. The analytical curves are not fittings to the data using any kind of scaling parameters – the near-perfect match seen in Figure 4.3 is obtained using only the measured values of m_{eff}, ω_m and γ_m.

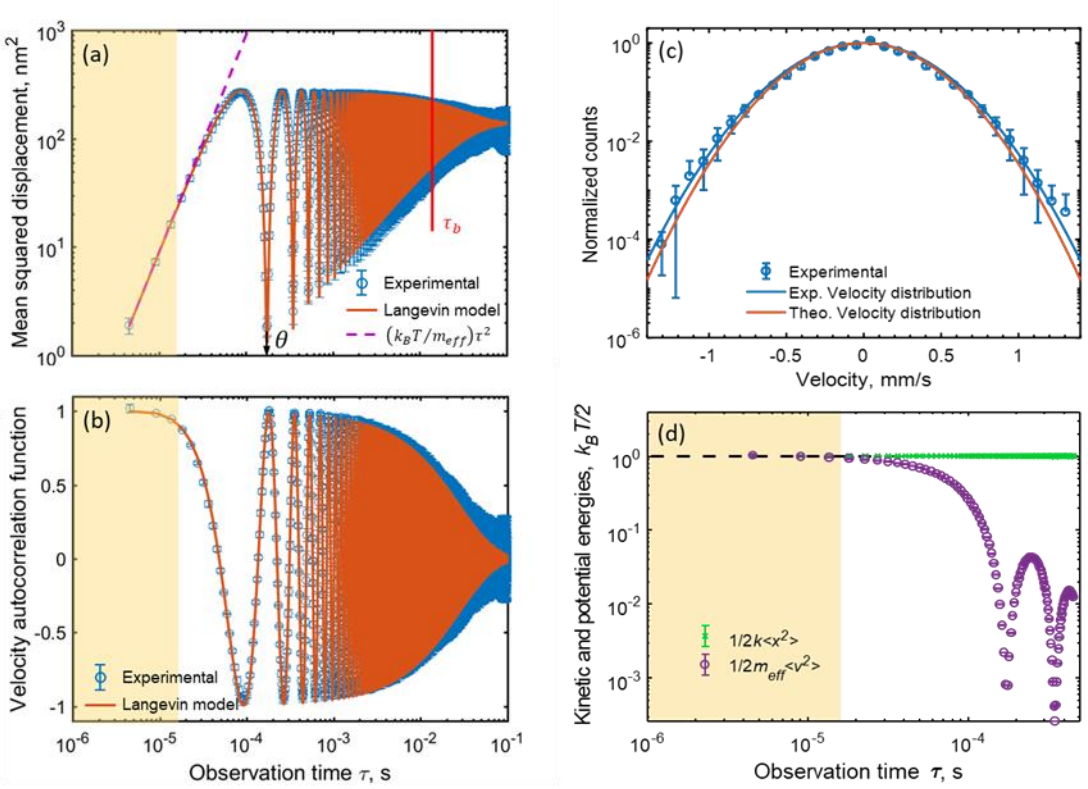

Figure 4.3 **Statistics of nano-membrane cantilever thermal motion - comparison between experiment and analytical theory.** (a) Mean squared displacement $\langle[\Delta x(\tau)]^2\rangle$ of the membrane cantilever tip as a function of the observation time interval τ. Experimental data are plotted as blue circles; The orange line is derived from the Langevin model for thermal motion of a harmonic oscillator; The violet dashed line is an asymptote for ballistic motion at a constant velocity of $\sqrt{k_BT/m_{eff}}$ = 0.297 mm/s. (b) Normalized velocity autocorrelation function $\langle v(t)v(t+\tau)\rangle/(k_BT/m_{eff})$ as a function of the observation time interval, again showing experimental data (blue points) overlaid with analytical theory (orange line) (c) Measured cantilever tip velocity distribution for an observation time interval τ = 4.7 μs [blue circles]. Solid lines are Maxwell-Boltzmann distributions: blue, as a best-fit to the experimental data, with $\sqrt{\langle v^2\rangle}$ = 0.303 mm/s; Orange, with $\sqrt{\langle v^2\rangle}$ = 0.297 mm/s from equipartition theorem. (d) Experimentally measured values of $\frac{1}{2}k\langle x^2\rangle$ [potential energy, green symbols and line] and $\frac{1}{2}m_{eff}\langle v^2\rangle$ [kinetic energy, purple line] as functions of the observation time τ. At short timescales, where v represents the well-defined ballistic velocity, the latter equates to kinetic energy. Error bars on experimental data points represent the standard deviation over a number of repeated independent measurements. Yellow shaded zones in (a), (b) and (d) denote the ballistic regime.

In the ballistic regime of motion ($\tau \ll \theta$) nanomembrane cantilever velocity v is well defined, so the distribution of velocities over an ensemble of sampling events can be established, as plotted in Figure 4.3c for the shortest observation interval τ = 4.7 μs. A Maxwell-Boltzmann velocity distribution fitting

$$f(v) = \sqrt{\frac{m_{eff}}{2\pi k_B T}}\, exp\left(-\frac{m_{eff}v^2}{2k_BT}\right) \tag{4.1.2}$$

to the data yields variance, i.e., a root-mean-square velocity $\sqrt{\langle v^2\rangle}$= 0.303 mm/s that is well-matched to the value obtained from energy equipartition theorem: $\sqrt{k_BT/m_{eff}}$= 0.297 mm/s. The small 2% discrepancy between these values is related to the shot noise of the electron beam current in the experimental case. Compliance with the equipartition theorem, which stipulates that the

Boltzmann energy $k_B T$ should be equally distributed between potential and kinetic energies of the cantilever is also illustrated in Figure 4.3d. Figure 4.3d shows experimental values of $\frac{1}{2}k\langle x^2\rangle$ and $\frac{1}{2}m_{eff}\langle v^2\rangle$ as functions of the observation time interval τ ($k = m_{eff}\omega_m^2$ being the cantilever's spring constant). The former equates to the potential energy of the cantilever; the latter equates to kinetic energy *only* at short intervals $\tau \ll \theta$, where v represents the well-defined ballistic velocity. Convergence of the two traces at short timescales thereby confirms equipartition of kinetic and potential energies in the ballistic regime (the yellow shaded band in Figure 4.3d).

The observations of the thermomechanical motion of a nano-membrane cantilever reveal the following dynamics: At short timescales, up to about 10 μs the membrane moves with constant velocity (i.e. ballistically), with the average displacement being directly proportional to the observation time interval. Brownian-like dynamics emerge for longer observation times, when membrane motion is caused by multiple phononic creation/annihilation events: average displacement becomes a sub-linear function of the observation time. When length of the observation interval becomes equal to the natural oscillation period, average displacement reaches a minimum. For intervals much longer than the oscillation period, the mean squared displacement $2k_B T/\left(m_{eff}\omega_m^2\right)$ is proportional to temperature and is independent of observation time. High sampling-rate measurements of the instantaneous trajectory of the cantilever provide direct verification of the thermal equipartition theorem and the Maxwell-Boltzmann distribution of velocities for the membrane.

4.2 Experimental method on ballistic motion detection

The displacement measurements technique is based on monitoring the secondary electrons flux created by scattering of the tightly focused electron beam on the sharp edge on the moving object as developed in Chapter 3. In this measurement, a focused electron beam with acceleration voltage V = 5 kV and a beam current I_e = 690 pA (larger spot size will give larger linear measurement regime reducing high electronic harmonic signals) incident on the vertical edge center of cantilever tip to pick out the fundamental flexural thermal oscillation at room temperature in high vacuum of 2.6×10^{-6} mbar. In order to obtain more projection of movement into the plane perpendicular to the incident electron beam, sample was attached on a 45-deg pretilt stub. The structure's thermal movement is probed at different positions using focused electron beam to discern the mode shapes of the first 3 mechanical modes. Figure 4.4b-f show the Fourier transform of the position autocorrelation function (i.e., position power spectral density, PSD) obtained from the measured real time displacement $\delta\boldsymbol{r}(t)$.

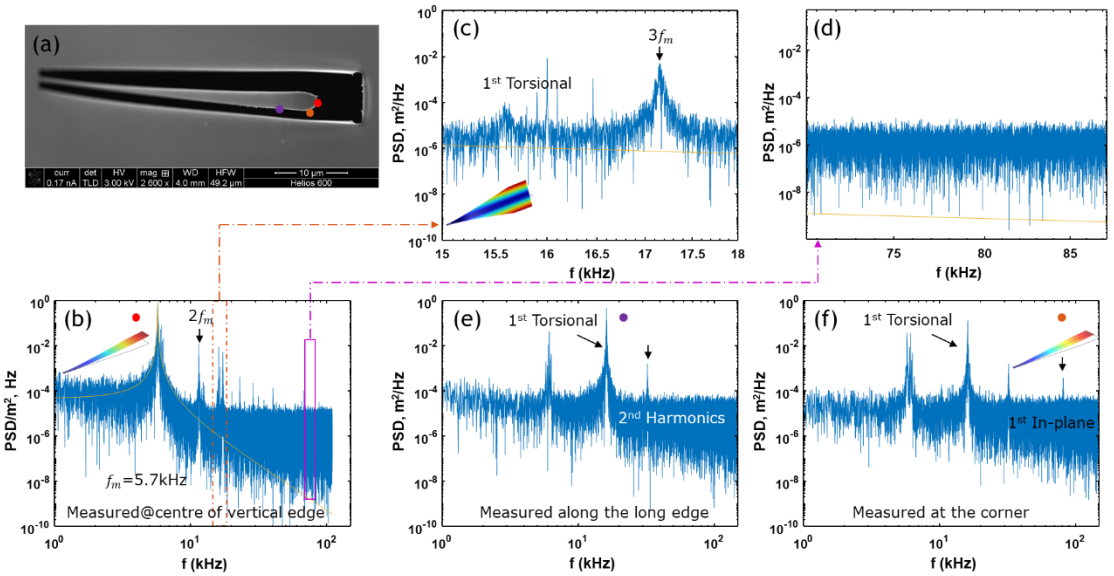

Figure 4.4 **Experimental evidence of separating out the fundamental out-of-plane mode.** (a) Measuring 45-degree tilted cantilever sample at 3 different noted positions. (b) Displacement power spectral density (PSD, obtained from the real time position measurement) in unit of nm^2/Hz of the cantilever measured at the centre position of unclamped end at noted by red dot in (a). Fundamental out-of-plane mode is clearly measured as shown by the resonance peak around 5.7 kHz. The peak around frequency of 11.4kHz is the second harmonics. (c) zoomed in of (b) reveals resonance around 15.7 kHz corresponds to the first torsional mode. (d) zoomed in section of the spectrum from panel (a), reveal no detectable thermal vibration within this frequency range when focusing the electron beam at the centre of the cantilever, along its vertical edge. (e) Measurement at the long edge of the cantilever reveals the torsional oscillations. (f) Displacement PSD measured at the corner of cantilever reveals Brownian oscillations of all three modes.

As can be seen in Figure 4.4b, when measuring at the center of the vertical edge as indicated by the red dot in Figure 4.4a, fundamental out-of-plane mode is revealed with good signal to noise ratio. The effective mass m_{eff} and mechanical quality factor Q for the cantilever's fundamental oscillatory mode are obtained by fitting the following analytical expression for displacement power spectral density Equation (2.2.10).

As indicated by the purple dot in Figure 4.4a, while measuring along the horizontal long edge away from its tip part clearly reveal the fundamental torsional mode (Figure 4.4e). Also, if one measured at the corner of the cantilever as indicated by the orange dot in Figure 4.4a, all 3 modes can be clearly revealed with fundamental in-plane mode showing by peak around 80 kHz in Figure 4.4f. As can be seen from Figure 4.4c, zoomed frequency range of Figure 4.4b, fundamental torsional mechanical movement signal around 15.7 kHz is suppressed by 4 orders of magnitude while the fundamental in-plane mode signal at ~ 80 kHz (see Figure 4.4d) is well below the shot-noise level when measuring at the center of the vertical edge of the cantilever. One can also see spurious signals at integer multiples of the strongest modulation frequencies (i.e. high-order harmonics) in Figure 4.4b-c,e due to the nonlinear transduction [120] of movement at larger displacement.

4.3 Disturbance of cantilever movement by the probe electron-beam

In keeping with prior works [105] I assume that around 2.5% of incident electron beam power is absorbed as heat $H_{abs} = 0.025 I_e V$ ~100 nW. Using evaluation method described in section 3.5.3, the cantilever temperature is increased by electron bombardment by δT ~ 0.4 K resulting in a negligible relative increase of the root mean square thermal displacement of the cantilever by only one part in $(\sqrt{1 + \delta T/T} - 1)$ ~7×10^{-4}.

The force related to momentum transfer from the electron beam is $F_{rad} = \frac{I_e}{e}\sqrt{2E_e m_e}$ ~1.6×10^{-13} N. Assuming a spring constant for the cantilever of 60 μN/m (from finite element modelling), this is sufficient to induce static tip displacement of ~2.6 nm. This is much smaller than the (30 nm) thickness of the cantilever, equating to cantilever rotation about the anchor point of only ~0.002°, and is of negligible consequence to its thermal motion dynamics.

4.4 Summary

To conclude, based on the technique developed in Chapter 3 and incorporating the new dimension of microsecond temporal resolution, in this chapter I have reported the first observation of the ballistic regime of thermal movements of a microcantilever membrane driven internally by momentum transfer from the annihilation and creation of the flexural phonons under vacuum, thus unveiling the physics of thermodynamics in micro/nano-mechanical structures.

The measured ballistic regime behaviour agrees very well with the one predicted by the Langevin model: membrane moves with constant velocity (i.e. ballistically), with the average displacement being directly proportional to the observation time interval. Over intervals up to ~10^{-5} s, the cantilever essentially moves ballistically over average distances up to 3 nm.

High sampling-rate measurements of the instantaneous trajectory of the cantilever provide direct verification of thermal equipartition theorem and the Maxwell-Boltzmann distribution of velocities for the membrane.

Chapter 5 Subatomic optical localization beyond thermal fluctuations

Is optical imaging and metrology of nanostructures exhibiting Brownian motion possible with resolution beyond thermal fluctuations? Over the past decade, spatial resolution in far-field optical imaging and metrology has improved far beyond the classical Abbé diffraction limit of $\lambda/2$, where λ is the wavelength of light. Nonlinear STED (stimulated emission depletion) and statistically enhanced STORM (stochastic optical reconstruction microscopy) techniques used in biological imaging [98, 100] now routinely achieve resolution of a few tens on nanometres, or better than $\lambda/10$. The application of artificial intelligence to the analysis of coherent light scattered by an object offers metrology with an accuracy of only a few nanometres, or better than $\lambda/100$ [121], on a par with scanning electron microscopy.

In this chapter I demonstrate an approach to optical measurements with absolute error reaching a previously unimaginable level of $\lambda/10{,}000$ – a "sub-Brownian" length scale, equivalent to a fraction of the typical size of an atom, and several times shorter than the thermal motion amplitude of the target objects and the resolution of transmission electron (cryo)microscopy. In single-shot measurements one can determine object dimensions through a deep learning-enabled analysis of its scattering pattern when it is illuminated with coherent, topologically structured light (e.g., super-oscillatory (SO) light) containing deeply subwavelength singularity features.

In section 5.1, research background and basics of optical superoscillations are reviewed followed by the methods for designing and experimental generation of a super-oscillatory focus as described by our former group member's work in refs. [122, 123] that are illustrated in section 5.2. Fabrication and characterisation of the nano-electro-mechanical double slit are described in section 5.3. Methodology and experimental results for deep learning-enabled optical measurements of nanowire position is presented in section 5.4 with details of the neural network architecture, training, and application procedures illustrated in section 5.4.1. Experimental results in terms of optical measurement under the illuminations of super-oscillatory and 'plane-wave' and analysis on the advantage of super-oscillatory light in metrology application are discussed in section 5.4.2.

5.1 Optical superoscillation

A systematic review of optical superoscillation can be found in refs. [124, 125]. Superoscillations are band-limited functions with the counterintuitive property that they can vary arbitrarily faster than their fastest Fourier component, over arbitrarily long intervals. Optical superoscillations are

rapid, subwavelength spatial variations of the intensity and phase of light, occurring in complex electromagnetic fields formed by the interference of several coherent waves [125]. The discovery of superoscillations stimulated a revision of the limits of classical electromagnetism — in particular, the studies of phenomena such as unlimitedly small energy hotspots, phase singularities, energy backflow, anomalously high wavevectors and their intriguing similarities to the evanescent plasmonic fields on metals [125]. Systematic study of optical superoscillations was recently revived in the context of quantum mechanics after Aharonov [126] showed that weak quantum mechanical measurements can have values outside the spectrum of the corresponding operator. In other words, a 'local' measurement of a value, such as the wavenumber of an optical wave, can be outside the range seen when a global measurement is taken [127]. In 2006, Berry and Popescu [128] showed that this implied optical waves could form arbitrarily small spatial energy localizations that propagate far from a source, and without the need for evanescent waves. However, only a small fraction of energy of the electromagnetic field can exist in the form of a superoscillation. Ferreira and Kempf showed [129] that the energy that can be channelled into the superoscillatory region decreases exponentially with the number of superoscillations. This is a particularly important and prohibiting limitation if one would like to use superoscillations for communication of high-frequency information using a low-bandwidth communication line. The energy channelled into the super-oscillatory region also increases with the speed of oscillation, but only polynomially. In optics this means that as the size of an optical hot-spot is reduced, polynomially less energy of the wave can be concentrated in the hot-spot. The latter fact is crucial for optical superoscillation to be applied for sub-wavelength light localization and imaging [125]. In principle, there are no limitations on the size of the hot-spot: it can be as small as we wish, providing we do not care how much energy it contains. However, it is the energy of the hot-spot and noise characteristics of the device that determines the practical limits of how small the hot-spot can be while remaining useful in imaging or light-localization applications such as manufacturing with light or data recording [124, 125].

While superoscillation may sound like an exotic and complicated phenomenon, it is often present in complex field patterns but can remain unnoticed due to their small amplitudes. For instance, following the approach of [130], it can be demonstrated simply in a one-dimensional wave consisting of six spatial Fourier components:

$$f(x) = ae^{i\varphi} = \sum_{n=0}^{5} \left(a_n e^{i2\pi nx}\right) \tag{5.1.1}$$

where a_n are the Fourier coefficients (here a_0 = 19.0123, a_1 = −2.7348, a_2 = −15.7629, a_3 = −17.9047, a_4 = −1.0000, a_5 = 18.4910.)

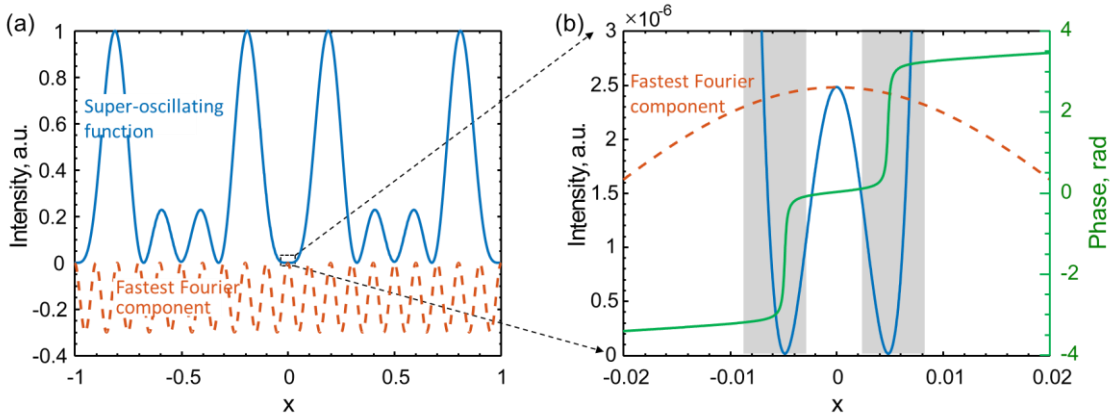

Figure 5.1 **One-dimensional superoscillation with discrete spectrum.** (a) a super-oscillatory function (solid blue line) and its fastest Fourier component (dashed orange line). (b) Zoom of the function near the origin showing a narrow peak with rapidly oscillating phase (solid green line) in the nulls on either side. The super-oscillatory region is shaded in grey [130].

Figure 5.1a shows the intensity of the wave $|f(x)|^2$ and its fastest Fourier component $\cos(k_{max}x)$ with k_{max} = 10π. The function appears to oscillate slowly compared with the fastest Fourier component, but if we examine the low intensity region near x = 0 (Figure 5.1b), then one can see that there is an extremely narrow peak, about 10 times narrower than the fastest Fourier component! This peak demonstrates two of the characteristics of superoscillation, firstly that super-oscillatory features are generally of low intensity, and secondly that the phase φ is rapidly oscillating in the super-oscillatory region (green solid line in Figure 5.1b). The rapidly oscillating phase is often used as a signature of superoscillation: a function is said to be super-oscillatory in a region where the phase gradient $k_{local} = d\varphi/dx$ is greater than that of the fastest Fourier component of said function, $k_{local} > k_{max}$. That is, the optical field is super-oscillatory if the local wavenumber is greater than the maximum wavenumber presents in the wave. This super-oscillatory region is shaded in grey Figure 5.1b.

5.2 Designing and generation of an optical superoscillation

5.2.1 Designing an optical superoscillation

In 2006, Berry and Popescu [128] showed theoretically that superoscillations could be created by a properly designed diffraction grating, and that they could propagate a significant distance from that grating. Their demonstration considered the evolution of the particular super-oscillatory function

$$f(x) = (\cos x + ia\sin(x))^N \qquad (a > 1, N \gg 1) \tag{5.2.1}$$

both as a quantum mechanical wavefunction and an optical field in the paraxial approximation. They showed that as the optical field propagates away from a grating that created it, the super-oscillatory sub-wavelength features are maintained over much greater distances than normal

evanescent features. They showed that, while diffraction causes the superoscillations to become larger, they can maintain their super-oscillatory nature over a distance of up to 14 wavelengths. This demonstration was extended to non-paraxial wave propagation in [131]. Indeed, as sketched in Figure 5.2a, the field cross section at the hot-spot along the direction parallel to the plane of the array may be presented as a superposition of partial waves emanated from individual holes/slits of the binary mask:

$$E(x) = \sum_n a_n \cos\left(k_n^{||} x + \varphi_n\right) \tag{5.2.2}$$

Such a superposition resembles the structure of a super-oscillating function (5.2.1): for a certain combination of partial amplitudes a_n, spatial frequencies $k_n^{||}$, and phases φ_n, superoscillation features are created, similar to those illustrated in Figure 5.1. By designing and optimizing the arrangement of the slits array, one can obtain a one-dimensional super-oscillatory hot spot focusing as shown in Figure 5.2b.

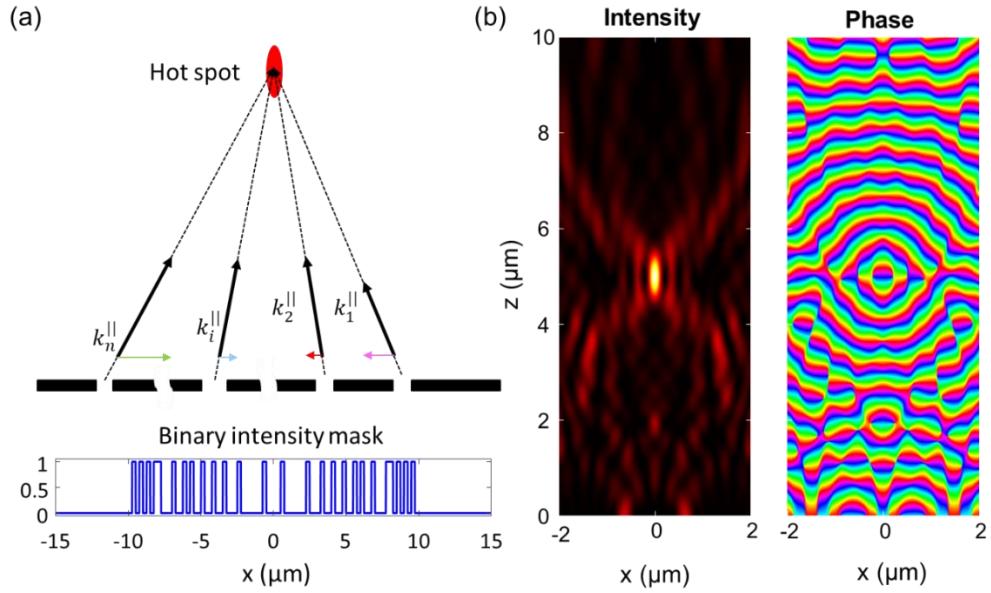

Figure 5.2 **Formation of a superoscillatory feature by light diffracted on the hole/slit array.** (a) Light diffracted through an optimized binary mask forming a super-oscillatory feature. This essentially is equivalent to an array of segmented plane wave source that interfere with each other and generates a cylindrical superoscillatory focusing in the far field. (b) Simulated intensity and phase mappings using Lumerical FDTD Solutions.

Superoscillations are also remarkably common in random systems. It was shown that on average one third of the area of a two-dimension speckle pattern was super-oscillatory and this was extended to waves in more dimensions [124, 125]. Despite the abundance of naturally occurring superoscillations, it is also possible to instructively design a generator of an optical field with particular super-oscillatory features, such as a hot-spot of a particular profile. To do this, the spot is specified within a given field of view (FoV) as shown in Figure 5.3a; outside this field of view (that

is in the sideband region) the intensity is allowed to take any value. Indeed, it has been shown in [132] that any arbitrarily small field feature can be represented as a series of bandlimited functions if we are concerned only with a prescribed field of view. This may be achieved using the formulism of prolate spheroidal wavefunctions (PSWF) developed by Slepian and Pollack [133]. This is a complete set of functions which are orthogonal both within the limited field of view and across all space (including any sidebands). The main feature of prolate spheroidal wavefunctions is that they are bandlimited and therefore can be formed from conventional plane propagating waves. Therefore, the desired sub-wavelength hot-spot is represented as a sum of prolate spheroidal wavefunctions (Figure 5.3b), which can be truncated when a satisfactory level of approximation is achieved. Using the method described in [123], Figure 5.3c-f show the generated sub-wavelength super-oscillatory hot spot with FoV = 2λ and FWHM = 0.42 λ at wavelength λ = 488 nm from superposition of two circular prolate spheroidal functions $E(r/\lambda) = 4.477\, S_3(r/\lambda) + S_4(r/\lambda)$, where r is radial distance from the beam axis.

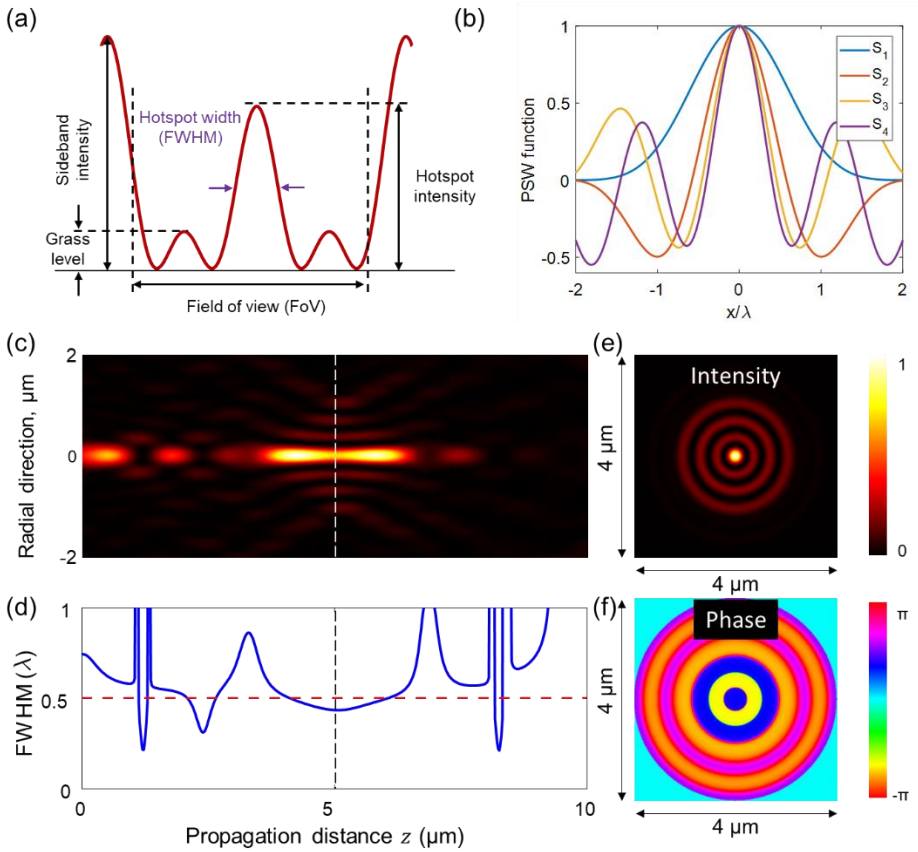

Figure 5.3 **Superoscillatory hot spot generated by superposition of circular prolate spheroidal wavefunctions.** (a) Important parameters of a superoscillatory spot: the ratio of hot-spot and sideband intensities is a measure of conversion efficiency; the field of view, i.e., the area around the hot-spot which is not illuminated by sidebands, the ratio of the peak hot-spot intensity to the grass level intensity determines the finesse of optical fabrication and the noise level of imaging instruments. (b) First four terms of prolate spherical wavefunctions (PSWF). (c) A super-oscillatory focusing generated by the superposition of PSWF function $E(r/\lambda) = 4.477\, S_3(r/\lambda) + S_4(r/\lambda)$. Intensity profile of the designed field along propagation direction. (d) Calculated full width half maximum (FWHM) value of the field along propagation direction. Simulated intensity (e) and phase (f) profiles in the transverse plane (z = 5 μm as indicated by the dashed lines in (c-d)). One can see several zones of phase jump and/or singularities.

5.2.2 Super-oscillatory light generation

A super-oscillatory hot spot can be experimentally generated through a super-oscillatory lens (SOL), spatial light modulators (SLM) and digital mirror devices (DMD) [125]. Currently, most super-oscillatory lenses are constructed with binary intensity or phase masks. The particle swarm optimization (PSO) algorithm has been widely employed [124]. Typically, the merit functions for optimization include the size of the central spot (FWHM), numerical aperture and size of the usable field of view (FoV). Super-oscillatory focusing can also be achieved using spatial light modulators (SLM) and a conventional microscope objective that focuses a beam with a carefully designed amplitude and phase profile using the method in the previous section (5.2.1) for precise tailored interference as shown in Figure 5.4. In experiment, a spatial light modulator for super-oscillatory hot spot generation as described by our former group member's work in [122] was used. An input beam from a fibre-coupled laser is expanded and collimated, and is incident on an amplitude shaping SLM. The amplitude modulated beam is then imaged onto a phase modulating SLM, using a 4-f system. This phase and amplitude spatially modulated beam are then demagnified and imaged onto the back focal plane of the microscope objective: the field on SLMs and the focal plane of the objective are then related by a Fourier transform. In this setup any arbitrary field profile may be obtained at the microscope focal plane simply by encoding its Fourier transform on the SLMs.

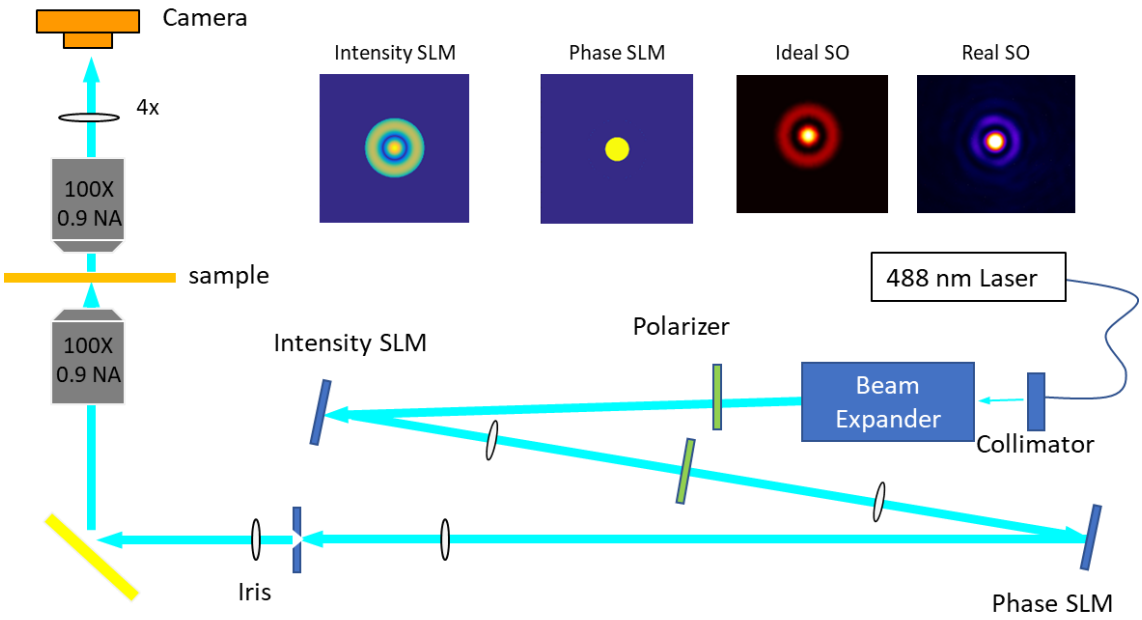

Figure 5.4 **Creating superoscillations with spatial light modulators.** Schematic of the setup for super-oscillatory (SO) focusing with SLMs. Light from a fibre-coupled laser is collimated, expanded, polarized and is incident on an amplitude modulating SLM. This beam from this SLM is imaged onto the phase SLM with a 1:1 telescope, and then demagnified onto the black focal plane of a microscope objective using a further telescope system.

SLM-based super-oscillatory focusing, while similar in principle to focusing with binary SOLs, has a number of experimental differences [124, 125]: The SLM approach allows focal spots to be formed

at the focus of a microscope objective, giving a working distance of at least a few hundred microns, compared to the few tens of microns currently seen with binary SOLs, making experiments on rough surfaces or within thick objects easier. SLM focusing is also more suitable for reflection, or epi-fluorescence, imaging, as it does not require a double pass through a binary SOL, but only through a standard microscope objective, and it may also be more suitable for optical scanning of the super-oscillatory spot as performed in a laser scanning confocal microscope. On the other hand, the SLM system is more complex to align, consisting of a number of optical components and considerable free-space path length. The binary SOLs have only one component and require only a relatively easy to achieve collimated laser beam as input. The SLM system is also sensitive to aberrations in the optical system. Although these are somewhat corrected for by the eigenmode optimization, this does not remove all aberrations. Both binary SOLs and SLM super-oscillatory focusing rely on the spatial coherence of the input beam.

5.3 Sample fabrication and characterization

Experimentally, the nano-electro-mechanical double slit (Figure 5.5a) is cut by focused ion beam milling from a 50 nm thick Si_3N_4 membrane coated with 65 nm gold and the terminals at the nanowire ends were electrically separated by removing only the gold film layer in selected areas. The in-plane position of the suspended nanowire relative to a fixed edge of the surrounding membrane, i.e. the width of the gap between the nanowire and the membrane edge, could be controlled electrostatically [45] with high precision over a few nanometer range through the application of a DC bias across the gap.

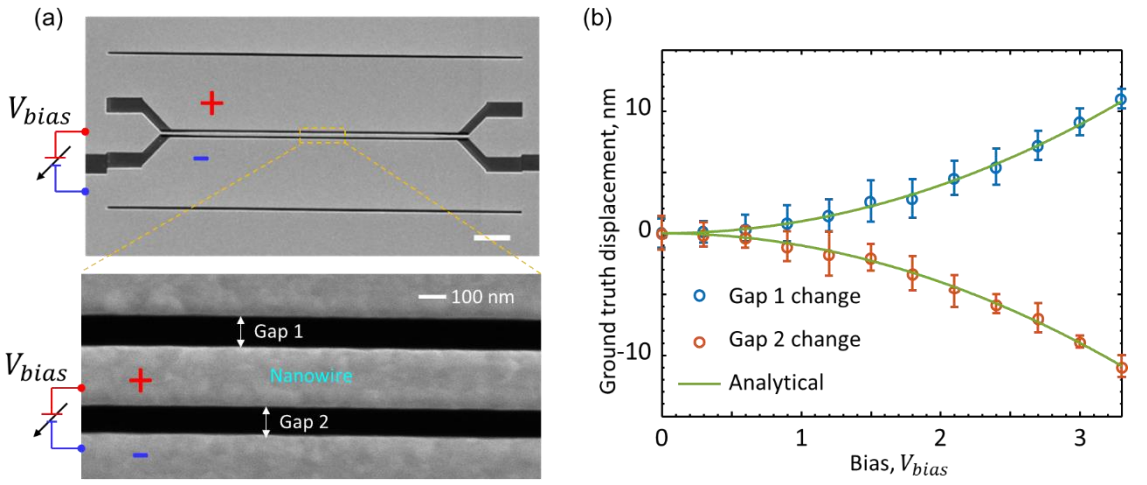

Figure 5.5 **Nano-electro-mechanical double slit and switching behaviour characterization.** (a) SEM image of the fabricated sample. (b) Experimentally measured averaged gap width changes of the two slits or displacement of the nanowire δx as a function of applied bias V_{bias} as shown by data dots [determined from SEM imaging at the different measured positions] with analytical model fitting indicated by lines approaching $\delta x = 0.996 V_{bias}^2$.

The fabricated nano-electro-mechanical device (Figure 5.5a) has slits' width of 100 nm and central nanowire's width of 200 nm and total length of 17 µm including its 1 µm tapered ends of width 100 nm. In order to determine its switching characteristics, the relative width change of two gaps against the bias of large amplitude was measured in a scanning electron microscope (SEM) while taking several images for its averaged displacement determination. The averaged gap width changes or the central nanowire's center of mass position δx approximates to $\delta x \sim \alpha_{fit} V_{bias}^2$ at smaller bias with fitting parameter α_{fit} (depending on nanowire's constituents and geometry) is determined to be 0.996 for the measured sample with analytical model fitting of its switching behavior in Figure 5.5b. Although each measurement by scanning electron microscope has an average uncertainty of ±1.2 nm, 4 measurements over a range of applied bias values enables determination of the quadratic dependence with high precision.

5.3.1 Analytical description of switching characteristics

Elastic nanostructures can be moved by electrostatic forces between charged objects and its electrostatically tunning and switching behaviour can be easily understood theoretically [45, 134, 135]. In the electrostatic (low frequency) limit, here considering the balance of elastic restoring force and electrostatic attraction between an elastic nanowire structure and its neighbouring anchored membrane (Figure 5.6a) separated by a gap g. The restoring force is $F_r = k(g_0 - g) = k\delta x$, where g_0 is the initial gap size and $k \sim 32Yh\,w^3/L^3$ is the spring constant for lateral displacement δx of a nano-bridge, with Young's modulus Y and bridge thickness h, width w and length L. It can be shown from Gauss' law that the electrostatic force between two parallel wires [135] with charge Q_e is $F_e = Q_e^2/(2\pi\varepsilon_0 L(g + w))$ and their gap-dependent capacitance (which determines Q_e) is $C = Q_e/V_{bias} = \pi\varepsilon_0 L/cosh^{-1}(1 + g/w)$, where V_{bias} is the applied voltage. From $F_r = F_e$ follows that

$$V_{bias} = V_0\sqrt{D_r(1 + W - D_r)}\,cosh^{-1}\left(\frac{1 + W - D_r}{W}\right) \tag{5.3.1}$$

$$V_0 = \sqrt{\frac{64Yhw^3g_0^2}{\pi\varepsilon_0 L^4}} \tag{5.3.2}$$

where $D_r = 1 - g/g_0 = \delta x/g_0$ and $W = w/g_0$ are the relative displacement and relative width, g is the gap width of a given DC bias and w is the nanowire width. In the lower voltage regime, the gap width change or the nanowire's center of mass position in equilibrium δx has a quadratic dependence on DC bias as detailed below. However, as the electrostatic force tends towards infinity, the gap approaches zero, there is a threshold voltage V_0, where the elastic restoring force cannot balance the electrostatic force anymore (Figure 5.6b).

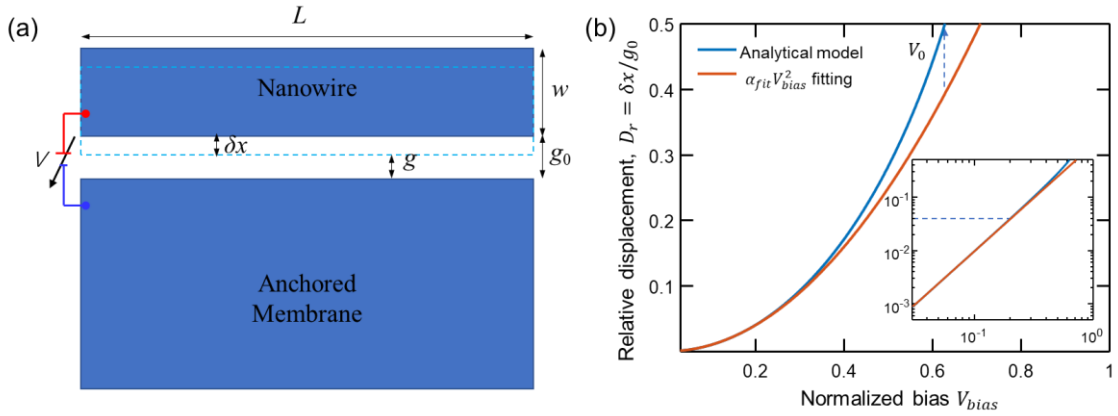

Figure 5.6 **Switching behaviour of the nano-electro-mechanical double slit.** (a) In-plane dimensional schematic of the double slit where nanowire is electrostatically controlled by DC bias. (b) Analytical model of switching characteristics according to equation (5.3.1) and its approximation fitting $\alpha_{fit}V_{bias}^2$ at lower DC bias regime. Dashed line indicated the irreversible switching happens at threshold voltage V_0. Inset: Logarithmic-logarithmic plot of switching dynamics demonstrates the displacement of the nanowire has quadratic dependence on the DC bias in the smaller relative displacement region (dashed line indicates $D_r = 0.04$ as used in experiment for maximum relative displacement).

In order to derive the relationship between the nanowire's displacement and applied DC bias in the lower voltage regime, for simplicity of the derivation, the experiment sample parameters of width w=200 nm and initial gap size g_0 = 100 nm are used and therefore $W = w/g_0 = 2$. Substituting $W = 2$ into Eq. (5.3.1), one can obtain

$$V_{bias} \sim \sqrt{D_r(3-D_r)}\, cosh^{-1}\left(\frac{3-D_r}{2}\right) \tag{5.3.3}$$

Using Puiseux series to expand the inverse hyperbolic cosine function [136], one can obtain

$$V_{bias} \sim \sqrt{D_r(3-D_r)}\sqrt{2\left(\frac{3-D_r}{2}-1\right)}\left[1-\frac{1}{12}\left(\frac{3-D_r}{2}-1\right)+\frac{3}{160}\left(\frac{3-D_r}{2}-1\right)^2 + \cdots\right] \tag{5.3.4}$$

$$V_{bias} \sim \sqrt{D_r}\sqrt{3-D_r}\sqrt{1-D_r}\left[1-\frac{1}{12}\left(\frac{3-D_r}{2}-1\right)+\frac{3}{160}\left(\frac{3-D_r}{2}-1\right)^2 + \cdots\right]$$

$$V_{bias} \sim \sqrt{D_r}\left[c_0 + c_1 D_r + c_2 {D_r}^2 + \cdots\right]$$

For the smaller displacement case: $D_r = 1 - g/g_0 = \delta x/g_0$ (in our experiment the maximum δx = 4 nm and g_0 is 100 nm and maximum $D_r = 0.04$), higher order terms can be reasonably neglected and therefore,

$$V_{bias} \sim c_0\sqrt{D_r} \sim c_0\sqrt{\frac{\delta x}{g_0}} \tag{5.3.5}$$

Thus,

$$\delta x \sim \alpha_{fit} V_{bias}^2 \tag{5.3.6}$$

with fitting parameter α_{fit}. The validity of this approximation can be seen from Figure 5.6b. The gap width change or the central nanowire's center of mass position approximates $\delta x \sim \alpha_{fit} V_{bias}^2$ at smaller bias as shown in inset of Figure 5.6b with fitting parameter α (depending on nanowire's constituents and geometry) is 0.996 for the measured sample, one can see this fitting is valid for relative displacement change D_r<0.1 or δx<10 nm for the measured sample.

5.4 Deep learning-enabled optical measurements of nanowire position

In optical measurement (Figure 5.7), the sample is illuminated, and scattered light is collected in transmission mode via a pair of 100×, NA = 0.9 microscope objectives. The computer-controlled wavefront synthesizer employed in this work is described in detail in section 5.2.2. It is based upon a pair of (Meadowlark P512) spatial light modulators – one for intensity and the other for phase modulation. In the present case, for laser light at a wavelength λ = 488 nm, it was programmed to generate an axially-symmetric superoscillatory wavefront constructed from two circular prolate spheroidal functions $E(r/\lambda) = 4.477\, S_3(r/\lambda) + S_4(r/\lambda)$, where r is radial distance from the beam axis. In the 'plane wave' illumination regime, the synthesizer was configured to generate a defocused Gaussian beam profile having a (measured) intensity variance of only ±5% over the ~400 nm width of the sample (i.e. including the nanowire and gap on either side).

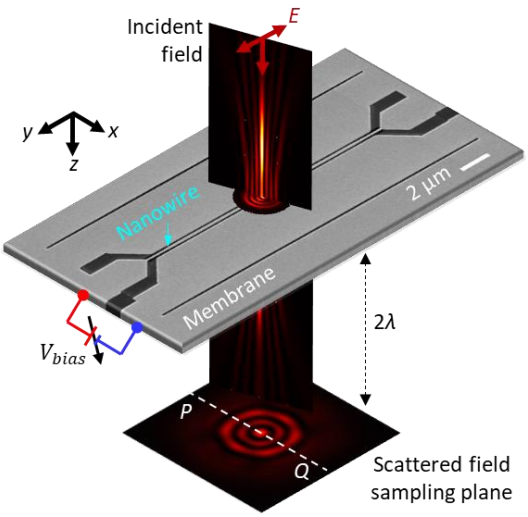

Figure 5.7 **Measuring nanowire displacement via scattering of topologically structured light.** Incident light scattered from the nanowire (in the present case, 17 µm long and 200 nm wide with a 100 nm gap on either side) is imaged in transmission through a high-NA microscope objective (not shown). Deeply-subwavelength lateral (x-direction) displacements of the wire, controlled by application of a DC bias between the wire and the adjacent edge of the supporting membrane, are quantified via a deep-leaning enabled analysis of single-shot scattering patterns.

To enable optical measurements of unknown nanowire positions, a dataset of single-shot scattering patterns recorded at different (electrostatically controlled) positions of the nanowire was created (Figure 5.8). Single-shot scattering pattern images for static nanowire displacements from zero to 4 nm (applied DC bias of 0-2V in 10 mV steps) were recorded. Knowledge of said position is obtained from *a priori* measurement, under a scanning electron microscope, of the dependence of nanowire position on applied bias as discussed in section 5.3.

5.4.1 Neural network architecture, training, and application procedures

As shown in Figure 5.8, eighty percent of these images, selected at random, were used for neural network training, i.e., as scattering patterns for known positions of the nanowire. The trained network was then tasked with determining (nominally) unknown nanowire positions from previously unseen single-shot scattering patterns.

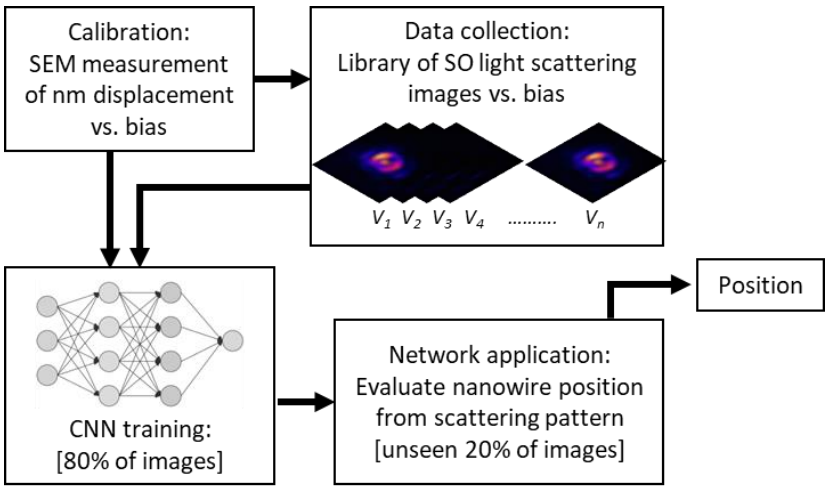

Figure 5.8 **Methodology for deep learning-enabled optical measurements of nanowire displacement.** Using a superoscillatory structured incident light field as example, single-shot scattering pattern images for static nanowire displacements from zero to 4 nm (applied DC bias of 0-2V in 10 mV steps) were recorded. These were analysed using a convolutional neural network (CNN, containing 3 convolutional layers and 3 fully connected layers): 80% of images (selected at random) for training and validation, the other 20% for testing.

The convolutional neural network (CNN) contained three convolution layers with, respectively, sixty-four 5×5, one hundred and twenty-eight 4×4, and two hundred and fifty-six 2×2 kernels, and three fully connected layers with 128, 256, 128 neurons. Each of the convolution layers was followed by a pooling layer with 4×4, 3×3, and 3×3 kernels with Rectified Linear Unit activation functions. The network was trained with the Adam stochastic optimization method and root mean square error loss function. More details on the introduction and implementation of the convolutional neural network can be found in Appendix A.

The experimental dataset comprised scattering intensity patterns imaged with a $9\lambda \times 9\lambda$ (350 × 350 pixels) field of view at a distance 2λ from the sample. These were recorded (for each regime of

illumination) at 201 different electrostatically-controlled positions of the nanowire, with x-direction displacements of ≤4 nm from its zero-bias equilibrium position. 64% of the images (selected at random) were used for network training, 16% for validation, with the remaining 20% then employed for testing (i.e. as scattering patterns for nominally unknown nanowire positions, to be determined by the trained network). For statistical purposes, i.e. to exclude the dependence of measurement outcome on the selection of training images, and their order of appearance in the training set, twenty independent iterations of the training, validation and testing procedure were performed.

5.4.2 Experimental results and discussion

Figure 5.9 shows the results of such measurements, as the absolute error in the optical measurement of nanowire position, retrieved by the trained neural network from the scattering pattern, against the ground truth (*a priori* calibrated) displacement values in the 10-1000 pm range. The statistical spread of datapoints is derived from twenty independent neural network training cycles. Experimental results show that nanowire position can be measured with a mean absolute error of as little as 76 pm using plane wave illumination and 28 pm with superoscillatory illumination. For comparison, the diameter of a silicon atom is ~220 pm.

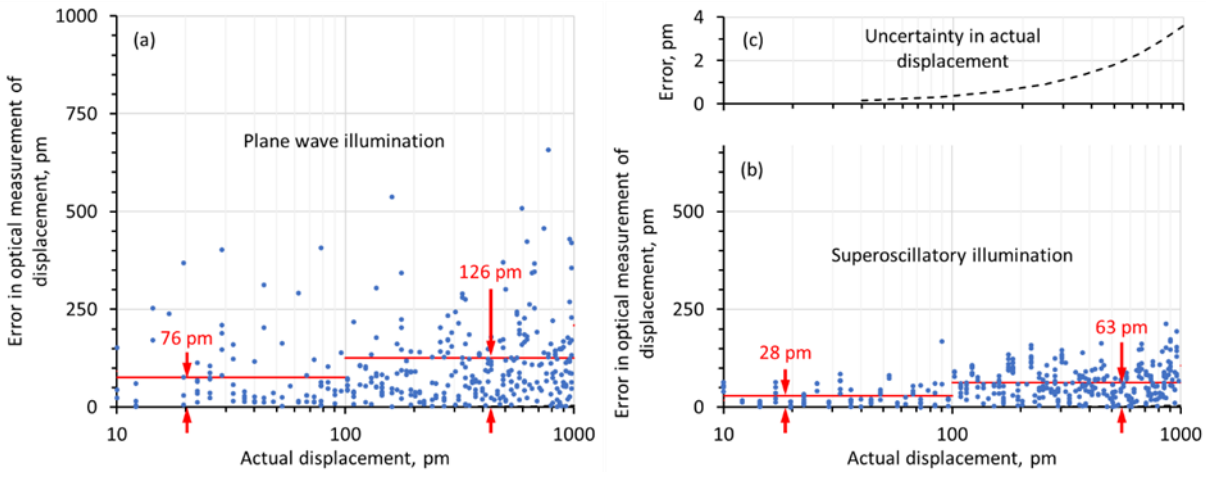

Figure 5.9 **Optical measurements of nanowire displacement.** Absolute error in measurements of nanowire displacement, using (a) plane wave and (b) topologically structured (superoscillatory) light field illumination, against actual displacement. Red horizontal lines show mean absolute errors for order-of-magnitude actual displacement bands, i.e. from 10-100 and 100-1000 pm. (c) Magnitude of uncertainty in actual nanowire displacement.

It's noted that ground truth values of nanowire displacement were independently established by a priori measurements under a scanning electron microscope for a number of different bias settings and interpolated by a quadratic dependence. Indeed, the first non-zero term in the analytical expression for the dependence of nanowire displacement on applied bias must be quadratic as displacement does not depend on the sign of the bias; and higher order terms are negligible while the magnitude of displacement remains much smaller that the gap size (~100 nm). Although each

individual measurement by scanning electron microscope has an uncertainty of ±1.2 nm, a large number of measurements over a range of applied bias values enables determination of the quadratic dependence with high precision. Error propagation analysis yields an uncertainty in ground truth displacements of <0.4% of its value (as shown in Figure 5.9c).

Optical metrology based upon analysis of scattered light is an inverse problem that can be reduced to the Fredholm integral equation, which can be efficiently solved by a neural network [121]. Recent work has demonstrated that this approach yields accuracy better than $\lambda/100$ in measuring the width of gaps in an opaque film with plane wave illumination, using a neural network trained on a set of fabricated samples with a range of different gap sizes [121]. There are two major contributing factors to the hundredfold improvement in mean absolute error reported here: a radically better training process and the use of topologically structured superoscillatory light.

Precisely tailored interference of multiple waves can form intensity "hotspots" in free space, with dimensions smaller than the conventional diffraction limit, as a manifestation of what is known as superoscillation. The electromagnetic field near a superoscillatory hotspot has many features similar to those in the vicinity of resonant plasmonic nanoparticles or nanoholes - hotspots are surrounded by phase singularities and nanoscale zones of energy backflow where phase gradients can be more than an order of magnitude larger than in a free propagating plane waves [137].

The use of such topologically structured light gives an advantage for AI-enabled metrology: The ability to evaluate small changes in the position of the nanowire depends upon the magnitude of associated changes in the scattered light field at distance *z* from the object $A(x,\ z)e^{i\phi(x)} = f\left(A_0(x,0)e^{i\phi_0(x,0)}\right)$, where $A_0(x,0)$ is the amplitude and $\phi_0(x,0)$ is the phase of the incident light in the *xy* object plane as illustrated in Figure 5.10 a-b. A small displacement in the object against the incident field in the *x*-direction results in a change in scattered light intensity $\delta I(x) \sim \delta A_0\ (x,0)^2 + A_0\ (x,0)^2\ \delta\phi_0(x,0)^2$. The first term in this expression is related to the change of illumination intensity associated with the object's positional shift, while the second relates to the corresponding change in phase. The phase-dependent term is absent for plane wave illumination, but can be large under superoscillatory illumination, when the object traverses a small (deeply subwavelength) feature of the incident field, such as a singularity, where the phase $\phi_0(x,0)$ jumps by π.

The responses of scattered plane wave and topologically structured light fields to displacement of an illuminated nanowire are also illustrated, through computational modelling, in Figure 5.10c-f. Numerical simulations were performed using Lumerical FDTD Solutions. Silicon nitride is taken to have a refractive index $n = (2\ +\ 0i)$, while parameters for gold are those by Johnson & Christy. Incident light is polarized parallel to the nanowire and perfectly matching layer (PML) boundary

conditions are used. The incident superoscillatory field was generated through a binary amplitude mask as detailed in Ref. [137].

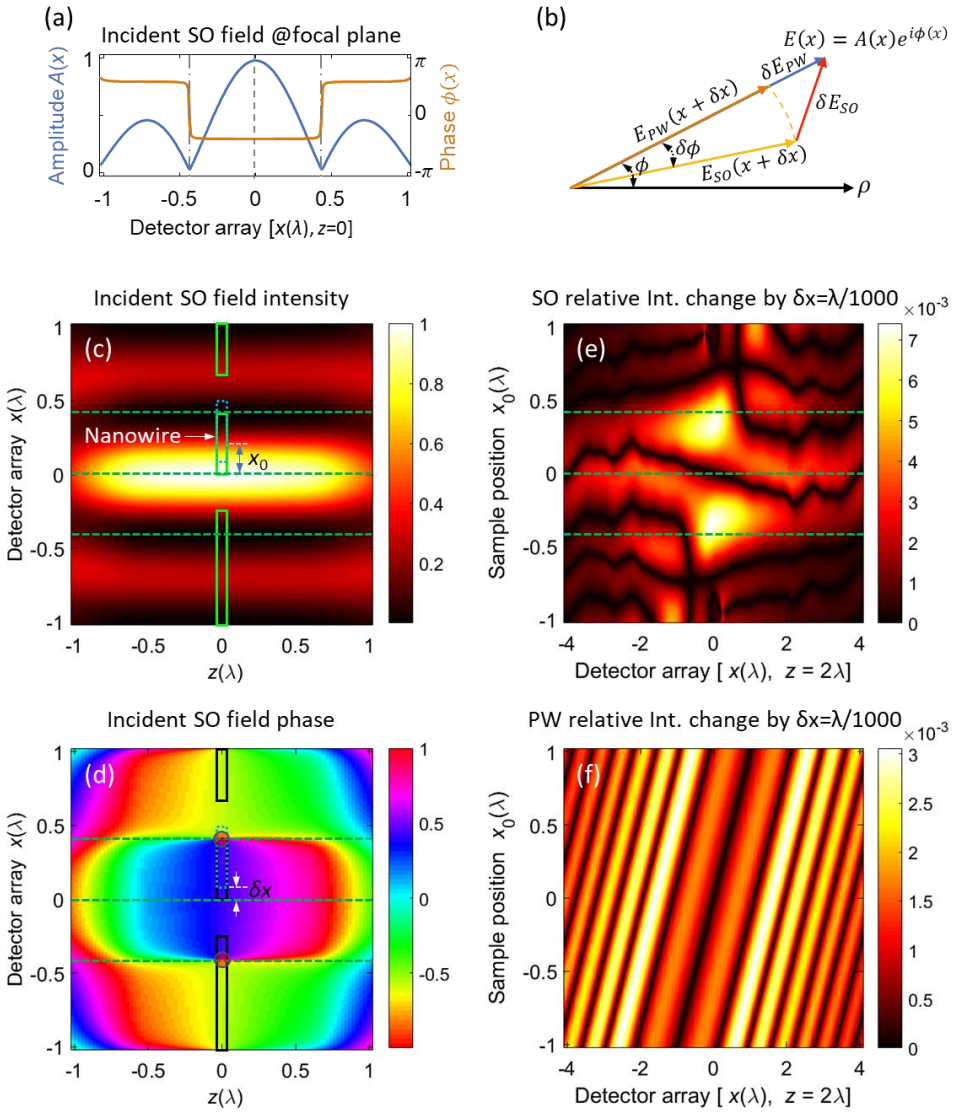

Figure 5.10 **Sensitivity of scattered fields to small nanowire displacements.** (a) Electric field amplitude and phase distributions of the superoscillatory field in the focal plane. (b) Phasor diagram of the electric field change δE induced by a smaller movement δx. For PW illumination, only electric field amplitude change, while structured light induces both amplitude and phase change with larger intensity change. (c) Intensity and (d) phase profiles of the superoscillatory field in the xz plane [light propagating in the +z direction, wavelength λ = 488 nm]. The sample – a nanowire in the gap between two semi-infinite sections of membrane – lies in the z = 0 plane [its cross-sectional profile being shown in green in (c) and grey in (d)]. (e) Relative change in scattered light intensity resulting from a λ/1000 displacement of the sample in x-direction along a cross-sectional line through the scattering pattern in the sampling plane [the line PQ in Figure 5.7] as a function of the initial position x_0 of the sample relative to the symmetry axis of the light field. (f) Corresponding plot of relative change in scattered light intensity for plane wave illumination of the same sample structure.

The incident superoscillatory wavefront (detailed in Ref. [137]) has a central intensity maximum (Figure 5.10c) flanked by phase singularities and zones of high phase gradient (Figure 5.10d). The case where these singularities lie in the nanowire sample plane is considered here. As a figure of merit for the sensitivity of the scattered field to small displacements of the nanowire, Figure 5.10e presents the magnitude of the relative change in scattered light intensity induced by a $\lambda/1000$ (~0.5

nm) shift in nanowire position, as a function of (horizontally) image plane coordinate and (vertically) the initial position of the sample within the structured light field. The scattered field intensity is strongly dependent on both, with largest changes (of up to 0.08%), occurring when a sharp edge of the nanostructure coincides with a phase singularity in the incident superoscillatory field. For comparison, Figure 5.10f shows the same for plane wave illumination. Here, the variations in scattered field intensity are smaller (reaching only 0.03%) and relatively weakly dependent on both image plane coordinate and lateral position of the sample. The contrast between Figure 5.10e and f explains the better mean error of positional measurement achieved with superoscillatory, as compared to plane wave, illumination (Figure 5.9).

The quality of artificial intelligence is directly related to the quality of training data for the neural network. The possibility here to achieve picometric levels of absolute error results firstly from the use of a training set that is ultimately congruent with the object of interest: the same electrostatically reconfigurable nanostructure is used for training and as the object of metrological study. Moreover, ground truth positional displacement values are much more precisely calibrated in this singular electrostatically controlled gap sample (Figure 5.9c) than they are in previously employed sets of mutually independent training samples fabricated with typically few-nanometer tolerance [101, 121].

The reported results represent the first example of "sub-Brownian" optical metrology – the measurement of object dimensions/displacements smaller than the amplitude of its thermal motion. The amplitude of nanowire thermal vibration can be evaluated from the Langevin oscillator model: in the present case, the nanowire's fundamental in-plane oscillatory mode at f_m = 1.6 MHz with effective mass m_{eff} = 2 pg has an average thermal fluctuation amplitude of $\delta x_{RMS} = \sqrt{k_B T/\left(4\pi^2 m_{eff} f_m^2\right)}$ ~ 145 pm at room temperature T= 300 K (k_B is the Boltzmann constant), i.e. a value markedly higher than the achieved (superoscillatory illumination) measurement error of ~30 pm. This is possible because measurements are performed with a detector integration time of ~100 ms and thus return the mean position of the nanowire, which oscillates thermally with a much shorter (~0.6 μs) period. Measurements are single-shot, and do not require scanning of the object, so they can be performed in binning mode, with a frame rate equal to that of the image sensor, which can reach MHz.

5.5 Summary

In summary, in a proof-of-principle experiment using a nano-electro-mechanical double slit sample, the relative positions of nanostructures can be measured with picometric resolution using

scattering of topologically structured light that is far below the reported accuracy [101, 103, 121]. Through artificial intelligence enabled analysis of scattered coherent light, sub-atomic resolution is achievable in single-shot measurements below the thermal vibration amplitude with sufficient exposure time longer than vibration damping time.

In this chapter, I have also analytically studied and experimentally demonstrated that structured light shows superiority in the motion measurement compared with conventional beam as a result of its rapid spatial variations. It's shown that nanowire position can be measured with a mean absolute error of as little as 76 pm using plane wave illumination and 28 pm with superoscillatory illumination. This shows that a nanostructure's position in the plane perpendicular to the direction of light propagation can be accurately measured through scattering patterns when light passes through.

Chapter 6 Optical detection and control of thermal fluctuation in nano-optomechanical metamaterials

The combination of optical resonators and nanomechanical resonators undergoing pico- or nanoscale movement actuated by electromagnetic forces [6, 30], thermal fluctuation [67], and quantum vacuum fluctuations [24, 25], on one hand, has enabled new platforms to efficiently reconfigure optical properties [6, 30] opening up the new field of picophotonics research [22] and applications in frequency conversion [138-143], which are of interest for communications and interfacing quantum systems operating at different frequencies [144]. On the other hand, strong nano-opto-mechanical interaction also enable optical readout of displacement, as discussed in section 1.2, and the control of nanomechanical oscillators as a result of dynamical backaction. This allows mechanical cooling [145], electromagnetic induced transparency [146], topological phonon transport [147], nonreciprocity [148, 149], and can facilitate mechanical nonlinearity leading to hybrid bistability [150, 151], phononic frequency combs [152], and optomechanical dissipative micro-solitons [152] at low laser intensity levels.

In this chapter, I demonstrate optical parametric control of thermomechanical motion in an array of nano-optomechanical resonators. A parametric oscillator is a harmonic oscillator in which oscillations are driven by periodically varying a parameter (such as the mass or spring constant) of the system at a frequency typically different from the natural frequency of the oscillator. I performed experiments on the optical parametric control of thermal motion via modulation of photothermal heating of nanowires; on tunable phononic frequency comb generation at microwatt laser power levels, by combining parametric control of a mechanical oscillator with the action of pondermotive optical forces originating from dipole-dipole interactions within the metamaterial; and on dynamic optomechanical coupling between two distinct doubly-clamped nanowires driven by fluctuating thermal forces, via parametric pumping at the difference frequency of their mechanical resonances. These experiments were conducted with a nano-optomechanical metamaterial sample (a free-standing array of flexible silicon nitride nanowires decorated with pairs of dissimilar silicon nanobricks) fabricated by my colleague Dr Jinxiang Li, and an experimental setup that he developed originally for the study of optomechanical asymmetry [153].

In section 6.1, I present the optomechanical interactions including optical force enhancement within metamaterials and mechanical frequency tuning as a result of a photothermal tuning mechanism, whereby laser-induced heating decreases tensile stress in the nanowires. Section 6.2 details the design and measured optical properties of the nano-optomechanical metamaterial sample used in subsequent experiments, and the optical detection of thermomechanical

fluctuations in the sample is described in section 6.3. Experiments on the parametric control of thermal vibrations and tunable phononic frequency comb generation are presented in section 6.4 together with an analysis of the evolution of thermomechanical spectra and the dynamic photothermal response of nanowires. Lastly, section 6.5 presents experiments demonstrating energy transfer between two parametrically coupled nanowires in a nano-optomechanical metamaterial system.

6.1 Optomechanical effects in photonic metamaterials

Optomechanical interactions in nanomechanically reconfigurable photonic metamaterials are generally of two kinds: first, dissipative interactions such as spring softening effect as a result of optical heating due to the photonic nanostructures' light absorption. And second, interactions underpinned by optical forces, i.e. radiation pressure and the gradient force.

6.1.1 Optical force enhancement within metamaterials

The component of the total averaged force $\langle \boldsymbol{F} \rangle$ acting on a metamaterial structure illuminated with light is calculated using a surface integral: $\langle F_i \rangle = \oiint \langle T_{ij} \rangle n_j dS$, where S is a bounding surface around the metamaterial element, n_j is the unit vector pointing out of the surface and $\langle T_{ij} \rangle$ is the time-averaged Maxwell stress tensor [134, 154]:

$$\langle T_{ij} \rangle = 1/2\, Re\left[\varepsilon_r \varepsilon_0 \left(E_i E_j^* - 1/2\, \delta_{ij} |E|^2\right) + \mu_r \mu_0 \left(H_i H_j^* - 1/2\, \delta_{ij} |H|^2\right)\right] \qquad (6.1.1)$$

where E and H are the total electric and magnetic fields (obtained from 3D finite element Maxwell solver simulations in COMSOL Multiphysics), δ_{ij} is Kronecker's delta, ε_0 (μ_0) is the vacuum permittivity (permeability) and ε_r (μ_r) is their relative counterpart, and Re stands for the real part. The element ij of the Maxwell stress tensor has units of momentum per unit of area per unit time and gives the flux of momentum parallel to the ith axis crossing a surface normal to the jth axis (in the negative direction) per unit of time [134, 154]. The stress tensor integral equation encompasses both the radiation pressure and the near-field gradient force, while not including Casimir forces derived from vacuum quantum fluctuations (which exist even in the absence of illumination).

To enhance out-of-plane forces, one possible method is to take advantage of high-quality factor Fano resonances [155] or bound states in the continuum (BIC) [156] in Mie-scattering. The inset of Figure 6.1b shows dimensional schematics of the BIC dielectric optomechanical metamaterial, manifesting such an effect. The periodicity of the square unit cell is 900 nm. The widths of the two 150 nm thick silicon bricks separated by a 150 nm wide air gap are 200 nm and 250 nm, respectively, and they are supported by 50 nm thick silicon nitride (Si_3N_4) having refractive index of $n_{Si_3N_4}$ = 2.0.

Silicon is assumed to be lossless with a refractive index of n_{Si} = 3.48 in the near-infrared range being considered. Under x-polarized plane wave illumination normally incident in the z direction, this structure presents a sharp transmission Fano-resonance at a wavelength that depends on the length of the narrow nanobars (see Figure 6.1a). This is a result of the antiphase oscillation of displacement currents generated in the two bars. As can be seen from Figure 6.1b, relative optical radiation pressure is enhanced around tenfold compared with a perfect reflector at normal incidence, where radiation pressure is $2P/c$ at maximum. This enhancement is attributed to momentum transfer from photons stored in the high-quality factor cavity with unity reflection formed by the unit cell, while optical force cancellation happens at wavelengths where unity transmission happens.

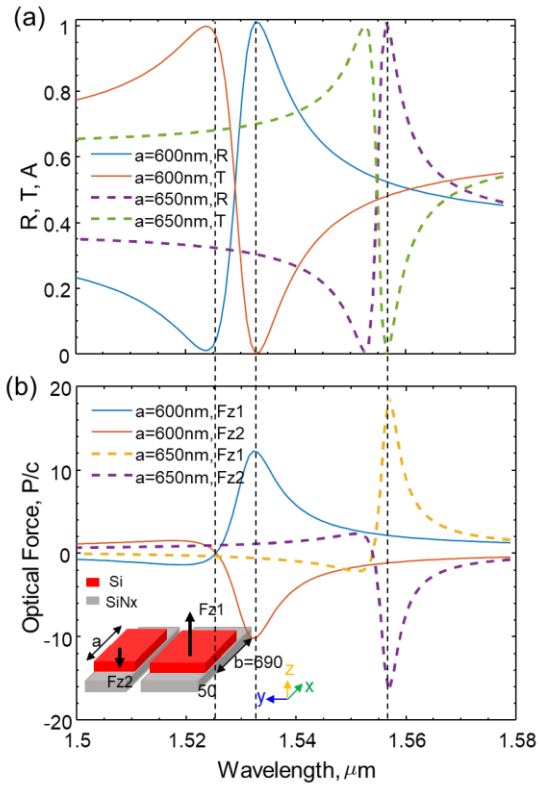

Figure 6.1 **Out-of-plane optical force enhancement in nano-optomechanical metamaterials.** (a) Numerically simulated reflection (R) and transmission (T) spectra of a metamaterial with unit cell comprising a pair of asymmetric silicon nanobars with different lengths for normally incident x-polarized light with narrow silicon nanobrick of length 600 nm and 650 nm, respectively, as shown in inset of (b). (b) Spectral dispersion of out-of-plane optical forces in z-direction on the constituent nanobars of the dielectric metamaterial. Optical force is presented in units of P/c, where P is the incident power per unit cell and c is the speed of light in vacuum.

In order to enhance in-plane optical forces within a metamaterial, one may enhance the fields, and thereby field gradients, within the plane of the structure. Figure 6.2a plots the numerically simulated optical spectra of a Mie-scattering based electromagnetic induced transparency (EIT) metasurface (unit cell dimensions detailed in the inset, Si and Si_3N_4 layers have thickness of 150 nm and 50 nm) in the lossless ($n_{Si} = 3.48$) and lossy cases ($n_{Si} = 3.48 + 0.01i$) for normally incident x-polarized light. The refractive index of silicon nitride (Si_3N_4) is $n_{Si_3N_4}$ = 2.0. A clear

transparency window in the transmission spectra is observed (Figure 6.2a), as the result of destructive interference between “bright” mode (excited electric dipole in the upper nanobars) and “dark” mode (excited magnetic dipole in the lower nanobars through energy exchange from upper nanobars). As can be seen in Figure 6.2b, in-plane attractive optical force enhanced approximately an order of magnitude as a result of the local field enhancement between the two component parts. However, as can be seen, optical force is loss dependent. The higher the absorption, the smaller is the optical force.

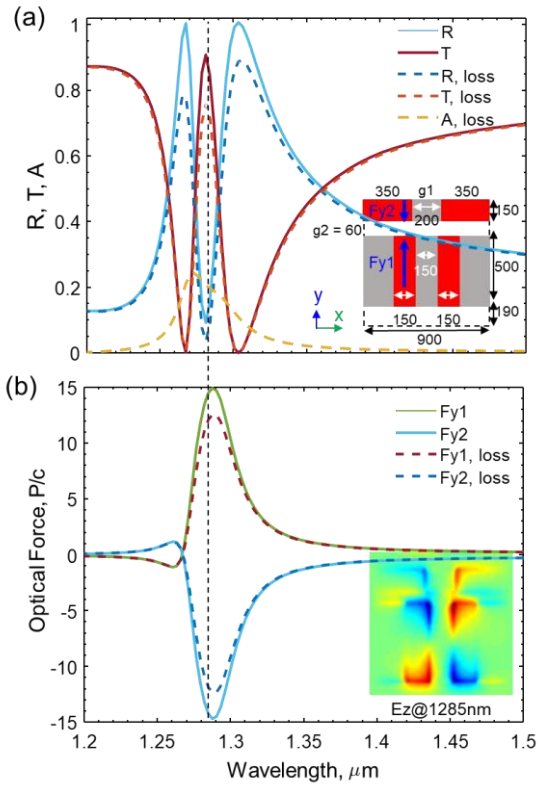

Figure 6.2 **In-plane optical force enhancement in nano-optomechanical metamaterials.** (a) Numerically simulated reflection (R), transmission (T) and absorption (A) spectra of a metamaterial with unit cell comprising nanobars arranged in Π shape for normally incident x-polarized light in lossless n_{Si} = 3.48 (solid lines) and lossy n_{Si} = 3.48 + 0.01i cases (dashed lines), respectively. Inset: Dimensional schematic view of a metamaterial unit cell. (b) Spectral dispersion of in-plane optical forces on the constituent nanobars of the dielectric metamaterial. Optical force is presented in units of P/c, where P is the incident power per unit cell and c is the speed of light in vacuum. The inset shows a map of the optically induced charge distributions at a wavelength of 1285 nm in terms of the instaneous electric field E_z that these changes generate normal to the metamaterial surface.

6.1.2 Photothermal tuning mechanism within nano-optomechanical metamaterial

Generally, in a nano-optomechanical system, heating of a mechanical beam, as a result of increasing light absorption, will result in a stress reduction due to thermal expansion. Optical heating changes the stress σ in a mechanical beam through the thermal expansion coefficient

$$\sigma = \sigma_o + \sigma_t = \sigma_o - \alpha Y \delta T \tag{6.1.2}$$

where σ_o is the initial stress at the initial temperature T_0, $\sigma_t = -\alpha Y \delta T$ is the temperature change δT related stress change, δT is the average temperature increase of the mechanical beam, Y is its Young's modulus, and α is its thermal expansion coefficient. According to Euler–Bernoulli beam theory, the resonant frequency $f(\sigma)$ of a pre-stressed doubly-clamped beam at its fundamental flexural mode is given by [58, 59, 157]

$$f(\sigma) = 1.03 \frac{h}{L^2} \sqrt{\frac{Y}{\rho}} \sqrt{1 + \frac{\sigma L^2}{3.4 Y h^2}} \tag{6.1.3}$$

where h is the thickness, L is the length, ρ is the density of the material, and σ is the tensile stress along the beam. Therefore, considering equation (6.1.3), frequency shift δf reads

$$\delta f = f(\sigma) - f(\sigma_o) = f_o \left(\sqrt{1 + \frac{\beta \sigma_t}{1 + \beta \sigma_0}} - 1 \right) \tag{6.1.4}$$

where

$$f_o = 1.03 \frac{h}{L^2} \sqrt{\frac{Y}{\rho}} \sqrt{1 + \beta \sigma_o} = f_1 \sqrt{1 + \beta \sigma_o} \tag{6.1.5}$$

being the initially stressed eigenfrequency without photothermal heating, f_1 is the stress free mechanical eignenfrequcy and β represents

$$\beta = \frac{L^2}{3.4 Y h^2} \tag{6.1.6}$$

The frequency shift δf in equation (6.1.4) can be approximated using Taylor series in the low temperature increase limit as

$$\delta f \sim \frac{f_o}{2} \frac{\beta \sigma_t}{1 + \beta \sigma_o} = -\frac{f_o}{2} \frac{\beta \alpha Y}{1 + \beta \sigma_o} \delta T \tag{6.1.7}$$

which decreases linearly with the increase of temperature change.

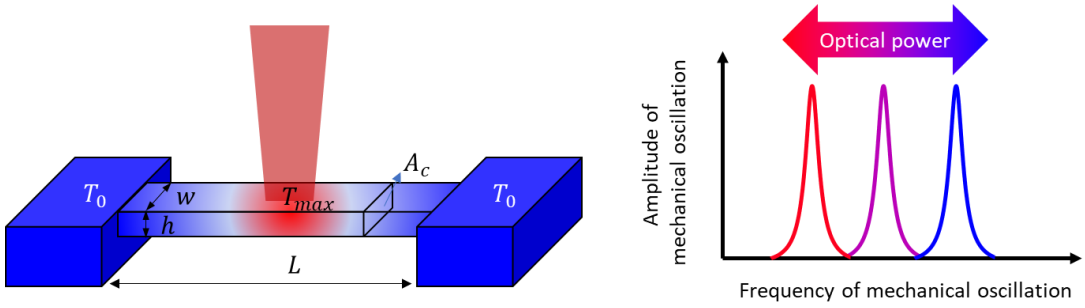

Figure 6.3 **Concept of photothermal tuning of mechanical eigenfrequencies**. Incident light heats a nanomechanical oscillator, causing a shift of its mechanical resonance frequency. Redshift of mechanical resonance frequency is observed by increasing laser power.

Assuming a mechanical beam of length L, illuminated at its central part (Figure 6.3), the energy absorbed per second, P_{abs}, in the centre is in equilibrium with the heat flow through the material out into the supports that have a constant temperature T_0. Following [59, 158], the temperature distribution is described as

$$T(x) = T_0 + 2(T_{max} - T_0)\frac{x}{L} \tag{6.1.8}$$

for $0 \leq x \leq \frac{L}{2}$, where T_{max} is the temperature at the centre. The heat flux, Q_T through one half of the structure can be described by the one-dimensional Fourier's law as

$$Q_T = -\kappa A_c \frac{\partial T}{\partial x} \tag{6.1.9}$$

where A_c is the mechanical beam's cross section and κ is the material's thermal conductivity. The total power absorbed in the beam must be equal to the total energy flowing from the centre to the supports

$$P_{abs} = 2|Q_T| \tag{6.1.10}$$

Combination with Equations (6.1.8) and (6.1.9) gives

$$\delta T_{max} = T_{max} - T_0 = \frac{P_{abs}L}{4\kappa A_c} \tag{6.1.11}$$

The average temperature increase of the structure becomes

$$\delta T = \frac{\delta T_{max}}{2} = \frac{P_{abs}L}{8\kappa A_c} \tag{6.1.12}$$

Hence, frequency shift δf

$$\delta f = -\frac{f_o}{2}\frac{\beta\alpha Y}{1+\beta\sigma_o}\delta T = -\frac{f_o}{2}\frac{\beta\alpha Y}{1+\beta\sigma_o}\frac{P_{abs}L}{8\kappa A_c} \tag{6.1.13}$$

is linearly proportional to laser power absorption P_{abs} when temperature increase is small.

6.2 Nano-optomechanical metamaterial for parametric oscillation experiments

Experiments described in the remaining sections of this chapter employ an all-dielectric nanomechanical metamaterial (Figure 6.4) fabricated on a silicon nitride membrane of nanoscale thickness [6, 33]. As shown in Figure 6.4a, it consists of a planar array of periodically arranged

optical resonators (with dimensional schematic of a unit cell or metamolecule is depicted in Figure 6.4b) supported by a 1D array of mechanical resonators, which are flexible nanowires of microscale length cut from the silicon-nitride membrane by focused ion beam (FIB) milling.

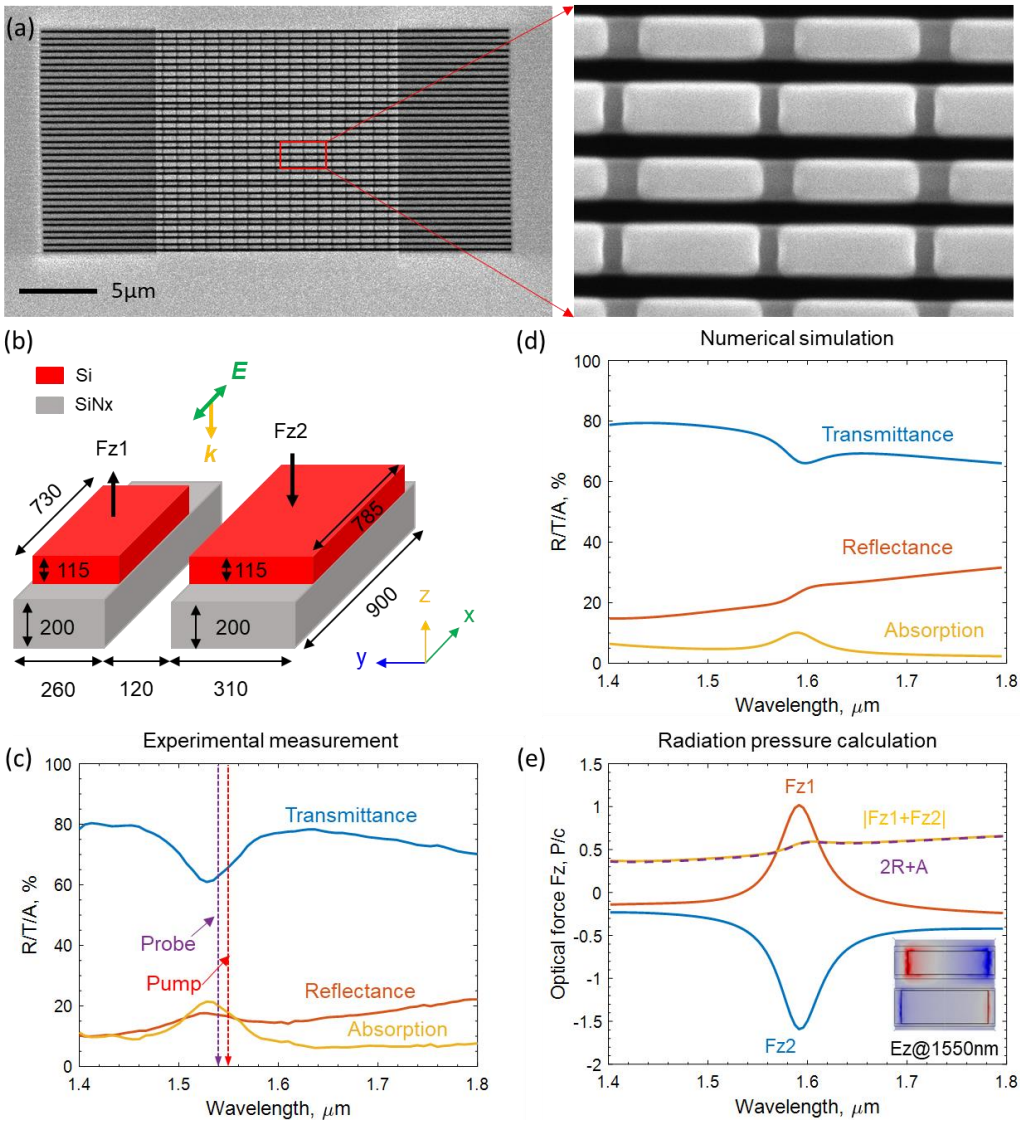

Figure 6.4 **Optical properties of dielectric nano-optomechanical metamaterials.** (a) SEM image of fabricated sample, black areas are cut through. (b) Dimensional schematic of a metamolecule. The periodicity along x and y direction are 900 and 820 nm. (c) The optical transmission, reflection and absorption spectra measured using CRAIC Spectrophotometers. Pump laser wavelength 1550 nm, Probe laser wavelength 1540 nm. (d) Simulated metamaterial optical spectra using COMSOL Multiphysics considering Si and Si_3N_4 with refractive index $n_{Si} = 3.48 + 0.1i$ and $n_{SiN} = 2.0 + 0.0i$. (e) Normal to the metamaterial component of optical forces $F_{z1,2}$ acting on the strip segments along the light propagation direction shown in a quantified through Maxwell stress tensor calculation [42]. The net optical force on the unit cell (yellow line) is presented alongside the value expected from reflection and absorption (dotted purple line). Forces are shown per unit cell in units of P/c, where P is the incident power per unit cell and c is the speed of light in vacuum. Inset shows map of the optically induced charge distributions at the pumping wavelength in terms of instaneous electric field E_z that these changes generate normal to the metamaterial surface.

The metamaterial was fabricated on a 200 nm thick silicon nitride membrane coated with a 115 nm layer of amorphous silicon (a-Si) by plasma-enhanced chemical vapor deposition (PECVD). This bilayer was then structured by FIB milling to define an array of asymmetric nanorod pairs in the

amorphous silicon layer, on 31 μm long silicon nitride beams. The structure supports a closed mode optical resonance [159] at a wavelength of 1530 nm as shown in Figure 6.4c, underpinned by the excitation of antiparallel displacement currents in the pair of amorphous silicon nanorods [160, 161]. In numerical simulation (as shown in Figure 6.4d-e), considering the experimentally measured optical spectra of the metamaterial sample, silicon refractive index is fitted to be $n_{Si} = 3.48 + 0.1i$. The relative optical force between the two constituting elements is calculated as ~3 P/c considering the loss of silicon material in the experimentally used sample, where P is the incident power per unit cell and c is the speed of light in vacuum.

As shown in Figure 6.5, numerical calculations show that the relative optical transmittance $\Delta\mu^t/\mu_0^t$ is generally a nonlinear function of the relative displacement between neighbouring beams along the z direction (here $\Delta\mu^t$ is the change of transmittance at a given displacement δz and μ_0^t is transmittance of the metamaterial without displacement), but may be approximately linear for sufficiently small displacements. This is illustrated by 3D finite element Maxwell solver simulations of the resonant optical properties of the array for different levels of mutual displacement between neighbouring beams (see Figure 6.5a). For instance, for displacements of up to 40 nm, transmittance changes approximately parabolically with displacement at 1550 nm (Figure 6.5b).

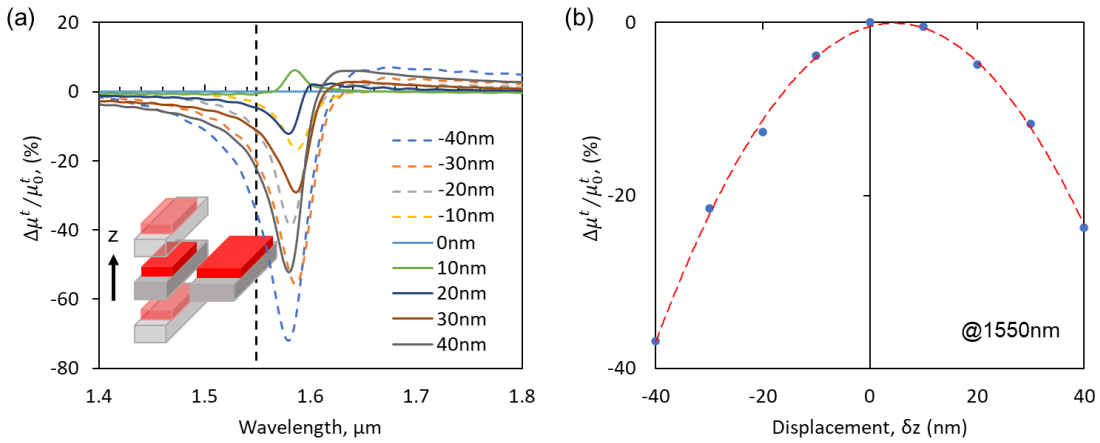

Figure 6.5 **Optical properties of the dielectric nanomechanical metamaterials.** (a) Computed values of ($\Delta\mu^t/\mu_0^t$), a figure of merit of responsivity of the metamaterial's optical properties to the relative displacement of neighbouring beams along z at different levels of displacement. (b) Dependence of ($\Delta\mu^t/\mu_0^t$) on displacement at wavelengths of 1550 nm. Positive displacement corresponds to the movement of narrower beams along +z relative to wider beams; all results are for x-polarized light.

6.3 Optical detection of thermal fluctuations in nano-optomechanical metamaterials

As has been discussed in previous chapters, nano-components such as beams and cantilevers can be modelled as damped mechanical oscillators [162-165]. Considering nanomechanical structures

located in the *xy*-plane, and engaged in out-of-plane thermal motion in the z direction throughout this chapter, the Langevin equation for the thermal motion of such a component can be written as [58]

$$\ddot{z} + \gamma_m \dot{z} + \omega_m^2 z = F_{thermal}(t)/m_{eff} = \sqrt{2\pi k_B T \gamma_m / m_{eff}}\, \eta(t) \tag{6.3.1}$$

where $F_{thermal}(t)$ is the Langevin thermal force experienced by the oscillator related to the dissipation factor γ_m through the fluctuation-dissipation theorem, $\eta(t)$ is a normalized white noise term, m_{eff} is the effective mass of the object, k_B is the Boltzmann constant, T is the temperature, $\omega_m = 2\pi f_m = \sqrt{(k/m_{eff})}$ is the natural angular frequency of oscillation, f_m is the natural frequency and k is the spring constant. The resonance quality factor $Q = \omega_m/\gamma_m$ in the limit of small damping, $\gamma_m \ll \omega_m$, which we assume here.

Thermomechanical fluctuations of a component's position $z(t)$ are transduced to fluctuations of intensity of light scattered on the component, $\delta I(t) = \frac{\partial \mu(z,\lambda)}{\partial z} \cdot I_0 \cdot \delta z(t)$, where I_0 and $I = \mu(z,\lambda) I_0$ are the intensities of the incident and scattered light, and $\mu(z,\lambda)$ is, generally, a nonlinear function of the component's displacement z and optical wavelength λ or frequency shown in Figure 6.5b. As, in a stochastic process, the power spectral density is equal to the Fourier transform of its autocorrelation function [85], the scattered light amplitude spectral density $S_I^{1/2}(f)$ resulting from small thermomechanical fluctuations in position $\delta z(t)$ is:

$$S_I^{1/2}(f) = \frac{\delta I}{\sqrt{\Delta f}} = \left(\left. \frac{\partial \mu(z,\lambda)}{\partial z} \right|_{z=0} \cdot I_0 \right) \times \sqrt{\frac{k_B T f_m}{2\pi^3 m_{eff} Q[(f_m^2 - f^2)^2 + (f f_m/Q)^2]}} \tag{6.3.2}$$

where Δf is the bandwidth. In an optomechanical metamaterial, a non-diffracting array of identical oscillating components, the same formula will describe the spectra of fluctuations of the intensity of light transmitted I^t through the metamaterial, see Figure 6.5.

Transmittance fluctuations over a range of mechanical frequencies can be calculated by integration over the power spectral density of the fluctuations

$$\begin{aligned} \delta I / I_0 &= \sqrt{\int \left(S_I^{1/2}(f) \right)^2 df} \\ &= \frac{1}{\mu_0^t(\lambda)} \times \left. \frac{\partial \mu^t(z,\lambda)}{\partial z} \right|_{z=0} \\ &\quad \times \sqrt{\frac{k_B T}{2\pi^3 m_{eff}}} \sqrt{\int \frac{f_m/Q}{(f_m^2 - f^2)^2 + (f f_m/Q)^2} df} \end{aligned} \tag{6.3.3}$$

Integration from 0 to ∞, or at least over the whole resonance, gives the root-mean-square (RMS) fluctuations

$$\delta I/I_0 = \frac{1}{\mu_0^t(\lambda)} \times \frac{\partial \mu^t(z,\lambda)}{\partial z}\bigg|_{z=0} \times \sqrt{\frac{k_B T}{4\pi^2 m_{eff} f_m^2}} \tag{6.3.4}$$

where the final term corresponds to the RMS beam displacement of

$$\delta z_{rms} = \sqrt{\frac{k_B T}{4\pi^2 m_{eff} f_m^2}} \tag{6.3.5}$$

Assuming metamaterial beams, such as those shown by Figure 6.4, with an effective mass m_{eff} = 2 pg and mechanical quality factor of Q = 2000 moving at a damped frequency f_1 = 2 MHz, and a typical change in optical properties with beam displacement of $\partial\mu/(\mu_0\partial z) \sim 1$ %/nm, one may expect to observe an RMS thermomechanical displacement amplitude of $\delta z_{rms} = 100$ pm at the centre of the beams at room temperature, resulting in a ~ 0.1% RMS fluctuations of optical properties. By applying this analytical description to experimental data collected by Dimitrios Papas and Jinxiang Li for, respectively, plasmonic and all-dielectric metasurfaces, we have shown that mechanical fluctuations of the constituent nanowires with amplitudes of a just a few hundred picometres lead to reflectivity/transmittance fluctuations on the order of 0.1% [117].

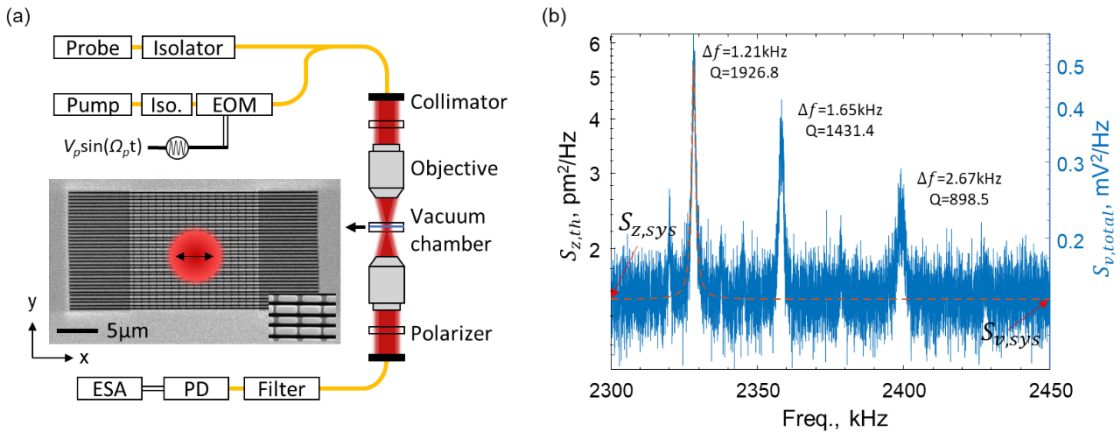

Figure 6.6 **Experimental setup for detection and control of thermal fluctuation in nanomechanical metamaterials.** (a) Schematic of the pump–probe measurement setup and a scanning electron micrograph of the metamaterial sample. Pump and probe laser beams are polarized along x-direction at wavelength of 1550 nm and 1540 nm with ~5 μm spot size in diameter. The pump and probe laser power on sample is ~40μW and ~20μW. Iso.: optical isolator, EOM: electro-optic-intensity modulator, PD: photodetector, ESA: electronic spectrum analyser. For thermal motion detection, pump laser is kept at a fixed laser power level without intensity modulation. [As will be described in section 6.4, for parametric control of thermal motion, pump laser is modulated by electro-optic-intensity modulator (EOM)]. (b) Calibrated displacement power spectral density of nanowires within dielectric metamaterials without pump laser modulation. Different peaks correspond to the thermal movement of different nanowires. Resonant peak widths δf are labelled in kHz.

Figure 6.6b shows a representative probe transmission spectrum for the all-dielectric metamaterial presented in Figure 6.4. As can be seen in Figure 6.6a, measurements were performed by

monitoring the *x*-polarized continuous-wave (CW) probe laser intensity transmitted through the sample while keeping pump laser at a fixed laser power level without intensity modulation. [Application of the intensity modulation of pump will be shown in the parametric control of thermal motion experiment in section 6.4.] The pump and probe optical sources used are fiber-coupled telecommunication semiconductor lasers operating at the wavelengths of 1550 and 1540 nm, respectively. The pump and probe were then combined into a single beam using a fiber coupler, decoupled into free space and focused on the sample placed in a microscope using focusing and collection objectives a confocal pair of 20× (NA=0.4) microscope objectives. The pump and probe laser power on the sample is ~40μW and ~20μW with spot size ~ 5μm in diameter corresponding to laser intensity of ~2μW/μm^2 and ~1μW/μm^2. The metamaterial sample was mounted in a vacuum chamber at a pressure of 4-5 μbar to reduce air damping of the mechanical modes. The intensity of probe light transmitted from the samples was monitored with a photodetector and a radio frequency spectrum analyser.

Displacement is then calibrated using the following procedure: Assuming the noise processes are uncorrelated, the total noise power spectral density (PSD) $S_{v,total}$ is the sum of the PSDs from individual noise processes. Thus, we have $S_{v,total} = S_{v,th} + S_{v,sys}$. Here $S_{v,th}$ is the thermomechanical motion power spectral density $S_{z,th}$ translated into the electronic domain, through the 'displacement-to-voltage' responsivity $\Re \equiv S_{v,th}^{1/2}/S_{z,th}^{1/2}$. The other term $S_{v,sys}$ is the voltage noise floor of the measurement system. Measured data can be fitted to the expression for $S_{v,total}$ by using $S_{v,th} \equiv \Re^2 \times S_{z,th}$ and treating $S_{v,sys}$ as a frequency-independent function within the smaller measured range:

$$\begin{aligned} S_{v,total}(f) &= \Re^2 \times S_{z,th} + S_{v,sys} \\ &= \Re^2 \frac{k_B T f_m}{2\pi^3 m_{eff} Q[(f_m^2 - f^2)^2 + (f f_m/Q)^2]} + S_{v,sys} \end{aligned} \tag{6.3.6}$$

Using effective mass of m_{eff} = 2.7 pg as calculated from COMSOL simulation for the narrow beam with known geometry and material parameter and from the fitting the first peak (assuming T = 300K), we obtain $S_{v,th}^{1/2}$ = 0.4 mV/Hz$^{1/2}$, Q = 1927, and $\Re$ = 0.308mV/nm. As seen in Figure 6.6b, this fitting returns a noise equivalent power spectral density of $S_{z,sys}$~1.53pm^2/Hz.

Several peaks are seen in the frequency spectrum (Figure 6.6b), each corresponding to an individual nanowire. Here, the main cause of variations between the resonance frequencies of individual, nominally identical beams is most likely disparities in beam tension across the sample resulting from the non-uniformity of intrinsic stress in the membrane, rather than variations of their physical dimensions. These variations in tensile stress across the metamaterials can be evaluated from Equation (6.1.5). The observed range of frequencies (from 2.3 to 2.5 MHz) is consistent with an

initial tensile stress of σ_o ~25 MPa and variations from beam to beam of ~10 MPa (using a numerically calculated stress-free eigenfrequency f_1 = 1.96 MHz for the supporting silicon nitride beam). These numbers are in keeping with the fact that stresses of between several hundred megapascals and a gigapascal are common in unstructured silicon nitride membranes [166], resulting in significant post FIB-fabrication stress variations across metamaterial arrays.

6.4 Parametric control of thermal motion in a nano-optomechanical metamaterial

The dynamic photothermal tuning mechanism as described in section 6.1.2 is exploited to periodically modulate the mechanical resonance frequency of nanowires in thermal (Brownian) motion driven by a white noise. Thus, this creates an array of Brownian parametric oscillators with time-varying spring constant. As schematically shown in Figure 6.7, light modulated at an angular frequency of ω_p functions as a parametric pump which converts the thermomechanical vibrations of the nanowire at frequency ω_m into multiple thermal vibration Stokes' or anti-Stokes' sidebands at angular frequencies $\omega = \omega_m \pm N\omega_p$ (where N is an integer) via nonlinear optomechanical interaction of frequency mixing.

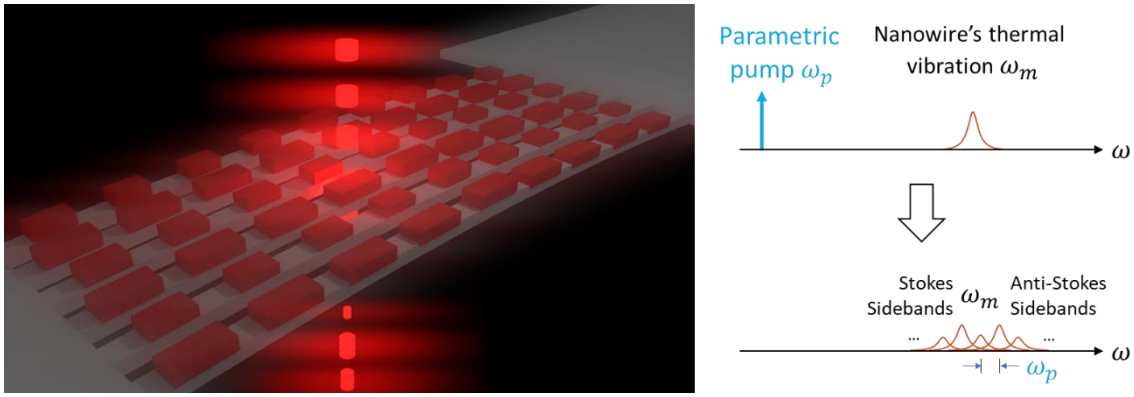

Figure 6.7 **Artistic impression of optical parametric control of thermomechanical vibration in an array of nano-optomechanical oscillators.** The modulated light at angular frequency of ω_p functions as a parametric pump which converts the thermomechanical spectrum at frequency ω_m into a series of thermal vibration sidebands centered at $\omega = \omega_m \pm N\omega_p$ via frequency mixing. It creates Stokes' and anti-Stokes sidebands whose amplitudes can be externally controlled by the parametric pump frequency and amplitude.

6.4.1 Optical parametric control of thermal motion

In this work, parametric control over thermal motion is demonstrated for a pair of dissimilar nanowires in the metamaterial array – those with resonant frequencies indicated in Figure 6.6b at ω_{m1} = 2π×2328.3 kHz ($\gamma_{m1} = 2\pi\delta f_1$= 2π×1.21 kHz, Q_1 = 1926.8) and ω_{m2} = 2π×2358.2 kHz (γ_{m2} = 2π×1.65 kHz, Q_2 = 1431.5) for two narrow nanowires. Experimental setup is schematically shown in Figure 6.6a.

In this experiment, the probe laser is at a wavelength of 1540 nm which is continuous-wave (CW). The probe laser power incident on the sample is P_{in} ~ 20μW corresponding to laser intensity of I_0 ~ 1μW/μm^2 considering the laser spot of diameter ~5 μm. The pump laser is at a wavelength of 1550 nm. The intensity of the pump laser beam was modulated by a fibre-coupled electro-optical modulator (EOM) with an averaged power incident on the sample of P_{in} ~ 40μW, corresponding to laser intensity of I_0 ~ 2μW/μm^2 considering the laser spot of diameter ~5 μm. As shown in Figure 6.8, the modulation depth of pump laser beam is defined as the ratio of power modulation amplitude P_{amp} and its average power P_{avg}, and is controlled by the applied peak-to-peak voltage V_p to the EOM. The pump modulation depth increases with the increasing peak-to-peak voltage V_p at a rate of 25%/Vpp, while its average power does not change.

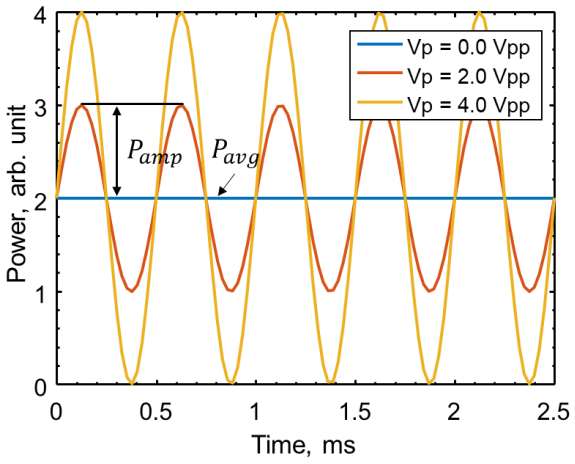

Figure 6.8 **Laser power modulation as a function of applied peak-to-peak voltage on electro-optic intensity modulator.** The power modulation depth, defined as the ratio of power modulation amplitude P_{amp} and its average P_{avg}, is 25%/Vpp.

The pump and probe were coupled into a single fibre and then focused onto the sample via a collimator and 20× (NA=0.4) microscope objective. Transmitted light was collected via a matched and axially-aligned objective, collimator and fibre on the opposite side of the sample chamber. Only probe light passes through the filter and was monitored with a photodetector and a radio frequency spectrum analyser.

Figure 6.9a displays the evolution of probe transmission spectra that are calibrated into thermochemical displacement power spectral density (see section 6.3) with increasing pump modulation depth while keeping the pump modulation frequency fixed at ω_p = 2π×2 kHz. One can see that with increasing pump modulation depth, first, creation of a series of sidebands located at frequencies $\omega_m \pm N\omega_p$ in the spectra; second, strong oscillations in the amplitudes of the peaks: for example, as shown in Figure 6.9a, for the mechanical mode ω_{m1}, the experimental spectra exhibit a nearly complete extinction of the initial state occupation at 2.0 Vpp and its reappearance at 3.0 Vpp. The oscillation in the amplitude of the first order sidebands can also be easily found. Therefore, total number and amplitudes of sidebands can be controlled by appropriately choosing

the external parametric pumping parameters. Furthermore, the spectra evolve differently for two nanowires of different damping rates.

The underlying dynamics of these behaviours can be described by the Brownian parametric oscillator equation [96] as presented in section 2.4 and repeated as:

$$\ddot{z}(t) + \gamma_m \dot{z}(t) + \left[\omega_m^2 + 2\varepsilon\omega_m \cos(\omega_p t)\right] z(t) = F_{thermal}(t)/m_{eff} \qquad (6.4.1)$$

where $z(t)$ is the real time thermal vibration of a nanowire along z-direction (Figure 6.5) at angular frequency ω_m with effective mass of m_{eff} driven by thermal Langevin force $F_{thermal}(t)$, γ_m is the mechanical dissipation factor and ω_p is the parametric pumping angular frequency. The optical parametric pumping pulse creates a time varying spring constant $k(t) = m_{eff}\left[\omega_m^2 + 2\varepsilon\omega_m \cos(\omega_p t)\right]$ via photothermal tuning mechanism as discussed in section 6.1.2, where ε is the parametric pumping strength reflecting the maximum mechanical resonant angular frequency shift of the nanowire ($\delta\omega = \sqrt{\omega_m^2 + 2\varepsilon\omega_m} - \omega_m \sim \varepsilon$). It is related to absorbed light power and therefore proportional to the pump modulation depth. Essentially, the optomechanical interaction studied here constitutes an optical phase-modulation of the nanowires' mechanical vibration.

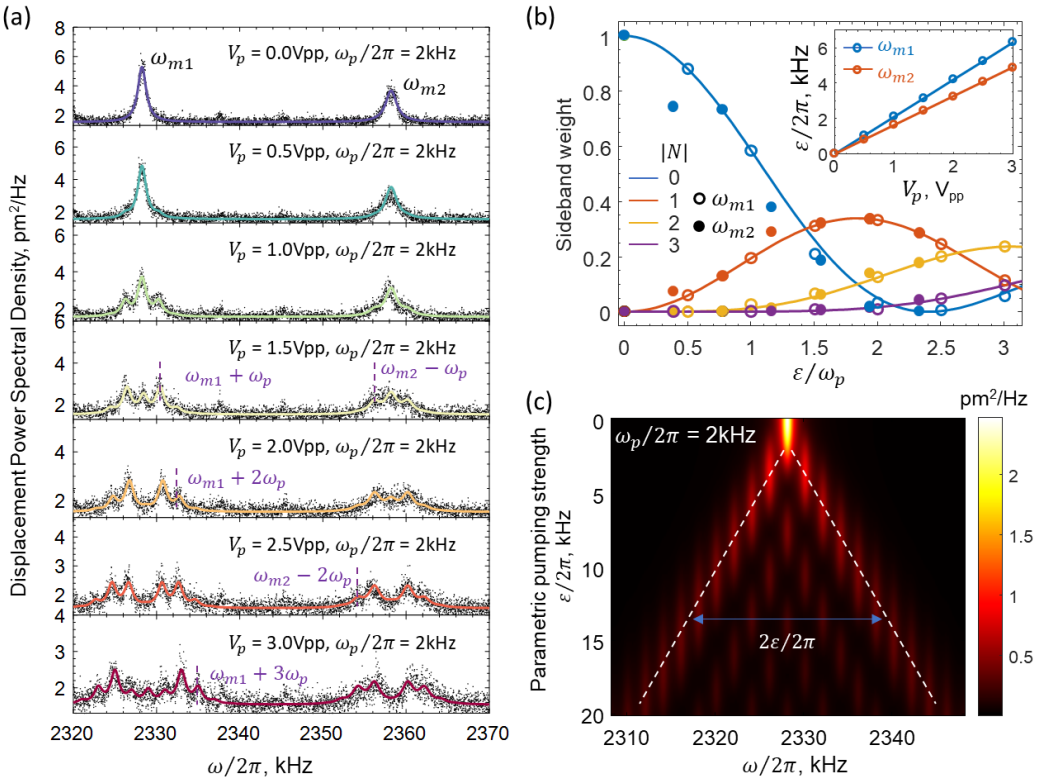

Figure 6.9 **Evolution of thermomechanical power spectral density as a function of parametric pumping strength.** (a) Evolution of the probe transmission spectra [calibrated into displacement power spectral density] with increasing pump laser intensity modulation depth (25%/Vpp). (b) Amplitudes (open or solid circles for mechanical mode 1 or 2) of the N_{th}-order spectral sidebands shown in (a). Solid lines, square of the N_{th}-order Bessel functions of the first kind. (c) Analytical evolution of Brownian power spectral density as a function of the parametric pumping strength with dashed lines indicate cut-off frequency which is proportional to parametric pumping strength ε.

The parametrically driven thermomechanical displacement power spectral density (PSD) obtained from Eqn. (6.4.1) as described in section 2.4 is

$$\Gamma(\omega) = \sum_{-\infty}^{\infty} J_N^2\left(\varepsilon/\omega_p\right)\Gamma_0\left(\omega_m + N\omega_p\right) \tag{6.4.2}$$

Here, $\Gamma_0(\omega_m) = 4\gamma_m k_B T/\{m_{eff}[(\omega_m^2 - \omega^2)^2 + \gamma_m^2\omega^2]\}$ is the initial thermomechanical displacement power spectral density (PSD) without parametric pumping. J_N represents the Nth order Bessel function of the first kind.

A good agreement is found between experimentally measured thermomechanical displacement power spectral density (as shown by the black dotted curves in Figure 6.9a) and analytical fitting results (as shown by solid lines in Figure 6.9a) using Eqn. (6.4.2) for two different nanowires and including the system noise level of 2pm^2/Hz.

The retrieved weights for the N_{th} sideband from this fitting are plotted by circles in Figure 6.9b for each curve plotted in Figure 6.9a, and they follow closely with analytical values $J_N^2\left(\varepsilon/\omega_p\right)$ from analytical model (solid line in Figure 6.9b) with the parametric pumping strength ε obtained from this fitting is plotted in inset of Figure 6.9b. As expected, the induced parametric pumping strength ε grows linearly with the pump modulation depth.

To reveal the evolution of thermomechanical displacement power spectral density with the increasing parametric pumping strength more clearly, analytical mapping of thermomechanical displacement power spectral density for the first mechanical mode is illustrated in Figure 6.9c. With increasing parametric pumping strength, one can see a linear spreading in the range of sidebands with cut-off frequency proportional to parametric pumping strength ε (see dashed white lines), together with strong oscillations in their amplitudes. Therefore, parametric pumping creates new Stokes' and anti-Stokes' sidebands each weighted by the Bessel function $J_N^2\left(\varepsilon/\omega_p\right)$, evolving as a function of parametric pumping strength ε.

Figure 6.10a shows the evolution of the measured probe transmission spectra that are calibrated into thermochemical displacement power spectral density with varied parametric driving frequency ω_p. This allows one to reach larger ratio of ε/ω_p while keeping the pump laser modulation depth fixed at 50%. One can see that with decreasing parametric pumping frequency (from bottom panel to top panel) the spectra are broadening and more sidebands are covered within, however, their amplitudes are decreasing as a result of energy conservation. The fitted analytical thermomechanical displacement power spectral density (as shown by solid lines) using Eqn. (6.4.2) again overlaps very well with the experimentally measured ones (as shown by black dotted curves).

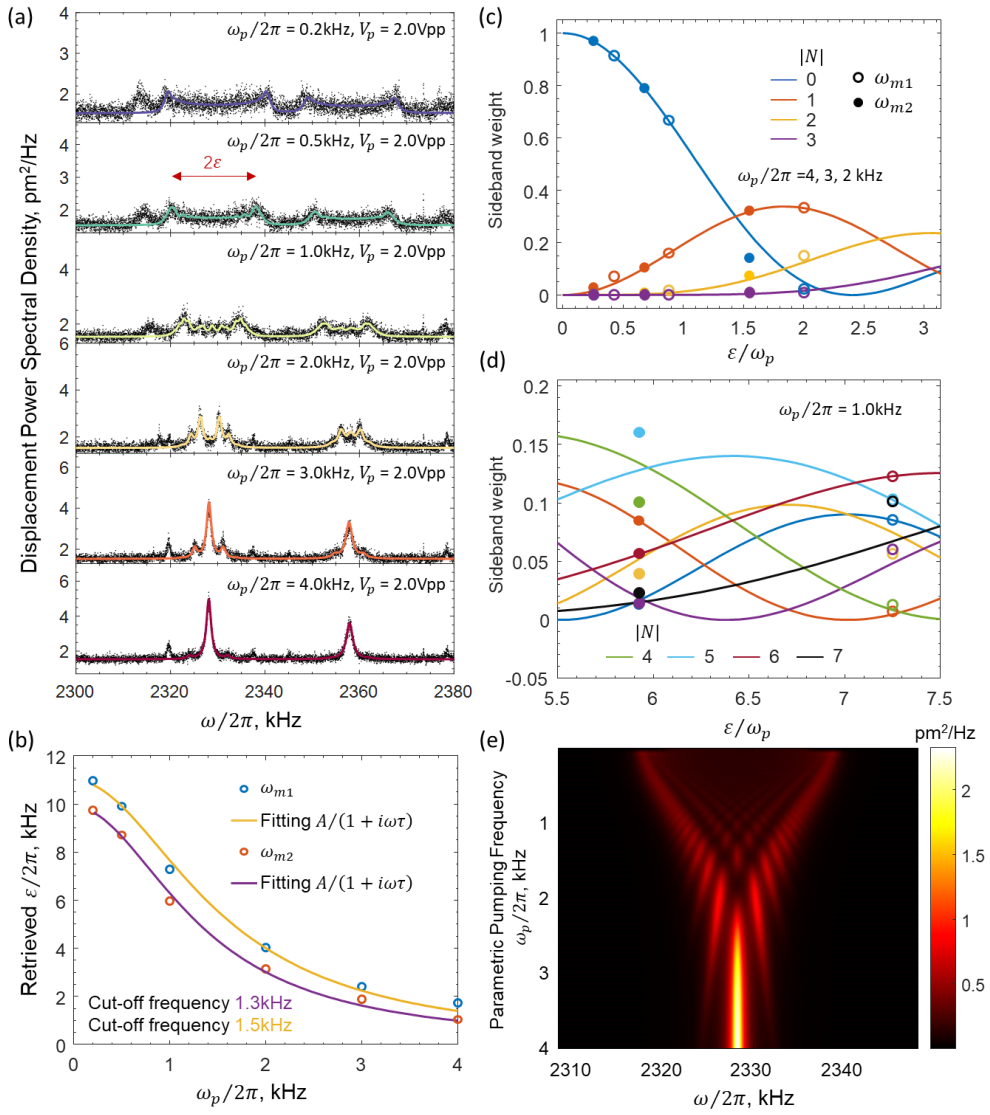

Figure 6.10 **Evolution of thermomechanical spectrum as a function parametric pumping frequency.** (a) Evolution of the probe transmission spectra [calibrated into displacement power spectral density] with growing parametric pumping frequency. (b) Experimentally retrieved parametric pumping strength as a function of applied frequency while keeping laser modulation depth fixed at 50%. The fittings of frequency response show the typical behaviour of a first-order low pass filter with cut-off frequency of 1.5 and 1.3 kHz and static pumping strength of 2π×11kHz and 2π×10 kHz. (c) Amplitudes (open or solid circles for mechanical mode 1 or 2) of the N_{th}-order spectral sidebands shown in (a) for frequency $\omega_p/2\pi$ = 4, 3, 2 kHz and (d) $\omega_p/2\pi$ = 1kHz. Solid lines, square of the N_{th}-order Bessel functions of the first kind. (e) Analytical evolution of Brownian power spectral density as a function of parametric pumping frequency with parametric pumping strength obtained from (b).

Parametric pumping strength ε (resulting from photothermal effect) is obtained from Figure 6.10a as a function of pumping frequency and plotted by circles in Figure 6.10b. The frequency response shows the typical behavior of a first-order low pass filter [167] with a cutoff frequency of 1.5 and 1.3 kHz and static pumping strength of 2π×11kHz and 2π×10 kHz for two mechanical modes when the illuminated laser power intensity is I_0 ~2 μW/μm². This overall agrees with that of the simulation result for dynamic photothermal response which suggests thermal relaxation frequency of the nanowire is ~8 kHz. Hence, the reported parametric control of the Brownian motion

mechanism can also enable photothermal dynamic response characterisation for a nanomechanical element.

Comparing the retrieved sideband weights with the analytical results for pumping frequencies $\omega_p/2\pi$ = 4, 3, 2 kHz (see Figure 6.10c), a good agreement is also found. However, the deviation is found in Figure 6.10d for the second mechanical mode ω_{m2} at parametric pumping frequency ω_p = 2π×1 kHz, this is due to the system noise where features such as peaks in the spectrum are buried in the noise and sideband weights are hard to retrieve.

Figure 6.10e shows the analytical evolution of Brownian power spectral density as a function of the parametric pumping frequency using parametric pumping strength obtained from Figure 6.10b for the first mechanical mode ω_{m1}. One can see more sidebands are generated for lower parametric pumping frequency and an interesting 'interference pattern' in frequency space can be observed.

6.4.2 Phononic frequency comb generation

The parametric control of Brownian motion demonstrated above suggests that certain frequency components of movement may be enhanced, as compared to the static/undriven case, when the resonance condition $\omega = \omega_m \pm N\omega_p$ is fulfilled, providing parametric gain defined as $\mathrm{G}(\omega) = \Gamma(\omega)/\Gamma_0(\omega)$. Unlike mechanical frequency combs that have been theoretically proposed using Fermi–Pasta–Ulam–Tsingou chains [152, 168], and later demonstrated in micromechanical resonators using nonlinear three-wave mixing [152, 169-171], here I present a tunable phononic frequency comb generation mechanism combining parametric pumping at frequency ω_p and a pondermotive light driving force at frequency ω_d near the mechanical resonance. This is experimentally achieved by modulating the pump laser intensity at the said two different frequencies. This regime can be mathematically described by adding the pondermotive light driving force term $F_d \cos(\omega_d t)$ on the righthand side of the Brownian parametric oscillator equation (6.4.1).

$$\ddot{z}(t) + \gamma_m \dot{z}(t) + \left[\omega_m^2 + 2\varepsilon\omega_m \cos\left(\omega_p t\right)\right] z(t) = F_{thermal}(t)/m_{eff} + F_d \cos(\omega_d t) \tag{6.4.3}$$

This force, coming from dipole-dipole interactions between neighboring optical resonators in the metamaterial (which has an estimated magnitude of ~25 fN in the present experimental configuration), induces several peaks in the transmission spectra at frequencies $\omega_d \pm N\omega_p$ (see Figure 6.11) via frequency mixing.

The signal at the optical driving frequency ω_d in Figure 6.11a increases with the growing parametric pumping strength ε as a result of parametric gain at this frequency (as ω_d coincides with

parametric sidebands of increasing amplitude). Also, a series of teeth appear at frequencies $\omega_d \pm N\omega_p$. By controlling the parametric pumping frequency ω_p, thereby the parametric gain spectrum, tunable frequency combs with different frequency separations can be generated (Figure 6.11b).

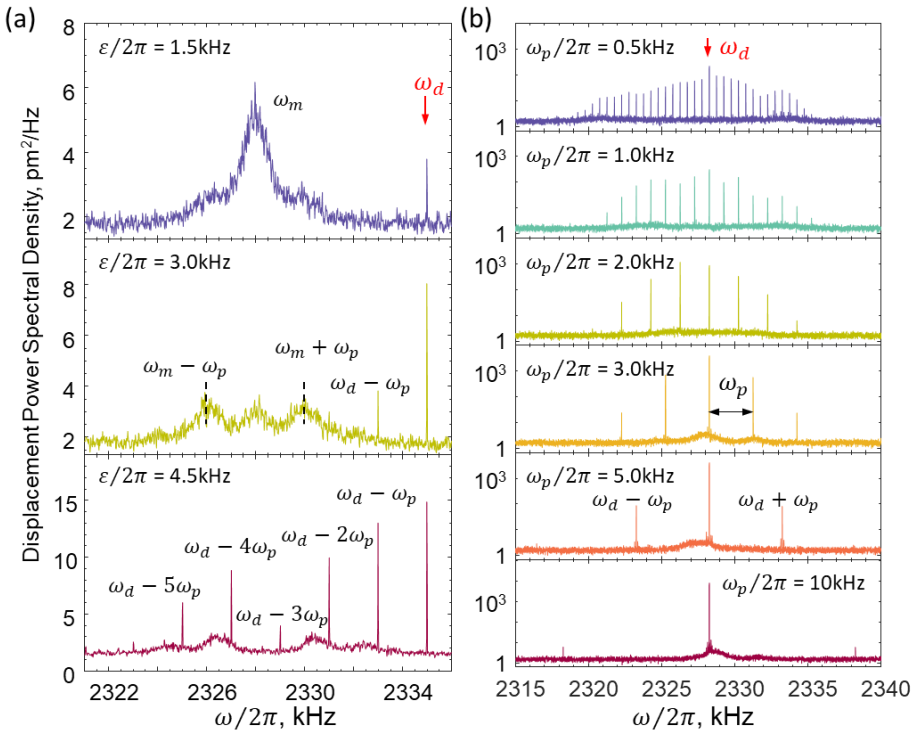

Figure 6.11 **Formation of a phononic frequency comb.** (a) Thermomechanical displacement power spectral density evolution as a function of growing parametric pumping strength ε while keeping its frequency fixed at $\omega_p/2\pi$ = 2kHz. The instantaneous optical force driving is fixed at frequency ω_d = 2335 kHz with laser intensity modulation depth of 25%. The instantaneous light driving force induces several coherent oscillations at a multiple frequency $\omega_d \pm N\omega_p$. (b) A tunable frequency comb generated by tuning parametric pumping frequency ω_p or comb separation while keeping the instantaneous optical force driving fixed at mechanical resonance frequency $\omega_{m1}/2\pi$ = 2328.5 kHz with laser intensity modulation depth of 25%.

6.5 Parametrically coupled optomechanical resonators

Dynamic coupling between two optomechanically connected doubly-clamped beams driven by thermal fluctuational forces is realized by parametrically pumping them at the difference frequency between their mechanical resonances. This enables strong vibrational coupling in systems where energy exchange between the two resonators is intrinsically inefficient owing to the frequency mismatch. The dynamics of such a system can be described by the following pair of coupled parametric Brownian oscillator equations:

$$\begin{aligned} &\ddot{z}_1(t) + \gamma_{m1}\dot{z}_1(t) + \left[\omega_{m1}^2 + 2\varepsilon_1\omega_{m1}\cos(\omega_p t)\right]z_1(t) + \Lambda\cos(\omega_p t)\, z_2(t) \\ &\qquad = F_{thermal}(t)/m_{eff1} \\ &\ddot{z}_2(t) + \gamma_{m2}\dot{z}_2(t) + \left[\omega_{m2}^2 + 2\varepsilon_2\omega_{m2}\cos(\omega_p t)\right]z_2(t) + \Lambda\cos(\omega_p t)\, z_1(t) \\ &\qquad = F_{thermal}(t)/m_{eff2} \end{aligned} \tag{6.5.1}$$

where z_1, z_2 are real time positions of the nanowires, γ_{m1}, γ_{m2} are their mechanical dissipation factors, ω_{m1}, ω_{m2} their mechanical resonance angular frequencies, ε_1, ε_2 the parametric pumping strengths for the two oscillators, and m_{eff1}, m_{eff2} are their effective masses. ω_p is the parametric pumping frequency. Λ is the coupling rate between two mechanical oscillators, and $F_{thermal}$ is the thermal Langevin force.

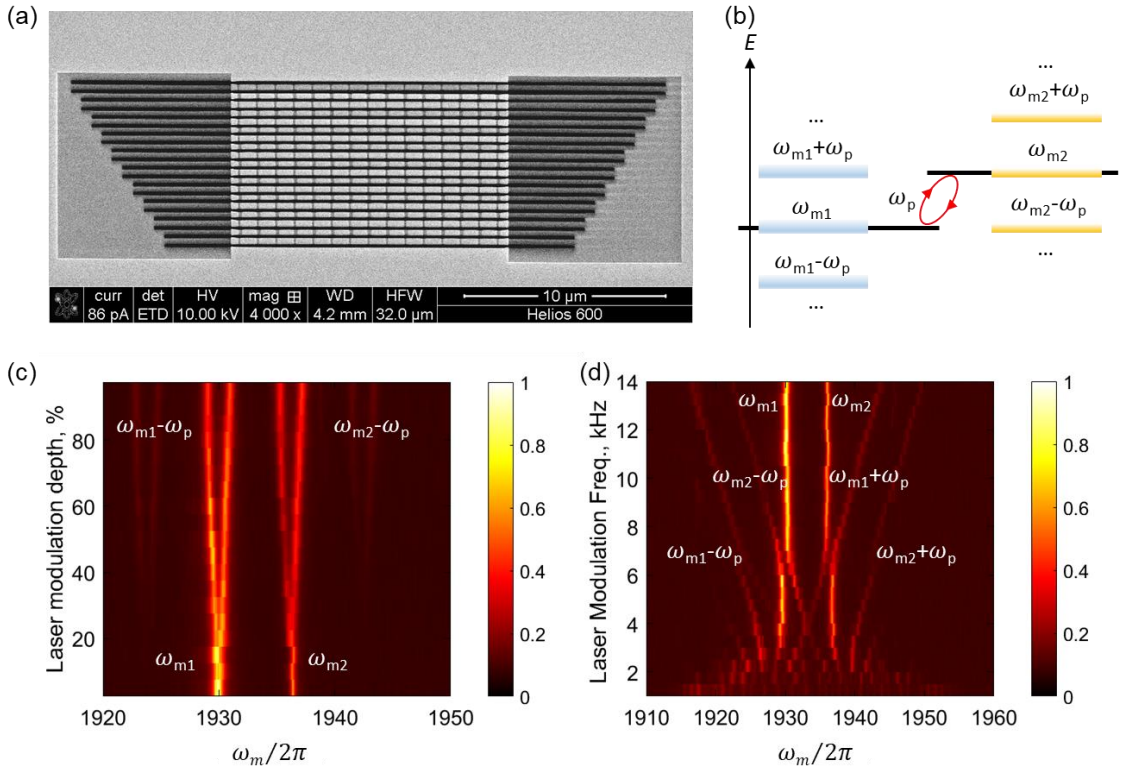

Figure 6.12 **Dynamic coupling between two distinct optomechanical beams.** (a) SEM images of planar dielectric metamaterials supported by Si_3N_4 beams of varied lengths fabricated on silicon nitride membranes. (b) Energy or spectrum diagram of the coupling between two thermomechanical oscillators with parametric pumping protocol. Blue bars denote the thermomechanical spectrum the mechanical oscillator with resonance frequency ω_{m1}, yellow bar represent the thermomechanical spectrum of the mechanical oscillator with resonance frequency ω_{m2}, when parametric pumping frequency satisfies $\omega_p = \omega_{m2} - \omega_{m1}$, energy transfer between two thermomechanical oscillators starts and is indicated by the red arrows. (c) Thermomechanical spectrum evolves with increasing parametric pumping strength at fixed parametric pumping frequency $\omega_p \cong \omega_{m2} - \omega_{m1}$ = 2π×6 kHz. (d) Spectra evolution with increased parametric pumping frequency ω_p while keeping the laser modulation depth fixed at 62.5%.

This experiment employed a different metamaterial sample comprised of silicon nitride beams of varying length, as shown in Figure 6.12a, whereby neighbouring beams can be readily identified in the frequency spectra of transmission. Figure 6.12b shows the energy diagram of the phonon transfer process for two frequency mismatched thermomechanical oscillators that are coupled to each other through a parametric pumping frequency ω_p. When parametric pumping frequency satisfies $\omega_p = \omega_{m2} - \omega_{m1}$, energy transfer between two thermomechanical oscillators starts as indicated by the red arrows. Figure 6.12c shows the experimental evolution of the thermomechanical modes of two neighbouring nanowires with natural resonant frequencies ω_{m1}= 2π×1930 kHz and ω_{m2}=2π×1936 kHz, as a function of the coupling strength Λ, which is proportional

to the laser modulation depth, while keeping the parametric pumping frequency fixed at $\omega_p \cong \omega_{m2} - \omega_{m1}$ ~ 2π×6 kHz. Mode splitting is clearly seen with increasing coupling strength indicating the strong coupling between two oscillators. The separation between the split peaks provides the coupling rate which can become so large that it can exceed the intrinsic energy dissipation rate of the two modes. Also, sidebands appear which replicate the dispersion of the ω_{m1} and ω_{m2} modes at lower and higher frequencies $\omega_{m1} - \omega_p$ and $\omega_{m2} + \omega_p$, as a result of frequency mixing. Figure 6.12d shows the evolution of the spectra with fixed coupling strength while sweeping the parametric pumping frequency ω_p from 2π×1 kHz to 2π×14 kHz. Here one can see that when ω_p approaches the difference frequency $\omega_{m2} - \omega_{m1}$ (i.e., 2π×6 kHz) of the two oscillators, splitting of spectral peaks occurs, indicating strong optomechanical coupling. A similar effect is seen when pumping at half of the difference frequency $\omega_p = (\omega_{m2} - \omega_{m1})/2$ ~ 2π×3kHz.

6.6 Summary

In this chapter I studied optomechanical interactions within nano-optomechanical metamaterials and the dependence of mechanical resonances of metamaterial beams on illumination by light. The ability to control mechanical resonances with light can be exploited for tuning of metamaterial functionalities. It is shown that frequencies of natural mechanical resonances of nano-optomechanical metamaterials can be continuously tuned by light induced heating affecting mechanical tension in the nanostructure.

I have demonstrated optical detection and parametric control of a picometric Brownian motion of the individual mechanical oscillators within a metamaterial array, and of two optomechanically coupled oscillators. This optical parametric control protocol allows continuous mechanical frequency conversion utilizing nonlinear optomechanical interaction (i.e. frequency mixing) at lower intensity level. This frequency mixing effect provides a new mechanism for phononic frequency comb generation in nano-optomechanical metamaterials by combining parametric control of mechanical oscillators with a periodic optical driving force. Finally, energy transfer between two thermomechanically oscillating nanowires via parametric coupling has been demonstrated in nano-optomechanical metamaterial.

Chapter 7 Conclusions

7.1 Summary

This thesis has been dedicated to several experimental efforts towards visualizing, interrogating and controlling the atomic length scale (fast) dynamics of thermal and driven motion in photonic nanostructures leveraging secondary electrons, light and optomechanical interactions. They open an exciting field of picophotonics, the emerging science of light and its interactions with matter at picometre [(sub-)atomic] scale.

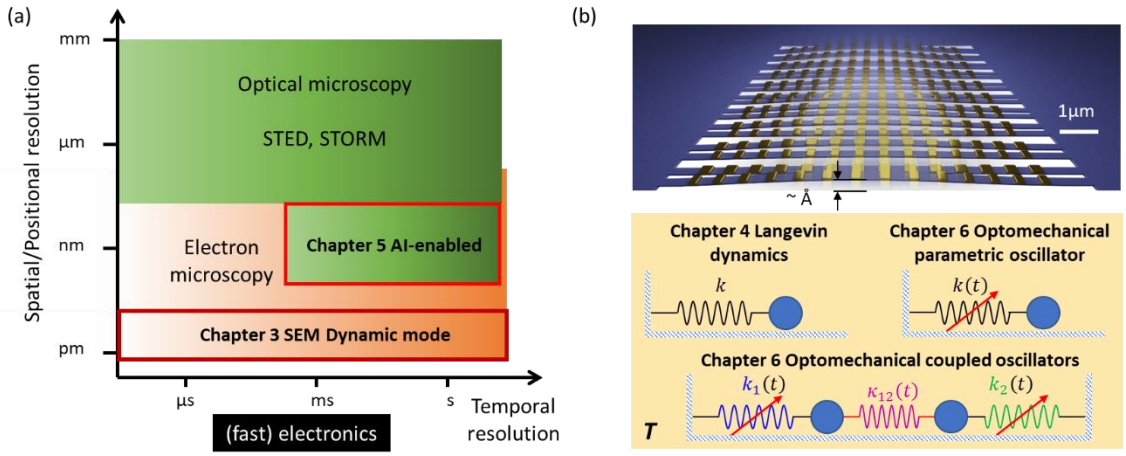

Figure 7.1 **Atomic scale thermal movement visualization and control in nanostructures.** (a) Important tools developed in this thesis in comparison with the routinely available electron and optical tools in terms of spatial/positional and temporal resolution (based on fast electronics instead of ultrafast pump-probe technique). (b) Based on the nano-optomechanical metamaterial platform, oscillatory thermodynamics at the atomic length scale are studied for a single oscillator with a fixed spring constant at short-time scale, a parametric oscillator with time varying spring constant, and two different parametrically coupled oscillators that are coupled into a heat bath T.

From a technological metrology perspective:

1. In Chapter 3, I have demonstrated a novel hyperspectral motion visualization technique built around a conventional scanning electron microscope via free electron edge-scattering to locally interrogate the thermomechanical movement. This extends a conventional scanning electron microscope to the dynamic mode regime with nanometre (nm) spatial resolution, microsecond (µs) temporal resolution and picometric (pm/Hz$^{1/2}$) electron-shot noise limited displacement sensitivity. This is essential for studying fast dynamics in nanomechanical structures, and is particularly suitable for the mechanical properties' characterisation of NEMS devices and complex nanomechanical photonic metamaterials. This hyperspectral movement visualization technique is based on conventional scanning electron microscopy which therefore can be widely accessible for researchers from the nanomechanics and nano-optomechanics

community. It can also be applied to a wide variety of nanomaterials, structures, and devices, for highly-localized evaluation of material parameters such as Young's modulus, stress/strain measurement, mass sensing, micro/nano-device manufacturing process control and optimization, non-destructive testing, and the study of forces and fields at the (sub)nanometer scale.

2. In Chapter 5, I have reported an important advance on optical super-resolution imaging, which in a proof-of-principle experiment can localize the position of a nanowire with subatomic resolution beyond the magnitude of its thermal fluctuations via artificial intelligence (AI)-enabled analysis of structured light scattering. This surpasses the routinely achievable optical resolution of a few tens on nanometres, or better than $\lambda/10$ from nonlinear STED (stimulated emission depletion) and statistically enhanced STORM (stochastic optical reconstruction microscopy) techniques used in biological imaging. Illumination with topological light gives access to higher accuracy than conventional plane wave illumination is also demonstrated. The reported proof-of principle demonstration can be straightforwardly applied to measuring subatomic displacements in many practical applications (allowing in-situ training) including: non-contact position monitoring of platforms in ultra-precise STM/AFM instruments and mask aligner; and monitoring structural deformations and thermal drifts in precise instruments.

From a fundamental perspective:

1. In Chapter 4, I have studied fast dynamics of ballistic thermal movement in a nano-membrane to the atomic scale. This enables observation of fundamental statistical mechanics, such as the Maxwell–Boltzmann velocity distribution and the energy equipartition theorem in nanomechanical systems, thus unveiling the fast dynamics underpinning functionality of micro/nano mechanical devices and metamaterials. Short-interval measurements in the ballistic regime (where fast, e.g., micro-channel plate, electron detectors would extend capability to higher frequencies – shorter time intervals) present new opportunities, such as for fast thermometry, based on evaluation of the initial $k_B T/m_{eff}$ slope of mean squared displacement. Importantly, in being based only on the fundamental rules of thermodynamics and knowledge of the material and geometrical parameters of the cantilever, the calibration of such a thermometry would not require reference to any external standard. The slope measurement may also be used for fast monitoring of cantilever mass at known temperature, for instance during materials deposition processes or for the detection of molecular adsorption and desorption [172].
2. In Chapter 6, based on the nano-optomechanical metamaterial platform, I have studied the dynamics of nonlinear nano-optomechanical oscillators that are thermally driven and optically controlled. I have studied the optical parametric control over a thermomechanical oscillator

which allows continuous mechanical frequency conversion utilizing nonlinear optomechanical interaction of frequency mixing. A tunable phononic frequency comb generation mechanism is also provided. Lastly, thermal energy exchange between two optomechanically linked oscillators has also been demonstrated via parametric pumping at the difference frequency of two thermomechanical vibrations. From the fundamental research interest, current work provides a feasible way for realization and implementation of Floquet nano-optomechanical insulator [173], temporal or spatiotemporal metamaterials [174] on nano-optomechanical metamaterial platform. This work may also shed light on diverse applications related to precise probing of the temperature and dynamic thermal response characterization for a nanomechanical structure.

7.2 Outlook

There is enormous scope for further studies. Here a very brief outlook is given on what could follow in this thesis.

From technological perspective:

1. Currently, the 3 dB detection bandwidth of the developed hyperspectral motion visualization technique is ~ 5MHz which is limited by the bandwidth of the built-in secondary electron detector in the SEM. Micro-channel plate electron detectors would extend capability to higher frequencies. With a high-speed secondary electron detector, it would be possible to study dynamics in the GHz frequency range [54, 175]. Promising new techniques for resolving and hyperspectrally mapping picometric movements might also be realized via other modes of imaging (see section 3.1) such as backscattering electrons and cathodoluminescence in the future. Using cathodoluminescence imaging mode, one can not only obtain the movement information but also the optical properties of the nanostructures and their mutual-interactions. This would allow investigating the mechanical phonon-coupled quantum emitters [176, 177] and entangled phonon-photon pairs [178].
2. With a high-speed camera, the artificial intelligence enabled optical super-resolution imaging technique may be possible to visualize the fast dynamics of a nanoscale object, comparable with the above technique realized by the scanning electron microscopy. Besides, the artificial intelligence enabled optical super-resolution imaging technique has currently been demonstrated for 1D imaging in a proof-of-principle experiment, it can be readily extended to 2D and 3D objects of a priori known shapes. It will hopefully be commercially available when its applicability can be extended into objects of random shape. This requires endeavour in developing new algorithms and physics inspired model in artificial intelligence. Furthermore,

how to combine the numerical simulation dataset from Maxwell-solver with the experimental dataset to obtain a trustworthy model and thus getting rid of the lab-intensive dataset collection process requires further efforts.

From fundamental research interest:

The nano-optomechanical metamaterial system provides an ideal platform for studying interesting dynamics in an array of (non-) linear (coupled) oscillators that are driven by Langevin thermal force and controlled optically at low power intensity. Many fundamental research work can be done based on this platform.

This includes mainly nonlinear optomechanics such as phonon lasing and noise squeezing [179] by driving the oscillator in the parametric resonance regime, non-reciprocal phonon transfer [180], synthetic dimension [147], phonon-phonon scattering, and mechanical solitons [152]. These hopefully can be realized by improving the sample design and optimizing the sample fabrication process.

Besides, the nano-optomechanical metamaterial system provides a platform for the study of Van Der Waals, (non-)Hamiltonian forces [23-25], and quantum gravity in nano-systems [181, 182].

Additionally, a collective behavior of an oscillators array (mimicking many-body system), such as the optomechanical synchronization as a result of optomechanical coupling within its constituting elements is expected to be observed when the mechanical frequency variance is smaller than the nonlinear coupling rate. This would allow the realization of a classical analogue of time crystal [183].

These considerations would help to bring nano-optomechanical systems to the fore as candidates for future sensing, communications, computing and networking.

Appendix A Introduction convolutional neural networks and their implementation in this work

Machine learning is a branch of artificial intelligence (AI) and computer science which focuses on the use of data and algorithms to imitate the way that humans learn, gradually improving its accuracy [184]. Machine learning models fall into three primary categories: supervised machine learning, unsupervised machine learning, and reinforcement learning [184, 185]. Deep learning is a subfield of machine learning that is inspired by artificial neural networks, which in turn are inspired by biological neural networks. A specific kind of deep neural network is the convolutional network [185], which is commonly referred to as a CNN or ConvNet. It is a deep, feed-forward artificial neural network, also called a multi-layer perceptron (MLP). Convolutional neural networks have been one of the most influential innovations in the field of machine vision. They have performed far better than traditional machine vision system and have produced state-of-the-art results. These neural networks have proven to be successful in many different real-life case studies and applications, including:

- Image classification, object detection, segmentation, face recognition;
- Self-driving cars that leverage CNN based vision systems;
- Classification of crystal structure using a convolutional neural network.

This success can be traced back initially to 2012, the year in which Alex Krizhevsky [186] used convolutional neural networks to win that year's ImageNet Competition, reducing classification error from 26% to 15%. This brought neural networks to renewed prominence in what is often called the "third wave of neural networks" - the first two waves having been in the 1940s-60s and in the 1970s-80s.

Figure A.1 shows the typical architecture of a convolutional neural network for a supervised learning model. It shows that an image as an input to the network, which goes through multiple convolutions, subsampling, and a fully connected layer, to generate an output. The convolution layer computes the output of neurons that are connected to local regions or receptive fields in the input, each computing a dot product between their weights and a small receptive field to which they are connected in the input volume. Each computation leads to extraction of a feature map from the input image. The objective of subsampling is to obtain an input representation by reducing its dimensions, which helps in reducing overfitting. One of the techniques of subsampling is max pooling. With this technique, one can select the highest pixel value from a region depending on its

size. The objective of the fully connected layer is to flatten the high-level features that are learned by convolutional layers and to combine all of the features. It passes the flattened output to the output layer where one may then use a softmax classifier (for classification tasks) or a sigmoid activation function (for regression tasks) to predict the input image label.

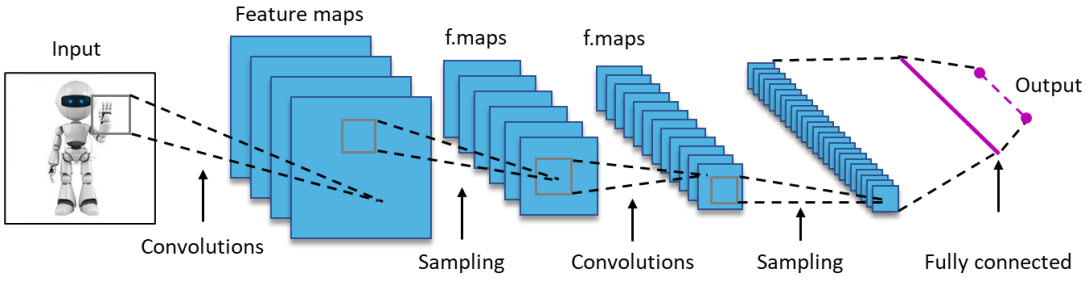

Figure **A. 1 Typical convolutional neural network (CNN) architecture**. A CNN generally contains multiple convolutions, subsampling, a fully connected layer, and a final output layer.

In practice, CNN can be implemented using either TensorFlow or PyTorch frameworks in Python. In Chapter 6, the CNN implementation was realized in TensorFlow using the Keras library. Keras contains numerous implementations of commonly used neural-network building blocks such as layers, objectives, activation functions, optimizers, and a host of tools to make working with image and text data easier, and to simplify the coding necessary for writing deep neural network code. In addition to standard neural networks, Keras contains support for convolutional and recurrent neural networks. It also supports other common utility layers like dropout, batch normalization, and pooling. For linear regression tasks demonstrated, the implementation of a convolutional neural network generally, and specifically in the case demonstrated in Chapter 6, consists of the following procedures:

Load the data: Training and test images, along with their labels, are loaded and stored in variables, which constitute the training and test dataset.

Data preprocessing: Converting each image of the training and test set into a matrix which is fed into the network is the first step. Before feeding it into the network one needs to convert it to float type, and rescale pixel values to the 0 - 1 inclusive range. The labels then need to be converted to a normalized vector in range 0 - 1 (or class labels converted to an encoding vector for classification tasks). The last step is a crucial one: In machine learning or any data specific task, one should partition the data into training and test data correctly (an 80:20% split in the present case). For the model to generalize well, one should also split the training data into two parts, one designed for training and another one for validation. In the present case, we train the network on 80% of the training data and validate it on the remaining 20%. This helps to reduce overfitting by validating the model on data it has not seen in training phase, which helps to boost test performance.

The network: In the present case, images are of a size 350 x 350 pixels. We convert the image matrix to an array, rescale it between 0 and 1, reshape it to a size 350 x 350 x 1, and feed this as an input to the network. Three convolutional layers are used: The first layer has 64 5 x 5 filters; The second layer has 128 4 x 4 filters and the third layer has 256 2 x 2 filters. In addition, there are three max-pooling layers each of size 4 x 4, 4 x 4 and 3 x 3. Finally, three fully connected dense layers containing neurons each of size 128, 256 and 128 that are activated by a sigmoid function.

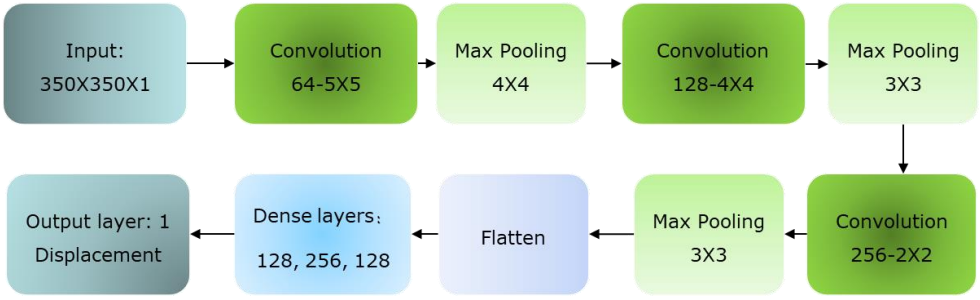

Figure **A. 2 Architecture of the Model**. CNN generally contains multiple convolutions, subsampling, a fully connected layer and a final output layer.

Model the data: Firstly, one must import all the necessary modules required to train the network. We used a batch size of 32. Using a higher batch may be preferable but is constrained by available memory. The choice contributes significantly to determining the learning parameters and affects prediction accuracy.

Neural network architecture: In Keras, one can simply stack the desired layers one by one. We add a first convolutional layer with the Conv2D() function, the max-pooling layer with the MaxPooling2D() function, and so on. The last layer is a Dense layer that has a sigmoid activation function.

Compile the model: After the model is created, it is compiled using the Adam optimizer, one of the most popular optimization algorithms. Finally, one specifies the metric (mean square error in the present case) to be used as a loss function for minimization while the network is training.

Train the model: In Keras, with the Keras' fit() function. One of the problems with training neural networks lies in the choice of the number of training epochs to use. Too many epochs can lead to overfitting of the training dataset, whereas too few may result in an underfit model. Early stopping is a method that allows one to specify an arbitrarily large number of training epochs and then to stop training once the performance stops improving on a holdout validation dataset. This method yields a so-called best trained model.

Predict labels: Finally, using the best trained model, the labels of unseen test images can be predicted by the network.

Appendix B Publications

Journal Articles:

1. **Ballistic Dynamics of Flexural Thermal Movements in a Nano-membrane Revealed with Subatomic Resolution**
   T. Liu, J. Y. Ou, N. Papasimakis, K. F. MacDonald, V. E. Gusev and N. I. Zheludev
   Sci. Adv. **8** (33), eabn8007 (2022) doi: 10.1126/sciadv.abn8007

2. **Visualization of Sub-atomic Movements in Nanostructures**
   T. Liu, J. Y. Ou, E. Plum, K. F. MacDonald, and N. I. Zheludev
   Nano Lett. **21**(18), 7746-7752 (2021) doi: 10.1021/acs.nanolett.1c02644

3. **Detection of sub-atomic movement in nanostructures**
   T. Liu, J. Y. Ou, K. F. MacDonald, and N. I. Zheludev
   Nanoscale Adv. **3**, 2213 (2021) doi: 10.1039/d0na01068e

4. **Thermal fluctuations of the optical properties of nanomechanical photonic metamaterials**
   J. Li, D. Papas, T. Liu, J. Y. Ou, K. F. MacDonald, E. Plum, and N. I. Zheludev
   Adv. Opt. Mater., 202101591 (2021) doi: 10.1002/adom.202101591

5. **Gigahertz Nano-Optomechanical Resonances in a Dielectric SiC-Membrane Metasurface Array**
   I. A. Ajia, J. Y. Ou, N. J. Dinsdale, H. J. Singh, T. Chen-Sverre, T. Liu, N. I. Zheludev, and O. L. Muskens
   Nano Lett. **11**, 4563-4569 (2021) doi: 10.1021/acs.nanolett.1c00205

Manuscript Under Review/ in Preparation:

1. **Picophotonics - Subatomic Optical Localization Beyond Thermal Fluctuations,**
   T. Liu, C. H. Chi, J. Y. Ou, J. Xu, E. A. Chan, K. F. MacDonald, and N. I. Zheludev
   (*Nat. Mater.*, under review) arXiv:2205.01475 (2022)

2. **Photonic metamaterial analogue of a continuous time crystal,**
   T. Liu, J. Y. Ou, K. F. MacDonald, and N. I. Zheludev
   (Nat. Phys., under review) arXiv:2209.00324 (2022)

3. **Parametric control of thermal fluctuation in a nano-optomechanical metamaterial,**
   T. Liu*, J. Li*, J. Y. Ou, K. F. MacDonald, and N. I. Zheludev (In preparation, * joint first authors)

Conference Contributions:

In cases where I am the presenting author, my name is underlined

1. (invited) **Metamaterial analogue of continuous time-crystal,**
   T. Liu, J. Y. Ou, K. F. MacDonald, N. I. Zheludev,
   16th International Congress on Artificial Materials for Novel Wave Phenomena (Metamaterials 2022), Siena, Italy, 12–17 Sept, 2022

2. (invited) **From phase change nanophotonics to phase change nano-opto-mechanics,**
   T. Liu, D. Papas, J. Li, J. Y. Ou, E. Plum, K. F. MacDonald, and N. I. Zheludev
   META 2022, Torremolinos, Spain, 19-22 Jul 2022

3. **Picophotonics: Sub-Brownian detection of nanowire position with atomic-scale resolution using topologically structured light,**
   T. Liu, J.-Y. Ou, J. Xu, K. F. MacDonald, and N. I. Zheludev
   CLEO 2022, San Jose, CA, USA, 15-20 May 2022

4. **Experimental observations of thermal fluctuations of metamaterial optical properties**
   D. Papas, J. Li, T. Liu, J. Y. Ou, K. F. MacDonald, E. Plum, and N. I. Zheludev
   CLEO 2022, San Jose, CA, USA, 15-20 May 2022

5. (keynote) **Picophotonics: visible invisible**
   G. Adamo, E. A. Chan, J. Li, T. Liu, S. Kurdiumov, K. F. MacDonald, J. Y. Ou, N. Papasimakis, E. Plum, T. Pu, C. Rendon-Barraza, Y. Wang, and N. I. Zheludev
   SPIE Photonics Europe 2022, Strasbourg, France, 3-8 Apr 2022
6. **Thermal fluctuations in the optical properties of dielectric and plasmonic nanomechanical metamaterials**
   J. Y. Ou, D. Papas, T. Liu, J. Li, E. Plum, K. F. MacDonald, and N. I. Zheludev
   Nanometa 2022, Seefeld, Austria, 28-31 Mar 2022
7. **Optical metrology with sub-atomic resolution**
   K. F. MacDonald, T. Liu, J. Y. Ou and N. I. Zheludev
   Nanometa 2022, Seefeld, Austria, 28-31 Mar 2022
8. (invited) **Picophotonics**
   C. Rendón-Barraza, E. A. Chan, J. Li, T. Liu, K. F. MacDonald, J.-Y. Ou, D. Papas, N. Papasimakis, E. Plum, T. Pu, G. Yuan, and N. I. Zheludev
   15th International Congress on Artificial Materials for Novel Wave Phenomena, Virtual Meeting, 20-26 Sept 2021
9. (invited) **Picophotonics: Visible invisible**

C. Rendón-Barraza, E. A. Chan, S. Kurdiumov, T. Liu, K. F. MacDonald, J. Y. Ou, N. Papasimakis, T. Pu, G. Yuan and N. I. Zheludev

SPIE Optics & Photonics 2021, Virtual Conference, 1 - 5 Aug 2021

10. (invited) **Metamaterial Nanomachines driven by heat, sound, electric and magnetic fields, and light**

    T. Liu, J. Li, D. Papas, J. Y. Ou, E. Plum, K. F. MacDonald, and N. I. Zheludev

    SPIE Optics & Photonics 2021, Virtual Conference, 1 - 5 Aug 2021

11. (invited) **Dynamics of nanomechanical metamaterials: Pico-vibrometry with light and electron beams**

    J. Y. Ou, T. Liu, J. Li, D. Papas, E. Plum, K. F. MacDonald, and N. I. Zheludev

    META 2021, Virtual Conference, 20 - 23 July 2021

12. (invited) **Nanomechanical photonic metamaterials**

    E. Plum, D. Papas, J. Li, T. Liu, J. Y. Ou, Q. Zhang, G. Lan, K. F. MacDonald, and N. I. Zheludev

    Materials for Humanity (MH21), Virtual Conference, 6-9 July 2021

13. **Flat photonic devices based on nanomechanical metamaterials driven by light, sound, electric and magnetic signals**

    J. Li, T. Liu; K. F. MacDonald, J. Y. Ou, D. Papas, E. Plum, and N. I. Zheludev

    Optical Design and Fabrication Congress, Virtual Conference, 27 Jun - 1 Jul 2021

14. **First Observation of Phonon-induced Ballistic Motion in Photonic Nanostructures**

    T. Liu, J. Y. Ou, K. F. MacDonald, and N. I. Zheludev

    CLEO/Europe-EQEC 2021 Virtual Meeting, 21 - 25 June 2021

15. **Picometric Ballistic (non-Brownian) Thermal Movements in Photonic Nanostructures**

    T. Liu, J. Y. Ou, K. F. MacDonald, and N. I. Zheludev

    CLEO 2021 Virtual Conference, 9-14 May 2021

16. **Ultrafast Hyperspectral Nanomotion Imaging of Ballistic and Brownian Motion in Metamaterial Nanostructures**

    T. Liu, J. Y. Ou, K. F. MacDonald and N. I. Zheludev

    Metamaterials 2020 (Virtual Conference), 28 Sept – 01 Oct 2020

17. (invited) **Functional nanomechanical metamaterials**

    J. Y. Ou, D. Papas, J. Li, T. Liu, Q. Zhang, D. Piccunotti, E. Plum, K. F. MacDonald and N. I. Zheludev

    Photon 2020 (virtual conference), 1-4 Sep 2020

18. **Exotic effects in nanomechanical metamaterials**

    J. Y. Ou, D. Papas, J. Li, T. Liu, Q. Zhang, D. Piccinotti, E. Plum and K. F. MacDonald, and N. I. Zheludev

    SPIE Optics & Photonics 2020, Digital Forum, 23 - 27 Aug 2020

19. (invited) **Functional nanomechanical metamaterials driven by light, electromagnetic forces and sound**

    N. I. Zheludev, D. Papas, T. Liu, J. Li, Q. Zhang, J. Y. Ou, E. Plum, and K. F. MacDonald

    CLEO 2020 Virtual Conference, 11-15 May 2020

20. **High-frequency nano-motion imaging of artificial nanostructures**

    T. Liu, J. Y. Ou, K. F. MacDonald, and N. I. Zheludev

    SPIE Photonics Europe Digital Forum 2020, 6-10 Apr 2020

21. **High-Frequency Nano-motion Electron Imaging for Artificial Nanostructures**

    T. Liu, J. Y. Ou, K. F. MacDonald, and N. I. Zheludev

    Electron Beam Spectroscopy for Nanophotonics 2019 (EBSN2019), Paris, France, 16-19 Sept 2019

22. **Imaging of high-frequency motion in artificial nanostructures**

    T. Liu, J. Y. Ou, K. F. MacDonald, and N. I. Zheludev

    Metamaterials'2019, Rome, Italy, 16 - 21 Sep 2019

Bibliography

1. A. H. Zewail, "Femtochemistry: Atomic-scale dynamics of the chemical bond," *The Journal of Physical Chemistry A*, **104**(24), 5660-5694, 2000.

2. F. Krausz, and M. Ivanov, "Attosecond physics," *Reviews of modern physics*, **81**(1), 163-234, 2009.

3. Y. Luo, X. Yang, T. Feng, J. Wang, and X. Ruan, "Vibrational hierarchy leads to dual-phonon transport in low thermal conductivity crystals," *Nature communications*, **11**(1), 1-10, 2020.

4. X. Gu, and R. Yang, "Phonon transport and thermal conductivity in two-dimensional materials," *Annual review of heat transfer*, **19**, 1-65, 2016.

5. H. Ishikawa, K. Kwak, J. K. Chung, S. Kim, and M. D. Fayer, "Direct observation of fast protein conformational switching," *Proceedings of the National Academy of Sciences*, **105**(25), 8619-8624, 2008.

6. N. I. Zheludev, and E. Plum, "Reconfigurable nanomechanical photonic metamaterials," *Nature nanotechnology*, **11**(1), 16-22, 2016.

7. B. Bhushan, *Springer handbook of nanotechnology* (Springer, 2017).

8. Y. Han, J. Zhou, H. Wang, L. Gao, S. Feng, K. Cao, Z. Xu, and Y. Lu, "Experimental nanomechanics of 2d materials for strain engineering," *Applied Nanoscience*, **11**(4), 1075-1091, 2021.

9. S. Barzanjeh, A. Xuereb, S. Gröblacher, M. Paternostro, C. A. Regal, and E. M. Weig, "Optomechanics for quantum technologies," *Nature Physics*, 1-10, 2021.

10. D. V. Knudson, and D. Knudson, *Fundamentals of biomechanics* (Springer, 2007).

11. A. Bernheim‐Groswasser, N. S. Gov, S. A. Safran, and S. Tzlil, "Living matter: Mesoscopic active materials," *Advanced Materials*, **30**(41), 1707028, 2018.

12. L. Woods, D. A. R. Dalvit, A. Tkatchenko, P. Rodriguez-Lopez, A. W. Rodriguez, and R. Podgornik, "Materials perspective on casimir and van der waals interactions," *Reviews of Modern Physics*, **88**(4), 045003, 2016.

13. T. Kouh, M. Hanay, and K. Ekinci, "Nanomechanical motion transducers for miniaturized mechanical systems," *Micromachines*, **8**(4), 108, 2017.

14. A. H. Zewail, "Four-dimensional electron microscopy," *Science*, **328**(5975), 187-193, 2010.

15. A. Feist, K. E. Echternkamp, J. Schauss, S. V. Yalunin, S. Schäfer, and C. Ropers, "Quantum coherent optical phase modulation in an ultrafast transmission electron microscope," *Nature*, **521**(7551), 200-203, 2015.

16. K. E. Priebe, C. Rathje, S. V. Yalunin, T. Hohage, A. Feist, S. Schäfer, and C. Ropers, "Attosecond electron pulse trains and quantum state reconstruction in ultrafast transmission electron microscopy," *Nature Photonics*, **11**(12), 793-797, 2017.

17. R. Dahan, A. Gorlach, U. Haeusler, A. Karnieli, O. Eyal, P. Yousefi, M. Segev, A. Arie, G. Eisenstein, and P. Hommelhoff, "Imprinting the quantum statistics of photons on free electrons," *Science*, **373**(6561), eabj7128, 2021.

18. S. Lee, D. Broido, K. Esfarjani, and G. Chen, "Hydrodynamic phonon transport in suspended graphene," *Nature communications*, **6**(1), 1-10, 2015.

19. L. Shi, "Nonresistive heat transport by collective phonon flow," *Science*, **364**(6438), 332-333, 2019.

20. J. Lee, K. T. Crampton, N. Tallarida, and V. A. Apkarian, "Visualizing vibrational normal modes of a single molecule with atomically confined light," *Nature*, **568**(7750), 78-82, 2019.

21. D. Peller, L. Z. Kastner, T. Buchner, C. Roelcke, F. Albrecht, N. Moll, R. Huber, and J. Repp, "Sub-cycle atomic-scale forces coherently control a single-molecule switch," *Nature*, **585**(7823), 58-62, 2020.

22. N. I. Zheludev, and K. F. MacDonald, "Picophotonics," in *Plasmonics: Design, Materials, Fabrication, Characterization, and Applications XX*(SPIE2022), p. PC1219701.

23. M. V. Berry, and P. Shukla, "Hamiltonian curl forces," *Proc. R. Soc. A*, **471**, 20150002, 2015.

24. F. Capasso, J. N. Munday, D. Iannuzzi, and H. B. Chan, "Casimir forces and quantum electrodynamical torques: Physics and nanomechanics," *IEEE Journal of Selected Topics in Quantum Electronics*, **13**(2), 400-414, 2007.

25. A. W. Rodriguez, F. Capasso, and S. G. Johnson, "The casimir effect in microstructured geometries," *Nature photonics*, **5**(4), 211, 2011.

26. W. Zhu, R. Esteban, A. G. Borisov, J. J. Baumberg, P. Nordlander, H. J. Lezec, J. Aizpurua, and K. B. Crozier, "Quantum mechanical effects in plasmonic structures with subnanometre gaps," *Nat. Commun.*, **7**(1), 11495, 2016.

27. S. W. Englander, and L. Mayne, "The nature of protein folding pathways," *Proc. Natl. Acad. Sci.*, **111**(45), 15873-15880, 2014.

28. R. P. Feynman, "Plenty of room at the bottom," in *APS annual meeting*(1959).

29. N. I. Zheludev, and Y. S. Kivshar, "From metamaterials to metadevices," *Nature materials*, **11**(11), 917-924, 2012.

30. M. Aspelmeyer, T. J. Kippenberg, and F. Marquardt, "Cavity optomechanics," *Reviews of Modern Physics*, **86**(4), 1391-1452, 2014.

31. W. Cai, and V. M. Shalaev, *Optical metamaterials* (Springer, 2010).

32. A. H. Dorrah, N. A. Rubin, M. Tamagnone, A. Zaidi, and F. Capasso, "Structuring total angular momentum of light along the propagation direction with polarization-controlled meta-optics," *Nature communications*, **12**(1), 1-13, 2021.

33. J.-Y. Ou, E. Plum, L. Jiang, and N. I. Zheludev, "Reconfigurable photonic metamaterials," *Nano letters*, **11**(5), 2142-2144, 2011.

34. A. Karvounis, J.-Y. Ou, W. Wu, K. F. MacDonald, and N. I. Zheludev, "Nano-optomechanical nonlinear dielectric metamaterials," *Applied Physics Letters*, **107**(19), 191110, 2015.

35. J.-Y. Ou, E. Plum, J. Zhang, and N. I. Zheludev, "Giant nonlinearity of an optically reconfigurable plasmonic metamaterial," *Advanced Materials*, **28**(4), 729-733, 2016.

36. Q. Zhang, E. Plum, J. Y. Ou, H. Pi, J. Li, K. F. MacDonald, and N. I. Zheludev, "Electrogyration in metamaterials: Chirality and polarization rotatory power that depend on applied electric field," *Advanced Optical Materials*, **9**(4), 2001826, 2021.

37. G. Lan, J.-Y. Ou, D. Papas, N. I. Zheludev, and E. Plum, "Non-contact optical magnetic field sensor based on metamaterial nanomechanics," *APL Photonics*, **7**(3), 036101, 2022.

38. S. Kapfinger, T. Reichert, S. Lichtmannecker, K. Müller, J. J. Finley, A. Wixforth, M. Kaniber, and H. J. Krenner, "Dynamic acousto-optic control of a strongly coupled photonic molecule," *Nature communications*, **6**(1), 1-6, 2015.

39. Y. Nagasaki, B. Gholipour, J.-Y. Ou, M. Tsuruta, E. Plum, K. F. MacDonald, J. Takahara, and N. I. Zheludev, "Optical bistability in shape-memory nanowire metamaterial array," *Applied Physics Letters*, **113**(2), 021105, 2018.

40. C. Meng, P. C. Thrane, F. Ding, and S. I. Bozhevolnyi, "Full-range birefringence control with piezoelectric mems-based metasurfaces," *Nature communications*, **13**(1), 1-7, 2022.

41. A. Karvounis, N. Aspiotis, I. Zeimpekis, J. Y. Ou, C. C. Huang, D. Hewak, and N. I. Zheludev, "Mechanochromic reconfigurable metasurfaces," *Advanced Science*, **6**(21), 1900974, 2019.

42. J. Zhang, K. F. MacDonald, and N. I. Zheludev, "Nonlinear dielectric optomechanical metamaterials," *Light: Science & Applications*, **2**(8), e96-e96, 2013.

43. P. Cencillo-Abad, J.-Y. Ou, E. Plum, J. Valente, and N. I. Zheludev, "Random access actuation of nanowire grid metamaterial," *Nanotechnology*, **27**(48), 485206, 2016.

44. Z. Han, C. Frydendahl, N. Mazurski, and U. Levy, "Mems cantilever–controlled plasmonic colors for sustainable optical displays," *Science advances*, **8**(16), eabn0889, 2022.

45. J.-Y. Ou, E. Plum, J. Zhang, and N. I. Zheludev, "An electromechanically reconfigurable plasmonic metamaterial operating in the near-infrared," *Nature nanotechnology*, **8**(4), 252-255, 2013.

46. J. Valente, J.-Y. Ou, E. Plum, I. J. Youngs, and N. I. Zheludev, "A magneto-electro-optical effect in a plasmonic nanowire material," *Nature communications*, **6**(1), 1-7, 2015.

47. A. W. Barnard, M. Zhang, G. S. Wiederhecker, M. Lipson, and P. L. McEuen, "Real-time vibrations of a carbon nanotube," *Nature*, **566**(7742), 89-93, 2019.

48. P. N. Pusey, "Brownian motion goes ballistic," *Science*, **332**(6031), 802-803, 2011.

49. S. J. Rothberg, M. S. Allenb, P. Castellinic, D. Di Maiod, J. J. J. Dirckxe, D. J. Ewinsf, B. J. Halkona, P. Muyshondte, N. Paonec, T. Ryang, H. Stegerh, E. P. Tomasinic, S. Vanlanduiti, and J. F. Vignolaj, "An international review of laser doppler vibrometry: Making light work of vibration measurement," *Opt. Laser Eng.*, **99**, 11-22, 2017.

50. A. Barg, Y. Tsaturyan, E. Belhage, W. H. P. Nielsen, C. B. Møller, and A. Schliesser, "Measuring and imaging nanomechanical motion with laser light," *Applied Physics B*, **123**(1), 2016.

51. O. Sahin, S. Magonov, C. Su, C. F. Quate, and O. Solgaard, "An atomic force microscope tip designed to measure time-varying nanomechanical forces," *Nature nanotechnology*, **2**(8), 507, 2007.

52. D. Rugar, R. Budakian, H. Mamin, and B. Chui, "Single spin detection by magnetic resonance force microscopy," *Nature*, **430**(6997), 329-332, 2004.

53. T. Bagci, A. Simonsen, S. Schmid, L. G. Villanueva, E. Zeuthen, J. Appel, J. M. Taylor, A. Sørensen, K. Usami, and A. Schliesser, "Optical detection of radio waves through a nanomechanical transducer," *Nature*, **507**(7490), 81-85, 2014.

54. D. J. Flannigan, P. C. Samartzis, A. Yurtsever, and A. H. Zewail, "Nanomechanical motions of cantilevers: Direct imaging in real space and time with 4d electron microscopy," *Nano letters*, **9**(2), 875-881, 2009.

55. Y. Tsaturyan, A. Barg, E. S. Polzik, and A. Schliesser, "Ultracoherent nanomechanical resonators via soft clamping and dissipation dilution," *Nature nanotechnology*, **12**(8), 776-783, 2017.

56. P. Ahn, X. Chen, Z. Zhang, M. Ford, D. Rosenmann, I. W. Jung, C. Sun, and O. Balogun, "Dynamic near-field optical interaction between oscillating nanomechanical structures," *Sci Rep*, **5**, 10058, 2015.

57. K. Bian, C. Gerber, A. J. Heinrich, D. J. Müller, S. Scheuring, and Y. Jiang, "Scanning probe microscopy," *Nature Reviews Methods Primers*, **1**(1), 1-29, 2021.

58. A. N. Cleland, *Foundations of nanomechanics: From solid-state theory to device applications* (Springer Science & Business Media, 2013).

59. S. Schmid, L. G. Villanueva, and M. L. Roukes, *Fundamentals of nanomechanical resonators* (Springer, 2016).

60. A. Einstein, "On the movement of small particles suspended in stationary liquids required by the molecularkinetic theory of heat," *Ann. d. Phys*, **17**(549-560), 1, 1905.

61. W. Sutherland, "Lxxv. A dynamical theory of diffusion for non-electrolytes and the molecular mass of albumin," *The London, Edinburgh, and Dublin Philosophical Magazine and Journal of Science*, **9**(54), 781-785, 1905.

62. M. Von Smoluchowski, "Zur kinetischen theorie der brownschen molekularbewegung und der suspensionen," *Annalen der physik*, **326**(14), 756-780, 1906.

63. X. Bian, C. Kim, and G. E. Karniadakis, "111 years of brownian motion," *Soft Matter*, **12**(30), 6331-6346, 2016.

64. J. Perrin, "Mouvement brownien et molécules," *J. Phys. Theor. Appl.*, **9**(1), 5-39, 1910.

65. A. Einstein, "Zur theorie der brownschen bewegung," *Annalen der physik*, **324**(2), 371-381, 1906.

66. D. S. Lemons, and A. Gythiel, "Paul langevin's 1908 paper "on the theory of brownian motion"["sur la théorie du mouvement brownien," cr acad. Sci.(paris) 146, 530–533 (1908)]," *American Journal of Physics*, **65**(11), 1079-1081, 1997.

67. R. Kubo, M. Toda, and N. Hashitsume, *Statistical physics ii: Nonequilibrium statistical mechanics* (Springer Science & Business Media, 2012).

68. B. Alder, and T. Wainwright, "Decay of the velocity autocorrelation function," *Physical review A*, **1**(1), 18, 1970.

69. A. B. Basset, *A treatise on hydrodynamics: With numerous examples* (Deighton, Bell and Company, 1888).

70. G. Batchelor, "Fluid mechanics. By ld landau and em lifshitz. 2nd english edition. Pergamon press, 1987. 539 pp.£ 45 or 29.50 (paperback)," *Journal of Fluid Mechanics*, **205**, 593-594, 1989.

71. D. Bedeaux, and P. Mazur, "Brownian motion and fluctuating hydrodynamics," *Physica*, **76**(2), 247-258, 1974.

72. R. Huang, I. Chavez, K. M. Taute, B. Lukić, S. Jeney, M. G. Raizen, and E.-L. Florin, "Direct observation of the full transition from ballistic to diffusive brownian motion in a liquid," *Nature Physics*, **7**(7), 576-580, 2011.

73. T. Franosch, M. Grimm, M. Belushkin, F. M. Mor, G. Foffi, L. Forró, and S. Jeney, "Resonances arising from hydrodynamic memory in brownian motion," *Nature*, **478**(7367), 85-88, 2011.

74. S. Kheifets, A. Simha, K. Melin, T. Li, and M. G. Raizen, "Observation of brownian motion in liquids at short times: Instantaneous velocity and memory loss," *Science*, **343**(6178), 1493-1496, 2014.

75. A. Widom, "Velocity fluctuations of a hard-core brownian particle," *Physical Review A*, **3**(4), 1394, 1971.

76. H. Clercx, and P. Schram, "Brownian particles in shear flow and harmonic potentials: A study of long-time tails," *Physical Review A*, **46**(4), 1942, 1992.

77. R. Zwanzig, and M. Bixon, "Compressibility effects in the hydrodynamic theory of brownian motion," *Journal of Fluid Mechanics*, **69**(1), 21-25, 1975.

78. G. Paul, and P. Pusey, "Observation of a long-time tail in brownian motion," *Journal of Physics A: Mathematical and General*, **14**(12), 3301, 1981.

79. D. A. Weitz, D. J. Pine, P. N. Pusey, and R. Tough, "Nondiffusive brownian motion studied by diffusing-wave spectroscopy," *Physical review letters*, **63**(16), 1747, 1989.

80. H. B. Callen, and T. A. Welton, "Irreversibility and generalized noise," *Physical Review*, **83**(1), 34, 1951.

81. R. Lifshitz, "Phonon-mediated dissipation in micro-and nano-mechanical systems," *Physica B: Condensed Matter*, **316**, 397-399, 2002.

82. C. Zener, "Internal friction in solids ii. General theory of thermoelastic internal friction," *Physical review*, **53**(1), 90, 1938.

83. M. C. Wang, and G. E. Uhlenbeck, "On the theory of the brownian motion ii," *Reviews of modern physics*, **17**(2-3), 323, 1945.

84. S. F. Nørrelykke, and H. Flyvbjerg, "Harmonic oscillator in heat bath: Exact simulation of time-lapse-recorded data and exact analytical benchmark statistics," *Physical Review E*, **83**(4), 041103, 2011.

85. B. D. Hauer, C. Doolin, K. S. D. Beach, and J. P. Davis, "A general procedure for thermomechanical calibration of nano/micro-mechanical resonators," *Annals of Physics*, **339**, 181-207, 2013.

86. J. Y. Stein, *A computer science perspective* (Wiley, 2000).

87. J. E. Kim, "On the equivalent mass-spring parameters and assumed mode of a cantilevered beam with a tip mass," *J. Mech. Sci. Technol.*, **31**(3), 1073-1078, 2017.

88. H. Ftouni, C. Blanc, D. Tainoff, A. D. Fefferman, M. Defoort, K. J. Lulla, J. Richard, E. Collin, and O. Bourgeois, "Thermal conductivity of silicon nitride membranes is not sensitive to stress," *Physical Review B*, **92**(12), 125439, 2015.

89. E. Chávez-Ángel, J. S. Reparaz, J. Gomis-Bresco, M. R. Wagner, J. Cuffe, B. Graczykowski, A. Shchepetov, H. Jiang, M. Prunnila, and J. Ahopelto, "Reduction of the thermal conductivity in free-

standing silicon nano-membranes investigated by non-invasive raman thermometry," *APL Materials*, **2**(1), 012113, 2014.

90. R. Lifshitz, and M. L. Roukes, "Thermoelastic damping in micro-and nanomechanical systems," *Physical review B*, **61**(8), 5600, 2000.

91. C. Zener, "Internal friction in solids. I. Theory of internal friction in reeds," *Physical review*, **52**(3), 230, 1937.

92. K. Babaei Gavan, "Dynamic characterization of silicon nitride cantilevers," 2009.

93. U. Gysin, S. Rast, P. Ruff, E. Meyer, D. Lee, P. Vettiger, and C. Gerber, "Temperature dependence of the force sensitivity of silicon cantilevers," *Physical review B*, **69**(4), 045403, 2004.

94. R. B. Bhiladvala, and Z. J. Wang, "Effect of fluids on the q factor and resonance frequency of oscillating micrometer and nanometer scale beams," *Physical review E*, **69**(3), 036307, 2004.

95. H. Hosaka, K. Itao, and S. Kuroda, "Damping characteristics of beam-shaped micro-oscillators," *Sensors and Actuators A: Physical*, **49**(1-2), 87-95, 1995.

96. S. Kohler, T. Dittrich, and P. Hänggi, "Floquet-markovian description of the parametrically driven, dissipative harmonic quantum oscillator," *Physical Review E*, **55**(1), 300, 1997.

97. E. Betzig, G. H. Patterson, R. Sougrat, O. W. Lindwasser, S. Olenych, J. S. Bonifacino, M. W. Davidson, J. Lippincott-Schwartz, and H. F. Hess, "Imaging intracellular fluorescent proteins at nanometer resolution," *Science*, **313**(5793), 1642-1645, 2006.

98. S. W. Hell, and J. Wichmann, "Breaking the diffraction resolution limit by stimulated emission: Stimulated-emission-depletion fluorescence microscopy," *Optics letters*, **19**(11), 780-782, 1994.

99. S. T. Hess, T. P. Girirajan, and M. D. Mason, "Ultra-high resolution imaging by fluorescence photoactivation localization microscopy," *Biophysical journal*, **91**(11), 4258-4272, 2006.

100. M. J. Rust, M. Bates, and X. Zhuang, "Sub-diffraction-limit imaging by stochastic optical reconstruction microscopy (storm)," *Nature methods*, **3**(10), 793-796, 2006.

101. T. Pu, J. Y. Ou, V. Savinov, G. Yuan, N. Papasimakis, and N. I. Zheludev, "Unlabeled far‐field deeply subwavelength topological microscopy (dstm)," *Adv. Sci.*, **8**, 2002886, 2020.

102. E. T. F. Rogers, J. Lindberg, T. Roy, S. Savo, J. E. Chad, M. R. Dennis, and N. I. Zheludev, "A super-oscillatory lens optical microscope for subwavelength imaging," *Nat. Mater.*, **11**, 432-435, 2012.

103. G. H. Yuan, and N. I. Zheludev, "Detecting nanometric displacements with optical ruler metrology," *Science*, **364**(6442), 771-775, 2019.

104. J. I. Goldstein, D. E. Newbury, J. R. Michael, N. W. M. Ritchie, J. H. J. Scott, and D. C. Joy, *Scanning electron microscopy and x-ray microanalysis* (Springer, 2018).

105. E. Buks, and M. L. Roukes, "Stiction, adhesion energy, and the casimir effect in micromechanical systems," *Physical Review B*, **63**(3), 2001.

106. A. Nigues, A. Siria, and P. Verlot, "Dynamical backaction cooling with free electrons," *Nat Commun*, **6**, 8104, 2015.

107. Q. P. Unterreithmeier, T. Faust, and J. P. Kotthaus, "Damping of nanomechanical resonators," *Physical review letters*, **105**(2), 027205, 2010.

108. J. Rieger, A. Isacsson, M. J. Seitner, J. P. Kotthaus, and E. M. Weig, "Energy losses of nanomechanical resonators induced by atomic force microscopy-controlled mechanical impedance mismatching," *Nature communications*, **5**(1), 1-6, 2014.

109. R. Hooke, *Micrographia: Or some physiological descriptions of minute bodies made by magnifying glasses, with observations and inquiries thereupon* (Courier Corporation, 2003).

110. I. Müllerová, and I. Konvalina, "Collection of secondary electrons in scanning electron microscopes," *J. Microsc.*, **236**(3), 203-210, 2009.

111. D. Drouin, A. R. Couture, D. Joly, X. Tastet, V. Aimez, and R. Gauvin, "Casino v2.42—a fast and easy-to-use modeling tool for scanning electron microscopy and microanalysis users," *Scanning*, **29**(3), 92-101, 2007.

112. S. Morozov, K. Novoselov, M. Katsnelson, F. Schedin, D. Elias, J. A. Jaszczak, and A. Geim, "Giant intrinsic carrier mobilities in graphene and its bilayer," *Physical review letters*, **100**(1), 016602, 2008.

113. E. Mariani, and F. Von Oppen, "Flexural phonons in free-standing graphene," *Physical review letters*, **100**(7), 076801, 2008.

114. A. Taheri, S. Pisana, and C. V. Singh, "Importance of quadratic dispersion in acoustic flexural phonons for thermal transport of two-dimensional materials," *Physical Review B*, **103**(23), 235426, 2021.

115. L. Lindsay, D. Broido, and N. Mingo, "Flexural phonons and thermal transport in multilayer graphene and graphite," *Physical Review B*, **83**(23), 235428, 2011.

116. S. Zheng, J.-K. So, F. Liu, Z. Liu, N. Zheludev, and H. J. Fan, "Giant enhancement of cathodoluminescence of monolayer transitional metal dichalcogenides semiconductors," *Nano Lett.*, **17**(10), 6475-6480, 2017.

117. J. Li, D. Papas, T. Liu, J. Y. Ou, K. F. MacDonald, E. Plum, and N. I. Zheludev, "Thermal fluctuations of the optical properties of nanomechanical photonic metamaterials," *Advanced Optical Materials*, **10**(5), 2101591, 2022.

118. T. Li, S. Kheifets, D. Medellin, and M. G. Raizen, "Measurement of the instantaneous velocity of a brownian particle," *Science*, **328**(5986), 1673-1675, 2010.

119. K. C. Schwab, and M. L. Roukes, "Putting mechanics into quantum mechanics," *Physics Today*, **58**(7), 36-42, 2005.

120. R. Leijssen, and E. Verhagen, "Strong optomechanical interactions in a sliced photonic crystal nanobeam," *Scientific reports*, **5**(1), 1-10, 2015.

121. C. Rendón-Barraza, E. A. Chan, G. Yuan, G. Adamo, T. Pu, and N. I. Zheludev, "Deeply sub-wavelength non contact optical metrology of sub-wavelength objects," *APL Photon.*, **6**, 066107, 2021.

122. E. T. Rogers, S. Quraishe, K. S. Rogers, T. A. Newman, P. J. Smith, and N. I. Zheludev, "Far-field unlabeled super-resolution imaging with superoscillatory illumination," *APL Photonics*, **5**(6), 066107, 2020.

123. K. S. Rogers, K. N. Bourdakos, G. H. Yuan, S. Mahajan, and E. T. Rogers, "Optimising superoscillatory spots for far-field super-resolution imaging," *Optics Express*, **26**(7), 8095-8112, 2018.

124. E. T. Rogers, and N. I. Zheludev, "Optical super-oscillations: Sub-wavelength light focusing and super-resolution imaging," *Journal of Optics*, **15**(9), 094008, 2013.

125. N. I. Zheludev, and G. Yuan, "Optical superoscillation technologies beyond the diffraction limit," *Nature Reviews Physics*, **4**(1), 16-32, 2022.

126. Y. Aharonov, D. Z. Albert, and L. Vaidman, "How the result of a measurement of a component of the spin of a spin-1/2 particle can turn out to be 100," *Physical review letters*, **60**(14), 1351, 1988.

127. M. V. Berry, "Evanescent and real waves in quantum billiards and gaussian beams," *Journal of Physics A: Mathematical and General*, **27**(11), L391, 1994.

128. M. Berry, and S. Popescu, "Evolution of quantum superoscillations and optical superresolution without evanescent waves," *Journal of Physics A: Mathematical and General*, **39**(22), 6965, 2006.

129. P. J. S. Ferreira, and A. Kempf, "Superoscillations: Faster than the nyquist rate," *IEEE transactions on signal processing*, **54**(10), 3732-3740, 2006.

130. N. I. Zheludev, "What diffraction limit?," *Nature materials*, **7**(6), 420-422, 2008.

131. M. Berry, "Exact nonparaxial transmission of subwavelength detail using superoscillations," *Journal of Physics A: Mathematical and Theoretical*, **46**(20), 205203, 2013.

132. F. M. Huang, and N. I. Zheludev, "Super-resolution without evanescent waves," *Nano letters*, **9**(3), 1249-1254, 2009.

133. D. Slepian, and H. O. Pollak, "Prolate spheroidal wave functions, fourier analysis and uncertainty—i," *Bell System Technical Journal*, **40**(1), 43-63, 1961.

134. J. D. Jackson, "Classical electrodynamics," (American Association of Physics Teachers, 1999).

135. J.-Y. Ou, "Reconfigurable photonic metamaterials," in *Physical Sciences and Engineering*(University of Southampton, 2014), p. 126.

136. J. H. Davenport, Y. Siret, and É. Tournier, *Computer algebra systems and algorithms for algebraic computation* (Academic Press Professional, Inc., 1993).

137. G. Yuan, E. T. F. Rogers, and N. I. Zheludev, "“Plasmonics” in free space: Observation of giant wavevectors, vortices, and energy backflow in superoscillatory optical fields," *Light Sci. Appl.*, **8**(1), 2, 2019.

138. L. Shao, M. Yu, S. Maity, N. Sinclair, L. Zheng, C. Chia, A. Shams-Ansari, C. Wang, M. Zhang, and K. Lai, "Microwave-to-optical conversion using lithium niobate thin-film acoustic resonators," *Optica*, **6**(12), 1498-1505, 2019.

139. M. Forsch, R. Stockill, A. Wallucks, I. Marinković, C. Gärtner, R. A. Norte, F. van Otten, A. Fiore, K. Srinivasan, and S. Gröblacher, "Microwave-to-optics conversion using a mechanical oscillator in its quantum ground state," *Nature Physics*, **16**(1), 69-74, 2020.

140. R. Yamazaki, A. Okada, A. Noguchi, S. Akao, Y. Tsukahara, K. Yamanaka, N. Takeda, Y. Tabuchi, K. Usami, and Y. Nakamura, "Radio-frequency-to-optical conversion using acoustic and optical whispering-gallery modes," *Physical Review A*, **101**(5), 053839, 2020.

141. W. Chen, P. Roelli, H. Hu, S. Verlekar, S. P. Amirtharaj, A. I. Barreda, T. J. Kippenberg, M. Kovylina, E. Verhagen, and A. Martínez, "Continuous-wave frequency upconversion with a molecular optomechanical nanocavity," *Science*, **374**(6572), 1264-1267, 2021.

142. A. Xomalis, X. Zheng, R. Chikkaraddy, Z. Koczor-Benda, E. Miele, E. Rosta, G. A. Vandenbosch, A. Martínez, and J. J. Baumberg, "Detecting mid-infrared light by molecular frequency upconversion in dual-wavelength nanoantennas," *Science*, **374**(6572), 1268-1271, 2021.

143. X. Xi, C.-L. Zou, C.-H. Dong, and X. Sun, "Highly tunable broadband coherent wavelength conversion with a fiber-based optomechanical system," *Advanced Photonics*, **4**(5), 056003, 2022.

144. M. Aspelmeyer, T. J. Kippenberg, and F. Marquardt, *Cavity optomechanics: Nano-and micromechanical resonators interacting with light* (Springer, 2014).

145. N. T. Otterstrom, R. O. Behunin, E. A. Kittlaus, and P. T. Rakich, "Optomechanical cooling in a continuous system," *Physical Review X*, **8**(4), 041034, 2018.

146. A. H. Safavi-Naeini, T. Alegre, J. Chan, M. Eichenfield, M. Winger, Q. Lin, J. T. Hill, D. E. Chang, and O. Painter, "Electromagnetically induced transparency and slow light with optomechanics," *Nature*, **472**(7341), 69-73, 2011.

147. J. P. Mathew, J. d. Pino, and E. Verhagen, "Synthetic gauge fields for phonon transport in a nano-optomechanical system," *Nature nanotechnology*, **15**(3), 198-202, 2020.

148. Z. Shen, Y.-L. Zhang, Y. Chen, C.-L. Zou, Y.-F. Xiao, X.-B. Zou, F.-W. Sun, G.-C. Guo, and C.-H. Dong, "Experimental realization of optomechanically induced non-reciprocity," *Nature Photonics*, **10**(10), 657-661, 2016.

149. H. Xu, L. Jiang, A. Clerk, and J. Harris, "Nonreciprocal control and cooling of phonon modes in an optomechanical system," *Nature*, **568**(7750), 65-69, 2019.

150. D. Papas, J.-Y. Ou, E. Plum, and N. I. Zheludev, "Volatile optical bistability enabled by mechanical nonlinearity," *arXiv preprint arXiv:2112.11087*, 2021.

151. M. Bagheri, M. Poot, M. Li, W. P. Pernice, and H. X. Tang, "Dynamic manipulation of nanomechanical resonators in the high-amplitude regime and non-volatile mechanical memory operation," *Nature nanotechnology*, **6**(11), 726-732, 2011.

152. J. Zhang, B. Peng, S. Kim, F. Monifi, X. Jiang, Y. Li, P. Yu, L. Liu, Y.-x. Liu, and A. Alù, "Optomechanical dissipative solitons," *Nature*, **600**(7887), 75-80, 2021.

153. J. Li, "Pico- and nanophotonics of reconfigurable metamaterials," (University of Southampton, 2021), p. 126.

154. S. Sukhov, and A. Dogariu, "Non-conservative optical forces," *Reports on Progress in Physics*, **80**(11), 112001, 2017.

155. M. F. Limonov, M. V. Rybin, A. N. Poddubny, and Y. S. Kivshar, "Fano resonances in photonics," *Nature Photonics*, **11**(9), 543-554, 2017.

156. C. W. Hsu, B. Zhen, A. D. Stone, J. D. Joannopoulos, and M. Soljačić, "Bound states in the continuum," *Nature Reviews Materials*, **1**(9), 1-13, 2016.

157. H. A. Tilmans, M. Elwenspoek, and J. H. Fluitman, "Micro resonant force gauges," *Sensors and Actuators A: Physical*, **30**(1-2), 35-53, 1992.

158. D. Papas, "Nonlinear, sensing and switching functionalities of nano-optomechanical metamaterials," (University of Southampton, 2022), p. 114.

159. V. A. Fedotov, M. Rose, S. L. Prosvirnin, N. Papasimakis, and N. I. Zheludev, "Sharp trapped-mode resonances in planar metamaterials with a broken structural symmetry," *Phys. Rev. Lett.*, **99**, 147401 2007.

160. V. V. Khardikov, E. O. Iarko, and S. L. Prosvirnin, "A giant red shift and enhancement of the light confinement in a planar array of dielectric bars," *J. Opt.*, **14**, 035103, 2012.

161. J. Zhang, K. F. MacDonald, and N. I. Zheludev, "Near-infrared trapped mode magnetic resonance in an all-dielectric metamaterial," *Opt. Express*, **21**(22), 26721-26728, 2013.

162. G. E. Uhlenbeck, and L. S. Ornstein, "On the theory of the brownian motion," *Physical Review*, **36**, 823-841, 1930.

163. G. S. Agarwal, "Brownian motion of a quantum oscillator," *Phys. Rev. A*, **4**, 739, 1971.

164. S. Chandrasekhar, "Stochastic problems in physics and astronomy," *Rev. Mod. Phys.*, **15**(1-89), 1943.

165. G. I. González, and P. R. Saulson, "Brownian motion of a mass suspended by an anelastic wire," *J. Acoust. Soc. Am.*, **96**, 207, 1994.

166. S. Hong, T. P. Weihs, J. C. Bravman, and W. D. Nix, "Measuring stiffnesses and residual stresses of silicon nitride thin films," *J. Electron. Mater.*, **19**, 903, 1990.

167. W. H. Pernice, M. Li, and H. X. Tang, "Photothermal actuation in nanomechanical waveguide devices," *Journal of Applied Physics*, **105**(1), 014508, 2009.

168. M. A. Porter, N. J. Zabusky, B. Hu, and D. K. Campbell, "Fermi, pasta, ulam and the birth of experimental mathematics: A numerical experiment that enrico fermi, john pasta, and stanislaw ulam reported 54 years ago continues to inspire discovery," *American Scientist*, **97**(3), 214-221, 2009.

169. A. Ganesan, C. Do, and A. Seshia, "Phononic frequency comb via intrinsic three-wave mixing," *Physical review letters*, **118**(3), 033903, 2017.

170. L. Cao, D. Qi, R. Peng, M. Wang, and P. Schmelcher, "Phononic frequency combs through nonlinear resonances," *Physical review letters*, **112**(7), 075505, 2014.

171. D. A. Czaplewski, C. Chen, D. Lopez, O. Shoshani, A. M. Eriksson, S. Strachan, and S. W. Shaw, "Bifurcation generated mechanical frequency comb," *Physical review letters*, **121**(24), 244302, 2018.

172. P. M. Kosaka, V. Pini, J. J. Ruz, R. Da Silva, M. González, D. Ramos, M. Calleja, and J. Tamayo, "Detection of cancer biomarkers in serum using a hybrid mechanical and optoplasmonic nanosensor," *Nature nanotechnology*, **9**(12), 1047-1053, 2014.

173. M. S. Rudner, and N. H. Lindner, "Band structure engineering and non-equilibrium dynamics in floquet topological insulators," *Nature reviews physics*, **2**(5), 229-244, 2020.

174. E. Galiffi, R. Tirole, S. Yin, H. Li, S. Vezzoli, P. A. Huidobro, M. G. Silveirinha, R. Sapienza, A. Alù, and J. Pendry, "Photonics of time-varying media," *Advanced Photonics*, **4**(1), 014002, 2022.

175. I. A. Ajia, J.-Y. Ou, N. J. Dinsdale, H. J. Singh, T. Chen-Sverre, T. Liu, N. I. Zheludev, and O. L. Muskens, "Gigahertz nano-optomechanical resonances in a dielectric sic-membrane metasurface array," *Nano Letters*, **21**(11), 4563-4569, 2021.

176. F. Werschler, C. Hinz, F. Froning, P. Gumbsheimer, J. Haase, C. Negele, T. De Roo, S. Mecking, A. Leitenstorfer, and D. V. Seletskiy, "Coupling of excitons and discrete acoustic phonons in vibrationally isolated quantum emitters," *Nano letters*, **16**(9), 5861-5865, 2016.

177. J. Kettler, N. Vaish, L. M. de Lépinay, B. Besga, P.-L. de Assis, O. Bourgeois, A. Auffèves, M. Richard, J. Claudon, and J.-M. Gérard, "Inducing micromechanical motion by optical excitation of a single quantum dot," *Nature nanotechnology*, **16**(3), 283-287, 2021.

178. P. K. Shandilya, D. P. Lake, M. J. Mitchell, D. D. Sukachev, and P. E. Barclay, "Optomechanical interface between telecom photons and spin quantum memory," *Nature Physics*, **17**(12), 1420-1425, 2021.

179. D. Rugar, and P. Grütter, "Mechanical parametric amplification and thermomechanical noise squeezing," *Physical Review Letters*, **67**(6), 699, 1991.

180. D. L. Sounas, J. Soric, and A. Alu, "Broadband passive isolators based on coupled nonlinear resonances," *Nature Electronics*, **1**(2), 113-119, 2018.

181. M. Aspelmeyer, "How to avoid the appearance of a classical world in gravity experiments," *arXiv preprint arXiv:2203.05587*, 2022.

182. M. Bahrami, A. Bassi, S. McMillen, M. Paternostro, and H. Ulbricht, "Is gravity quantum?," *arXiv preprint arXiv:1507.05733*, 2015.

183. N. Y. Yao, C. Nayak, L. Balents, and M. P. Zaletel, "Classical discrete time crystals," *Nature Physics*, **16**(4), 438-447, 2020.

184. M. I. Jordan, and T. M. Mitchell, "Machine learning: Trends, perspectives, and prospects," *Science*, **349**(6245), 255-260, 2015.

185. K. O'Shea, and R. Nash, "An introduction to convolutional neural networks," *arXiv preprint arXiv:1511.08458*, 2015.

186. A. Krizhevsky, I. Sutskever, and G. E. Hinton, "Imagenet classification with deep convolutional neural networks," *Communications of the ACM*, **60**(6), 84-90, 2017.